EXPERIMENTAL INVESTIGATION OF BASE FLOW FIELD AT HIGH ALTITUDE FOR A FOUR-ENGINE CLUSTERED NOZZLE CONFIGURATION

by

Edwin B. Brewer
George C. Marshall Space Flight Center

and

Charles E. Craven
Lockheed Missiles and Space Company

NATIONAL AERONAUTICS AND SPACE ADMINISTRATION • WASHINGTON, D. C. • MAY 1969

EXPERIMENTAL INVESTIGATION OF BASE FLOW FIELD AT

HIGH ALTITUDE FOR A FOUR-ENGINE CLUSTERED

NOZZLE CONFIGURATION

By Edwin B. Brewer

George C. Marshall Space Flight Center
Marshall, Ala.

and

Charles E. Craven

Lockheed Missiles and Space Company
Huntsville, Ala.

NATIONAL AERONAUTICS AND SPACE ADMINISTRATION

TABLE OF CONTENTS

LIST OF ILLUSTRATIONS

LIST OF ILLUSTRATIONS (Continued)

LIST OF ILLUSTRATIONS (Continued)

LIST OF ILLUSTRATIONS (Concluded)

DEFINITION OF SYMBOLS

Symbol	Definition

A   Nozzle throat area

A_w Overheating parameter, $\dfrac{1}{2}\left(\dfrac{i}{R_w}\right)\left(\dfrac{\partial R_w}{\partial i}\right)_h$,

a_w Overheating parameter, $\left(R_w - R_{w_{i=0}}\right)\Big/ R_{w_{i=0}}$

A_e Nozzle exit area

C   Variable defined by equation (3)

c_p Specific heat at constant pressure

d_e Nozzle exit diameter

dz   Incremental length along wire

D   Wire diameter

E $E = \dfrac{1 - \epsilon}{1 + A_w}$

e   Wire voltage

G   Shock wave angle (see Figure 65)

g   Dimensional conversion factor, $32.2 \text{ ft-lb}_m / \text{lb}_f \sec^2$

h   Infinite wire convective heat transfer coefficient

i   Wire current

K $\dfrac{T_w}{R_w}\left(\dfrac{dR_w}{dT_w}\right)$

k   Thermal conductivity

DEFINITION OF SYMBOLS (Continued)

Symbol	Definition
k_a	Thermal Conductivity of air
L	Finite wire length
M	Mach number, $u/(\gamma\mathscr{R}T)^{\frac{1}{2}}$
m	Variable defined by equation (4)
m_t	$\dfrac{T}{\mu}\left(\dfrac{d\mu}{dT}\right)$, evaluated at the local stagnation temperature
Nu	Infinite wire Nusselt number, hD/k_o
n_t	$\dfrac{T}{k_a}\left(\dfrac{dk_a}{dT}\right)$, evaluated at the local stagnation temperature
P	Static pressure
P_b	Base pressure
P_{b_c}	Center base pressure
P_c	Cell pressure
P_I	Impact tube pressure
P_o	Plenum pressure
R	Electrical resistance
Rn	Reynolds number, $\rho u D/\mu_o$
$R_{\sigma\tau}$	Correlation coefficient between modes
$\mathscr{R}$	Gas constant, ft lb_f/lb_m °R
S	Entropy

DEFINITION OF SYMBOLS (Continued)

Symbol	Definition
T	Temperature; also impingement locus non-dimensionalized
T_s	Support temperature
T_{aw}	Infinite wire temperature for no heat transfer
u	Local flow velocity
X, Y, Z	Cartesian coordinate system defined by Figure 11
x, y	Morkovin's fluctuation diagram coordinates defined by equation (14)
z	Distance along wire
α	$\left[1 + \dfrac{\gamma - 1}{2} M^2\right]^{-1}$
α_T	Temperature-resistance coefficient, $R_w/R_r = 1 + \alpha(T_w - T_r)$
β	$(\gamma - 1)M^2\alpha$; also impingement line sweep angle (see Figure 64)
β'	Supplement of β
γ	Ratio of specific heats; also see Figure 65
δ	Flow deflection angle (see Figure 66)
ϵ	Finite wire impedance factor, $\dfrac{R}{i}\left(\dfrac{\partial i}{\partial R}\right)_{sys}$
η	Recovery factor, T_{aw}/T_o
θ	Shock wave angle (see Figure 66)
θ_n	Conical nozzle half-angle
θ_l	Streamline impingement angle (see Figure 64)

DEFINITION OF SYMBOLS (Concluded)

Symbol	Definition
μ	Absolute viscosity of air
ν	Variable defined as $mL/2$
ξ	$100\dfrac{P - \bar{P}}{\bar{P}}$
ρ	Local flow density
σ	$100\dfrac{S - \bar{S}}{c_p \bar{S}}$
τ	$100\dfrac{u - \bar{u}}{\bar{u}}$
τ_{wr}	$\dfrac{T_w - T_{w_{i=0}}}{T_{w_{i=0}}}$

Subscripts and superscripts

Symbol	Definition
$(\ )_D$	Values obtained from Dewey's correlation
$(\ )_f$	Present approximation in iteration
$(\ )_h$	Heating of wire changing with flow field unchanged
$(\ )_o$	Condition based on stagnation temperature
$(\ )_r$	Reference
$(\ )_{sys}$	Changes with electrical system untouched
$(\ )_w$	Wire
$(\ )_1$	Values upstream of shock wave
$(\ )_2$	Values downstream of shock wave
$\overline{(\ )}$	Time average values
$(\ )'$	RMS values (with the exception of β')

EXPERIMENTAL INVESTIGATION OF BASE FLOW FIELD AT HIGH ALTITUDE FOR A FOUR-ENGINE CLUSTERED NOZZLE CONFIGURATION

SUMMARY

An experimental investigation of the base flow field for a four-engine clustered nozzle configuration was made over the characteristic range of center base pressure to ambient pressure ratio range from near 1.0 to near 4.0. Surveys of the base flow were made with static and pitot pressure probes, a constant current anemometer, condenser microphones, and wind vanes. The reverse flow was confined to the proximity of the model centerline and appeared to be an axisymmetric jet decaying from supersonic to subsonic flow. This reverse jet impinged on the center of the heat shield and spread out, forming a wall jet. A slowly circulating "separated" flow region was present in the base region formed from the viscous pumping of the nozzle jet plumes, the axisymmetric reverse jet, and the base wall jet. The static pressure in the circulating region was very nearly ambient. Hot-wire measurements indicated that the flow of the reverse jet had a relatively low turbulence level. The reverse jet originates from the detached shock portion of the "inviscid plume-plume impingement line" rather than the oblique shock recompression portion; therefore, the shear layer type of analysis for calculating the reverse flow is not applicable.

INTRODUCTION

The base heating of rocket powered vehicles from the jets of their own engines has been a problem of importance for over a decade [1]. The base heating is a result of strong radiation from the use of kerosene as a fuel, afterburning of turbine exhaust products, and interaction of plumes from multi-nozzle configurations. The interaction produces a reverse flow that impinges on the vehicle base and results in convective heat transfer. Techniques introduced by Korst, et al., [2] and used by Goethert [3] as well as by Page and Dixon [4] have been considered to be the major contributions in attempts to analyze base flow, but even these are admitted to be limited to qualitative estimates. The complexity of the multi-nozzle configurations and the reverse flow phenomena has almost eliminated analytical attempts to solve the problem, leaving experimental techniques as the only means of obtaining design information. Most experimental investigations have been limited to obtaining surface

measurements; consequently, the flow field has not been understood. The present experimental study examines the base flow itself, so that perhaps reasonable analytical models of the base flow can be constructed.

The center base pressure variation with ambient pressure (altitude) of four-engine configurations has become known as the characteristic curve. A typical characteristic curve is shown in Figure 1. One would have expected that the base pressure would simply have decreased with increasing altitude until the vent area between the nozzles became choked, and that further decreases in ambient pressure would not have affected the base pressure. Although this simple model has been known to be incorrect for some time, it has remained as a useful concept. The "reversals" that occur in the characteristic curve have not been explained. Parametric investigations have shown how the characteristic curve varies with heat shield position, nozzle area ratio, nozzle spacing, nozzle lip angle, etc. These investigations are reported in the literature and some data obtained by R. Matz and Goethert [5] at Arnold Engineering Development Center are reproduced in Figure 2. The "choked" conditions appear to occur in each case at a nominal base-to-ambient-pressure ratio of four. When no interaction between plumes occurs, the ratio is naturally one. The present investigation covers the range from near one to near four along the characteristic curve. The majority of the data was taken at the three pressure ratios indicated in Figure 1 in relation to the characteristic curve; specifically these pressure ratios are 20×10^{-4}, 26×10^{-4}, and 39×10^{-4}. The investigation was conducted in unheated air, thereby simplifying instrumentation techniques. As one would expect, the major features of the reverse flow are similar for hot or cold jets. This view is supported in Reference 6 by comparison of the characteristic curves obtained from a model test [7] using heated and unheated air and from combustion tests [8, 9] of two other four-engine models. If base burning were to occur, however, the characteristic flow pattern might be destroyed.

The flow field was surveyed in the planes of symmetry, and surface pressure measurements were obtained. No external flow existed over the model, and there were no configuration variables.

APPARATUS

Model

Details of the model are shown in Figure 3. The nozzles, which are conical with an area ratio of 3.11 and have an exit diameter of 2.67 inches, are

equally spaced on a 6. 6-inch diameter circle. Their external shape is cylindrical. The heat shield is located 2. 0 inches from the nozzle exit plane, giving a vent area between nozzles of approximately 2. 0 by 2. 0 inches. This model is a larger scale model of the one used to obtain the characteristic curve labeled "Matz" in Figure 1. With the heat shield in the nominal position the model characteristic curve is given by the one labeled "l_v = 0. 8" in Figure 2 (rather than "l_v = 2. 0, " because of the scale change).

Test Cell and Ejector

A schematic of the test cell, model, and ejector is shown in Figure 4. The dashed line in the ejector represents a second configuration tested by the insertion of a cylindrical sleeve. The model and plenum chamber are movable with respect to the ejector so that maximum ejector efficiency can be obtained. The performance of the first ejector configuration is shown in Figure 5. The exhaust plume did not fill this ejector, making the desired pressure ratio of 10×10^{-4} unattainable and making cell pressure control difficult. The cylindrical sleeve was installed to insure precise cell pressure control; however, the lowest pressure ratio attainable with the cylindrical ejector was 17×10^{-4}.

The test cell ambient pressure was initially measured by a shielded impact tube on the cell wall in the nozzle exit plane. At high nozzle plenum pressures, the relatively large amount of reversed flow impinging on the cell wall in the vicinity of the cell pressure tube produced erratic pressure variations. Although most data were taken at a low plenum pressure where this behavior did not occur, the cell pressure measurement was switched to a nozzle surface location close to the nozzle exit plane and outside the nozzle cluster. This pressure, which differs little from the one on the cell wall, is representative of the pressure seen by the plumes. Pressure variations on the nozzle surface are small, so that the plume sees the same pressure inside the cluster as it does outside, at least in the exit plane, or at the nozzle lip. The nozzle pressure taps are shown in Figure 6, a photograph taken through the access door. The access door mounted on the side of the cell allows entry to the cell for frequent instrument changes.

A three-dimensional traversing mechanism was mounted inside the cell above the model for probe manipulation during a run. Operation was from either a console or a hand-held remote control box. Two traversing speeds were available, designated fast and slow, corresponding to 0. 1 in./sec and 0. 01 in./sec. Position potentiometers provided output to digital voltmeters or

recording system to an accuracy of 0.001 inch. An additional traversing mechanism providing axial and rotational traversing is located behind the model heat shield for probe manipulation through the heat shield center.

Facility

The test was conducted in the intermittent tunnel building at the Von Karman Facility (VKF), of Arnold Engineering Development Center, Tullahoma, Tennessee. This facility was chosen so that a relatively large model could be tested, thereby minimizing traversing probe disturbances to the base flow. Schematics of the VKF facility and cell installation are shown in Figures 7 and 8. Basically, the facility operation is intermittent with dry unheated air supplied from VKF's 4000 psia high pressure bottle and exhausted into a 200 000 cu ft vacuum sphere.

There are two modes of operation: (1) The test cell is evacuated by opening valve A (see Figure 8) and then valve B to bring the model plenum to the desired total pressure. Valve C is closed. Valve E remains open with vacuum pumps operating on the sphere during the run, and the inbleed valve may or may not be open, depending on the desired cell pressure. (2) Valve A is opened to evacuate the cell. Valve E is then closed. Valve B is open to bring the model plenum to the desired pressure. Valve C is opened to allow the vacuum pumps to pump on the cell, and the inbleed valve remains closed. Run time is about five to six minutes in the first mode and about three minutes in the second. Turn-around time depends on the operating plenum pressure; for the range of plenum pressures from 20 psia to 100 psia turn-around times vary from 20 minutes to 50 minutes. This time was used for instrumentation changes.

DISCUSSION

Wind Vane

The small wind vane shown in Figure 9 was very valuable in determining the overall characteristics of the base flow field. The vane was slightly damped with grease so that it was responsive to flow directions only in the relatively high dynamic pressure regions. Probing was restricted to the geometric planes of symmetry where the flow component perpendicular to the planes is zero. For purposes of discussion, the coordinate system is defined as shown in Figure 10,

and will be used in the presentation of data. The origin of the coordinate system is located at the heat shield center. Since the XYZ traversing mechanism is mounted above the model, all traverses were made in the vertical plane of symmetry, i. e. , the YZ plane.

It was discovered that the main portion of the reverse flow was confined to the centerline of the model — termed "the reverse jet" — and in close proximity to the heat shield — termed "the wall jet." Elsewhere, the wind vane was not responsive to flow direction and produced erratic results. The flow direction throughout the reverse jet was very nearly perpendicular to the heat shield, while the flow direction of the wall jet was naturally parallel to the heat shield.

Static Pressure

Since the flow through the vent area is confined primarily to the vicinity of the heat shield, probes entering the base region through the low dynamic pressure region do not significantly alter the base flow field. This was indicated by the fact that static pressures on the heat shield and nozzles were unaffected. When the probes were moved into the reverse jet, however, the heat shield static pressures near the heat shield center did become somewhat erratic because of the probe wake. The heat shield pressure distributions for the three pressure ratios are given in Figure 11.

Details of the pressure probe used to obtain static pressures in the base region are shown in Figure 12. It is essentially a thin flat circular disk, having its edge (circumference) beveled on the lower surface and having a static orifice located at its center. As long as the disk is coincident with the plane of symmetry, i. e. , the YZ plane, the static pressure profiles can be obtained without regard for the flow direction; however, since flow directions were known from the wind vane, the tube support was always bent so that it was aligned with flow, thereby reducing wake disturbances.

Data were taken in the reverse jet along Y-traverses in 0.2-inch increments for various distances from the heat shield. The data are shown in Figures 13, 14, and 15 for the three pressure ratios. In general, the static pressure gradients in the base region are small. Static pressure distributions in the plume impingement regions are more interesting. Continuous traces were made in both the Y direction and the Z direction through the near plume region

and recorded on a Variplotter. The data were taken at the high traversing speed since low speed traverses gave essentially identical results. Since these pressures could be affected by probe disturbances because of the flow direction downstream of the impingement, the data are shown without scale in composite form in Figure 16. A 3- by 3.5-inch section of the Y-Z plane of symmetry (see Figure 16) is bounded on one side by the model centerline (Y = 0) and on another side by the nozzle exit plane (Z = 2). Also shown is the impingement centerline (see Figure 64c) which is in the plane of symmetry and is 2.33 inches from the model centerline. The static pressures exhibit some degree of symmetry about this centerline. It can be seen that the data repeated itself at redundant positions. Superimposed on the figure is the inviscid plume impingement line for comparison with the peak pressure points.

Impact Pressure

Because the impact tubes are not very sensitive to flow direction and the wind vane indicated nearly normal reverse flow, impact pressure measurements were made with the tube axis parallel to the model centerline. The details of the probe are shown in Figure 17. The impact pressure data, taken in the same manner as the static pressure data, are shown in Figures 18, 19, and 20 for the three pressure ratios. The same probe was used in the wall jet with the probe axis parallel to the heat shield (the data are shown in Figures 21, 22, and 23). Some additional data were taken with a hypodermic tube in order to get closer to the heat shield (see Figures 22 and 23).

To obtain a better perspective of the base flow field, the impact data are superimposed upon the physical coordinate system in Figures 24, 25, and 26. The arrowheads indicate the orientation of the impact tubes relative to the model. Also shown in these figures are the inviscid plume impingement lines, which will be discussed more fully in a later section.

The static pressures were combined with the impact data to obtain the Mach number profiles shown in Figures 27, 28, and 29. The profiles, along the model centerline, are shown in Figure 30 for various pressure ratios. These data were taken in 1/2-inch increments. From the figure it can be seen that the Mach number increases as the pressure ratio drops and that the position of the peak Mach number moves toward the heat shield as does the sonic point. Also, there is a marked increase in the static pressure as the reverse jet approaches the heat shield at the lower pressure ratio. Evidently the drop in Mach number as the flow approaches the heat shield is caused in part by viscous dissipation; however, this does not explain the static pressure rise. This static pressure rise is puzzling since it begins while the flow is still supersonic. Perhaps the presence of smeared-out shocks or multiple shocks near the heat shield would explain the data. At the lower pressure ratio, static and impact

6

data were taken continuously on a slow speed traverse along the model center-line and recorded on the plotter. There was no evidence from the plot of any discontinuity existing in the base region at that pressure ratio; however, it is unlikely that the type instrumentation used here would indicate with any clarity the presence of small discontinuities were they to occur. Reference 10 attributed the smooth decay from supersonic flow to subsonic flow without shocks to viscous decay; however, the short running lengths and the increasingly rapid deceleration with decreasing pressure ratio, along with the observed rise in static pressure, tend to indicate the presence of smeared shocks. Better flow field instrumentation, preferably optical instrumentation, is required to determine the true nature of the reverse jet recompression.

Fluctuating Base Pressure

A Brüel and Kjaer microphone was mounted flush in the center of the heat shield to determine if any resonant base cavity pressure fluctuations were present. The output of the microphone, recorded on magnetic tape at 60 inches per second in the FM mode, was reduced to the power spectral density function plots shown in Figures 31 through 34. Data were taken at two plenum pressures, 20 psia and 70 psia, and at a pressure ratio of 40×10^{-4}. A small spike occurs in the power spectrum at about 700 cps. Kistler 701A piezoelectric transducers mounted off the heat shield center as accelerometers made it apparent that the structural vibrations did not affect the microphone output and that a low energy resonance of unknown source is present in the base flow cavity. This resonance may originate individually or in combination with the plume impingement, the plume shear layer, the wind tunnel noise, or possibly from cell cavity resonance.

Hot Wire Anemometer

Hot-wire data were taken in the base flow region (1) to obtain a degree of redundancy in instrumentation and thereby obtain agreement or disagreement with the Mach number obtained from the pressure instrumentation; (2) to attempt to measure adiabatic wire temperatures to be used with pressure data to obtain mean flow measurements, and (3) to establish the base flow turbulence level. The theoretical methods and the experimental techniques for obtaining these data are discussed along with the results in this section.

DETERMINATION OF LOCAL FLOW MACH NUMBER

Method. The hot-wire system provides the heat transfer from the wire to the stream and the wire recovery temperature for zero heat transfer. The flow field can be determined from this information if one additional thermodynamic measurement is made and if the relations for heat loss and recovery factor are known functions of the flow properties. For the transition region between continuum and free molecular flow, theoretical relations are not available. Experimental correlations must be relied upon. Dewey's correlation [11] which is the best that is presently available, was used in the data analysis presented here, where necessary. Dewey's correlation is for an infinite wire so that one must take into account the heat transfer from the wire to the support. This is done by using the finite-wire equation which is derived as follows:

Starting with the differential heat balance equation for a finite wire having internal heat generation, convective heating to the air, and heat loss to supports having equal temperatures, one has

$$h\pi D \, dz(T_w - T_{aw}) - \frac{\pi D^2}{4} \frac{d}{dz}\left(k_w \frac{dT_w}{dz}\right) dz = i^2 \frac{R_w}{L} dz \; . \qquad (1)$$

Replacing R_w by $R_r [1 + \alpha(T_w - T_r)]$ gives the differential equation for the wire temperature distribution. The boundary conditions are:

1. at $z = 0$, $dT_w/dz = 0$

2. at $z = L/2$, $T_w = T_s$

where $z = 0$ corresponds to the center of the wire with the assumption of equal support temperatures.

The solution, assuming constant wire thermal conductivity, is

$$T_w = \frac{T_s - C}{\cosh(mL/2)} \cosh(mz) + C \quad , \qquad (2)$$

where

$$C = \frac{i^2 R_r (1 - \alpha T_r)/L + h\pi D\, T_{aw}}{h\pi D - i^2 R_r\, \alpha/L} \tag{3}$$

and

$$m^2 = \frac{4}{\pi D^2 k_w}\, (h\pi D - i^2 R_r\, \alpha/L) \quad. \tag{4}$$

The mean wire temperature is found by integrating across the wire, so that

$$\overline{T}_w = \frac{2}{L} \int_0^{L/2} T_w\, dz = C + \frac{T_s - C}{\nu}\, \tanh(\nu) \quad, \tag{5}$$

where $\nu = m\, L/2$. The finite wire equation can be used in conjunction with experimental data to obtain the two-dimensional values of Nusselt number, Nu, and adiabatic wire temperature, T_{aw}. We simply measure the wire temperature at any two different wire currents along with the support temperature, which then gives two equations and two unknowns — Nu and T_{aw}. Redundancy can be obtained by making measurements at additional currents, thereby giving a check on the applicability of the finite wire equation to the physical problem. With Nu and T_{aw} known, the other flow properties can be obtained by any suitable iteration scheme. The one used here is as follows:

1. Assume the recovery factor to be 1.0: $\eta_f = 1.0$

2. Assume then that the Mach number is 1.0: $M_f = 1.0$

3. Compute stagnation temperature: $T_o = T_{aw}/\eta_f$

4. Use the static pressure from the experimental data and the mass flow equation to obtain the Reynolds number:

$$\frac{\rho u D}{\mu_o} = \frac{PDM_f}{\mu_o \sqrt{T_o}} \left[1 + \frac{\gamma - 1}{2} M_f^2\right]^{\frac{1}{2}} \left[\frac{\gamma g}{\mathscr{R}}\right]^{\frac{1}{2}} \tag{6}$$

5. Use M and Rn and Dewey's correlation to obtain η_D

6. Increment M_f and iterate above procedure (steps 2 to 6) until $\eta_D = \eta_f$

7. Use converged values and Dewey's correlation to obtain Nu_D

8. ˙Increment η_f and iterate above procedure (steps 1 to 8) until $Nu_D = Nu$

Experiment. A photograph of a typical hot-wire probe used in the base region is shown in Figure 35. Design details are shown schematically in Figure 36. The hot-wire supports were hypodermic needles epoxied into 1/8-inch O.D. stainless steel tubing. The needle separation permitted nominal wire lengths of 30/1000 inch. At each needle tip, a thermocouple junction was formed from iron-constantan lead wire which passed through the hollow needle. All of the hot wires that were used for the test were soldered onto the thermocouple junctions. Care was taken to insure wire voltage/thermocouple voltage isolation. The probe lead resistance was measured by placing the probe tip in a mercury bath and measuring the resistance at the probe connector with a Kelvin bridge. Wire flexure and subsequent failure were reduced by applying rubber cement to the wire/support juncture. All wires used were platinum-10-percent-rhodium of 0.0001 inch diameter.

The voltage across the hot wire, probe, and leads was amplified by a Dana Model 3420 dc amplifier before being recorded on an X-Y Plotter. The current, selected at the current control panel of the Transmetrics Unit, was recorded by hand. The position signal from the survey unit potentiometer was fed to a Cohu digital voltmeter and to the X-Y Plotter. Since the Plotter was spanned to respond with maximum sensitivity for a selected current, current changes would drive the plotter pen off scale so that a dc off-set or a bias voltage was required. This off-set was obtained from a precision voltage source (Dial-A-Volt model DAV-46D, General Resistance, Inc.) which allowed off-sets with an accuracy of 0.001 mv. The anemometer and recording system are shown schematically in Figure 37. During run periods all the equipment was left operating continuously and was calibration checked periodically during a run shift.

The hot-wire probe was mounted above the model to the survey unit in a vertical position with the 1/2-inch probe tip coinciding with the model center-line, and the wire oriented parallel to the X-axis so that for traverses on the

10

vertical plane of symmetry (i. e. , the Y-Z plane at X = 0) , the flow will always be perpendicular to the wire. Y-traverses across the reverse jet were made from the model centerline (Y = 0) upward. Z-traverses across the wall jet were made from the heat shield (Z = 0) outward.

Thermocouples were mounted on the lip of one nozzle, in the test cell, and in the model plenum chamber. The temperatures were recorded on the VKF standard data system, along with the heat shield and nozzle pressure data. The nozzle lip temperature continually decreased during the run approaching recovery temperature. Also, the plenum temperature slowly decreased because of pressure drop in the VKF high pressure bottle. Two cool-down runs were usually necessary to insure a nominal temperature variation during subsequent runs. Nozzle lip and plenum temperature variation during the run affect the reverse jet stagnation temperature and have considerable effect on the hot-wire measurements. Attempts to measure current-resistance were not made until the flow field became thermally steady as indicated by the wire support temperature.

All R-i data were recorded on Y-traverses in the model exit plane (Z = 2). This one traverse was considered sufficient for indicating agreement or disagreement with pressure data, and was repeated on several runs so that confidence in the hot-wire results could be ascertained. The resistance and temperature of the wire were recorded on the run log before and after each run so that changes in wire characteristics could be noted and be used as reference conditions for the data reduction.

An example of the data taken from the plotter is reproduced in Figure 38 from run 907-6. The three currents used were 0. 392 ma, 3. 0 ma, and 4. 0 ma. The fourth trace shown is a repeat of the first current. The probe voltage is obtained by adding the off-set voltage to that read from the trace. It is noted that the first and fourth trace do repeat fairly well. For the first trace at the model centerline, Y = 0, the trace reads 3. 04 mv + 10. 2 mv offset or a total of 13. 24 mv, while the fourth trace gives 1. 215 mv + 12. 0 mv offset for a total of 13. 215 mv, the difference being 0. 025 mv. This corresponds to 0. 064 ohm or about 2 degrees Rankine in wire temperature. As seen from Figure 39, the support temperature also varied about 2 degrees. The probe used on this particular run had a lead resistance of 0. 785 ohm which must be subtracted from that obtained from the plotter to obtain wire resistance.

Figure 40, an example output from the VKF data system, corresponds to the data taken immediately before and after each trace. The variations in

cell pressure, plenum pressure, plenum temperature, as well as nozzle lip temperature during the run, can be directly observed. The nozzle wall temperature variation from trace 1 to trace 4 was also 2 degrees.

Using the data at Y = 0 and the finite wire equation, curves of Nu vs T_{aw} were generated for each wire current. The results are plotted in Figure 41. It is gratifying that the three curves intersect at a single point, indicating that the finite wire equation is an adequate description of the physical problem. Using the higher and lower wire currents and the procedure outlined in the previous section, the Mach number profile was calculated. The result is compared with the Mach number obtained from the pressure data in Figure 42 for run 907-3. The agreement is considered to be excellent; therefore, the Mach number used to reduce the remainder of the hot-wire data will be obtained from the pressure data.

MEAN FLOW MEASUREMENTS

Method. Having established a reasonable confidence level in the Mach number obtained from pitot and static pressure probes we can obtain the flow properties with only one additional thermodynamic measurement. The measured wire adiabatic temperature (low wire current) can be obtained rather easily in comparison to the previous method. Any time hot-wire measurements are made, a sustained effort is required and support by people having a good knowledge of the electronic equipment is needed. Although making adiabatic wire temperature measurements is one of the easiest to make, it is still necessary to use finite wire corrections, the heat transfer correlations are still needed, and an iteration is still necessary. However, only a single iteration is required, as compared to the double iteration in the previous technique. The iteration is on the local stagnation temperature. From an assumed stagnation temperature, the flow properties are obtained and a new stagnation temperature is calculated from the finite-wire equation. Since the finite-wire equation is used with only very low wire currents, equation (5) can be simplified by setting $i = 0$ with the result given by

$$\overline{T}_w = T_{aw} + \frac{T_s - T_{aw}}{\nu} \tanh (\nu) \qquad (7)$$

where

$$\nu = (L/D) (Nu\, k_a/k_w)^{\frac{1}{2}} \quad .$$

12

Dividing through by T_o and replacing T_{aw}/T_o by the recovery factor η and solving for T_o gives

$$T_o = \frac{\nu \overline{T}_w - T_s \tanh(\nu)}{\eta [\nu - \tanh(\nu)]} \quad . \tag{8}$$

This iteration procedure closes rapidly, requiring only two or three iterations.

Experiment. The data were taken in much the same way as outlined in the previous section, except that only one current was used (0.392 ma). Y-traverses were made at four Z stations: 1.0, 1.5, 2.0, 2.5. Z-traverses were made at six Y stations: 1.0, 1.5, 2.0, 2.5, 3.0, 3.5. Data were obtained for the three pressure ratios except for the wall jet where the pressure ratio 20×10^{-4} was not obtained. Examples of raw data plots taken directly from the X-Y plotters are reproduced in Figures 43 through 48. The voltage on these plots must be corrected as before for lead resistance. The short run-time did not allow the flow sufficient time to attain complete thermal equilibrium before data recording started. Since the local velocity is relatively insensitive to changes in local stagnation temperature, attaining complete thermal equilibrium was not a necessity.

Some of the resulting flow properties are presented in Figures 49 through 54. The range over which the plenum stagnation temperature, the nozzle lip temperature, and the test cell ambient temperature varied during the particular run is indicated on the local base flow stagnation temperature curves. It is noted that the stagnation temperature does not fall in the expected range, i.e., between the nozzle plenum value and the nozzle lip value. Careful reassessment of these data and data reduction techniques did not reveal any explanation for the apparent discrepancy.

TURBULENCE MEASUREMENTS

Method. Morkovin [12] has established the theoretical basis and operational procedures to decompose the hot-wire voltage fluctuations into the various thermodynamic and kinematic flow fluctuations. With the set of sensing variables, u, ρ, and T_o, the voltage fluctuations across the wire from mean voltage drop, $\bar{e}$, as a function of time, is

$$\Delta e = -\Delta e_\rho \left(100 \frac{\rho - \bar{\rho}}{\bar{\rho}}\right) - \Delta e_u \left(100 \frac{u - \bar{u}}{\bar{u}}\right) + \Delta e_{T_o} \left(100 \frac{T_o - \bar{T}_o}{\bar{T}_o}\right), \tag{9}$$

13

or the voltage fluctuation with respect to mode fluctuations is

$$\Delta e = \Delta e_{\sigma} \sigma + \Delta e_{\tau} \tau + \Delta e_{\xi} \xi \quad , \tag{10}$$

where σ, τ, and ξ correspond to the entropy, vorticity, and sound modes. The two equations serve to define the sensitivity coefficients, Δe_{ρ}, Δe_{u}, Δe_{ξ}, Δe_{T}, Δe_{σ}, and Δe_{τ}. These coefficients are functions of the electrical system and the thermodynamic and kinematic flow properties. The contribution due to the sound mode will be assumed negligible for purposes of data reduction. In light of the results obtained, this assumption appears to be valid (see Reference 12). The general expression for these coefficients as derived by Morkovin are (with the exception of the sound coefficient)

$$\Delta e_{\sigma} = \Delta e_{\rho} + \alpha \Delta e_{T_o}$$

$$\Delta e_{\tau} = \beta \Delta e_{T_o} - \Delta e_{u} \quad , \tag{11}$$

where α and β are functions of Mach number, and where

$$\Delta e_{\rho} = \frac{\bar{e} E}{100} \left[A_w \frac{Rn}{Nu} \frac{\partial Nu}{\partial Rn} - \frac{A_w}{\tau_{wr}} \frac{Rn}{\eta} \frac{\partial \eta}{\partial Rn} \right]$$

$$\Delta e_{u} = \frac{\bar{e} E}{100} \left[A_w \left\{ \frac{Rn}{Nu} \frac{\partial Nu}{\partial Rn} + \frac{1}{\alpha} \frac{M}{Nu} \frac{\partial Nu}{\partial M} \right\} - \frac{A_w}{\tau_{wr}} \left\{ \frac{1}{\alpha} \frac{M}{\eta} \frac{\partial \eta}{\partial M} + \frac{Rn}{\eta} \frac{\partial \eta}{\partial Rn} \right\} \right]$$

$$\Delta e_{T_o} = \frac{\bar{e} E}{100} \left[K + A_w \left\{ K - 1 - n_t + m_t \frac{Rn}{Nu} \frac{\partial Nu}{\partial Rn} + \frac{1}{2\alpha} \frac{M}{Nu} \frac{\partial Nu}{\partial M} \right\} \right. \tag{12}$$

$$\left. - \frac{A_w}{\tau_{wr}} \left\{ \frac{1}{2\alpha} \frac{M}{\eta} \frac{\partial \eta}{\partial M} + m_t \frac{Rn}{\eta} \frac{\partial \eta}{\partial Rn} \right\} \right] .$$

The parameters that affect the wire response can be seen directly. Normally, these expressions are reduced to simplified form by assuming some of the partial derivatives to be small or negligible; in particular, the term (M/Nu) $(\partial Nu/\partial M)$ is essentially zero at high Reynolds number and Mach number. For the present experiment, no such simplifications occur and the full expressions

14

were used. Using Dewey's empirical heat law [11], the various partial derivatives were calculated (see Figures 55 through 58). Squaring and averaging of equation (10) yields

$$\Delta e'^2 = \Delta e_\sigma^2 \, \sigma'^2 + \Delta e_\tau^2 \, \tau'^2 + 2\Delta e_\sigma \, \Delta e_\tau \, \sigma' \, \tau' \, R_{\sigma\tau} \quad , \tag{13}$$

where the sound mode has been dropped. By dividing through by Δe_σ^2 and using Morkovin's x-y nomenclature,

$$x = \Delta e_\tau / \Delta e_\sigma \tag{14}$$

$$y = \Delta e' / \Delta e_\sigma \quad ,$$

the equation becomes

$$y^2 = \sigma'^2 + 2 \, x \, \sigma' \, \tau' \, R_{\sigma\tau} + x^2 \, \tau'^2 \quad , \tag{15}$$

which is the equation of a hyperbola. By taking data at several overheats and using a least mean square hyperbola curve fit, the three unknowns, σ', τ', and $R_{\sigma\tau}$ can be obtained.

Experiment. All turbulence data were recorded at a single position in the reverse flow — on the model centerline at the nozzle exit plane, i.e., $Y = 0$, $Z = 2$. The cell was evacuated, and the current and time constant were measured at several overheats. After flow was started and the probe moved into position, the current required to obtain a given overheat was measured and the time constant calculated by slide rule (using the fact that the time constant is inversely proportional to the square of the current for a given overheat) and set in. This time constant was checked using a square wave generator on several runs and found to be correct. (The fact that this could be done indicated that the turbulence level was not large.) The wire voltage signal from the Shapiro-Edwards amplifier was fed to a Hewlett-Packard RMS meter and its 20-second averaging time output fed to a United Systems Corporation Digitec dc voltmeter. The digital output was recorded by hand for the several different overheats obtained during a run. The RMS noise was recorded at each overheat. The overheating parameter a_w was varied from 0.0 to 0.4 in approximately 0.04 increments. The amplifier gain and support temperature were recorded. The mean flow parameters were taken from the previously obtained mean flow measurements, and sensitivity coefficients were calculated by using Figures 55 through 58. The various overheat parameters needed to obtain the sensitivity coefficients were obtained in the following manner: The R-i data

were curve-fitted by using the theoretical finite-wire equation, and the resulting equation was differentiated to obtain A_w and τ_{wr} from their respective definitions. The zero overheat wire resistance and current exhibited some scatter from run to run, caused entirely by variation of tunnel stagnation temperature, over which we had no control. The finite circuit impedance factor, ϵ, which appears in E, was calculated from the known circuit (with the bridge in the circuit) as a function of the wire current. The voltage of the hot wire system was increased from 25 to 50 volts to reduce the finite circuit impedance factor. The data are shown in Figures 58 through 62, where the RMS voltage has been corrected for noise and gain. Using the faired curve through the RMS data, the x-y fluctuating diagram was calculated, and the results were plotted in Figure 63. Superimposed is the least mean square hyperbola curve fit having the equation $y^2 = 50.7155x^2 - 50.9441x + 53.3067$, and therefore $\sigma' = 7.30\%$, $\tau' = 7.12\%$, and $R_{\sigma\tau} = -0.49$.

Analysis of Inviscid Plume Impingement

Since the test was conducted with a particular geometry and particular plenum conditions, it is necessary to interpret the results in the light of theoretical analysis to prevent their generalization to situations where they are invalid. The effect of the various geometric and fluid dynamic variables upon the base flow field is determined by their effect upon the plume interaction regions and the shock structure existing in these regions. Mentioned previously in conjunction with Figures 24, 25, and 26 were the inviscid plume impingement lines, which represent the locus of intersection of solid plumes. If the geometry and flow conditions are such that an oblique shock can turn the flow into the plane of symmetry, then the inviscid plume impingement line represents the shock attachment line. This flow situation is represented in Figure 64a, b, and c. A reference line is drawn in the plane of symmetry through the impingement line at the point where streamline M_1 makes an angle with the reference line of θ_1. The impingement line or the shock origin is swept an angle β relative to the reference line, which is the intersection line of the plane of symmetry and the plane containing streamline M_1. The element indicated in Figure 64c is enlarged in Figure 65. The initial streamline M_1 passes through the shock and is turned into the plane of symmetry, becoming streamline M_2. As viewed from A in the figure, the shock plane makes an angle G with the plane of symmetry. Likewise, as viewed from B, the plane containing streamline M_1 makes an angle γ with the plane of symmetry. The plane containing both M_1 and M_2, labeled plane $\overline{102}$ in Figure 66, is perpendicular to the shock plane. M_2 is required to be in this normal plane since that plane contains the resultant

normal component of M_1 and the resultant tangential component of M_1. Therefore, the flow deflection angle δ and the shock wave angle θ as related to M_1 through the Rankine-Hugoniot [13] relations must be measured in this same normal plane. M_1, θ, and β are known for each impingement point as a result of geometry. If G were known, then δ and θ could also be obtained from geometry. G can then be varied through the range from zero to some G_{max}, and δ versus θ can be plotted. The points where this geometric curve of δ versus θ crosses the fluid mechanics solution of δ versus θ represent the solution points. The geometric curves of δ versus θ start on the line $\theta = \delta$ for $G = G_{max}$ and also end on the line $\theta = \delta$ for $G = 0$. G_{max} is the angle the shock makes with the plane of symmetry when M_2 coincides with the impingement line; i.e., the plane, containing M_1 and perpendicular to the shock, passes through the impingement line. The geometric curves for several impingement points are plotted in Figure 67 along with the fluid dynamic solution. At the first impingement point, there are two solutions corresponding to the weak and strong shocks, and, likewise, at impingement point 2, except that the two solutions are at two flow deflection angles. At the third impingement point, there are two weak shock solutions. At point 4 there is only one solution at the point of tangency. Beyond point 4, there are no oblique shock solutions. At point 4, $\delta = \delta_{max}$ for the component of M_1 normal to the impingement line. Figure 68 shows δ, θ, and G plotted as they vary along the impingement line. For a clustered nozzle configuration where the inviscid impingement line is terminated by the model centerline before point 4, one could use a Korst-type calculation to calculate the mass reversed along the impingement line and integrate from point 1 to the model centerline. However, as pointed out by Chu [14] such a configuration would require such a large exit Mach number as to preclude its existence for a four-engine cluster. Normally, the shock is detached along a portion of the impingement line. For the configuration tested here, the shocks could not be attached between the model centerline and the tick marks in Figures 24, 25, and 26. Therefore, that portion of the inviscid impingement line has little meaning. Evidently, the flow is turned by the shock in a lateral direction where it becomes trapped and forms a reverse jet. Outside the cluster, this lateral flow moves away from the base region and does not affect its environment unless there is an external flow over the vehicle. The strength of the reverse jet is dependent upon the percentage of the impingement line having a detached shock. Naturally, the lower the external pressure the greater the percentage; however, the strength of the reverse jet is dependent upon other factors as well, such as the mass flow along the plume boundary which decreases with decreasing external pressure. When the external pressure becomes very small, its influence upon the base flow dwindles, and the plumes are dependent more upon the base pressure environment of their own making.

At pressure ratios lower than those tested here, the shock will be detached along the entire impingement length, in which case the reverse flow from the closest impingement point (point 1) might or might not affect the heat shield environment. In this connection, it is noted that this model was run with a fifth nozzle mounted at the center of the cluster, and although the recompression shocks were detached all along the impingement lines, the heat shield and nozzle static taps indicated ambient pressure. This occurred at a pressure ratio of 26×10^{-4}. Even though the total mass reversed was greater than that from the four-engine configuration at the same pressure ratio, it did not significantly affect the base environment.

There is yet to appear in the literature solutions for the impingement regions, in particular, solutions pertaining to the detached shock and lateral flow. It appears that time-dependent finite difference techniques have the best chance of solving this problem. The laser-doppler [15] technique for obtaining flow information in these impingement regions is technically feasible at present, and perhaps data pertaining to this problem will be generated within the following year.

CONCLUSIONS

The flow field in the base region of a four-engine cluster consists of an almost axisymmetric turbulent jet impinging upon the heat shield center, forming a wall jet. This pattern persists throughout the "reversal" portion of the characteristic curve. The reverse jet originates from the lateral flow emanating from behind the detached shock portion of the plume impingement. The viscous flow emanating from the attached shock portion of the plume impingement region does not significantly affect the base environment and is pumped from the base region by the reverse jet and wall jet.

The reverse jet at first accelerates to supersonic flow and then decelerates as it approaches the heat shield. The deceleration becomes more rapid with increasing altitude as the peak Mach number position and the sonic point move toward the heat shield. The wall jet boundary layer grows and accelerates to sonic velocity in the vicinity of the vent area between nozzles.

Heat transfer and pressure distribution over the heat shield probably could be predicted for four-engine configurations by using techniques applicable to normal jet impingement on flat plates, provided that the strength of the reverse jet were known. In the past, calculations of mass reversed have been based upon the recompression of the plume viscous mixing layer rather than on the actual detached shock-lateral flow pattern that exists. Hopefully, greater emphasis will be placed on the real problem in the future.

George C. Marshall Space Flight Center
National Aeronautics and Space Administration
Marshall Space Flight Center, Alabama, December 12, 1968
933-32-19-00-62

19

REFERENCES

1. Dahm, W. K.: Present Techniques and Problems in the Determination of the Base Heating Environment of Propelled Booster and Space Vehicles. Paper presented at the Fifth International Symposium on Space Technology and Science in Tokyo, Japan, September 2 through 7, 1963.

2. Korst, H. H., Chow, W. L., and Zumwalt, G. W.: Research on Transonic and Supersonic Flow of a Real Fluid at Abrupt Increases in Cross Section. University of Illinois, ME Technical Report 392-5, December 1959.

3. Goethert, B. H.: Base Flow Characteristics of Missiles with Cluster-Rocket Exhausts. IAS Paper No. 60-89, July 1960.

4. Page, R. H., and Dixon, R. J.: Base Heating on a Multiple Propulsion Nozzle Missile. Paper presented at the AIAA Summer Meeting in Los Angeles, California. Paper No. 63-179, June 17 through 20, 1963.

5. Matz, R., and Goethert, B. H.: Fluid Dynamic Aspects of Space Flight, Vol. II, Experimental Investigation of Base Flow Characteristics of Four Nozzle-Cluster Rocket Model. Gordon and Breach, AGARDograph 87, 1966.

6. Wilson, H. B.: A New Technique for Simulating Rocket Engine Flow for Study of Base Heating Problems. Paper presented at the AIAA Aerodynamic Testing Conference, in Los Angeles, California, Paper No. 66-760, September 21 through 23, 1966.

7. Sola, J. M., and Nelius, M. A.: Base-Flow-Field Investigation of a Four-Engine Saturn S-IV (3.6-Percent-Scale) Cold-Flow Model at Simulated Altitudes up to 194,000 Feet. AEDC-TDR-62-76, May 1962, [C].

8. Morris, J. A., and Cannell, A. L.: Base Recirculation of a 1/10-Scale Saturn S-IV Stage at Simulated Altitudes above 142,000 Feet. AEDC-TN-61-102, August 1961, [C].

9. Bird, K. D., Matthis, C. L., and Reece, J. W.: The Application of Short Duration Techniques to the Experimental Study of Base Heating. Part I — High Altitude Testing Technique and Experimental Results for a Four-Engine Rocket Configuration. CAL Report No. HM-1510-Y-1(I), April 1962.

REFERENCES (Concluded)

10. Wasco, R. A., and Cover, T. L.: Experimental Investigation of Base Flow Field at High Altitudes for Configurations of Four and Five Clustered Nozzles. Lewis Research Center, NASA TM X-1371, May 1967.

11. Dewey, C. F.: A Correlation of Convective Heat Transfer and Recovery Temperature Data for Cylinders in Compressible Flow. International Journal of Heat and Mass Transfer. Vol. 8, 1965.

12. Morkovin, M. V.: Fluctuations and Hot-Wire Anemometry in Compressible Flows. Gordon and Breach, AGARDograph 24, 1956.

13. Shapiro, A. H.: The Dynamics and Thermodynamics of Compressible Fluid Flow, Vol. II. The Ronald Press Company, 1954.

14. Chu, C. W.: Conditions for Non-Reversing of Exhaust Gas in a Multijet-Plume. Northrop Norair Monthly Progress Report No. 5, Contract NAS8-11260, December 1964.

15. Rolfe, E., et al.: Final Report — Laser Doppler Velocity Instrument. Raytheon Company Report R67-4450, Contract NAS8-20413, December 1967.
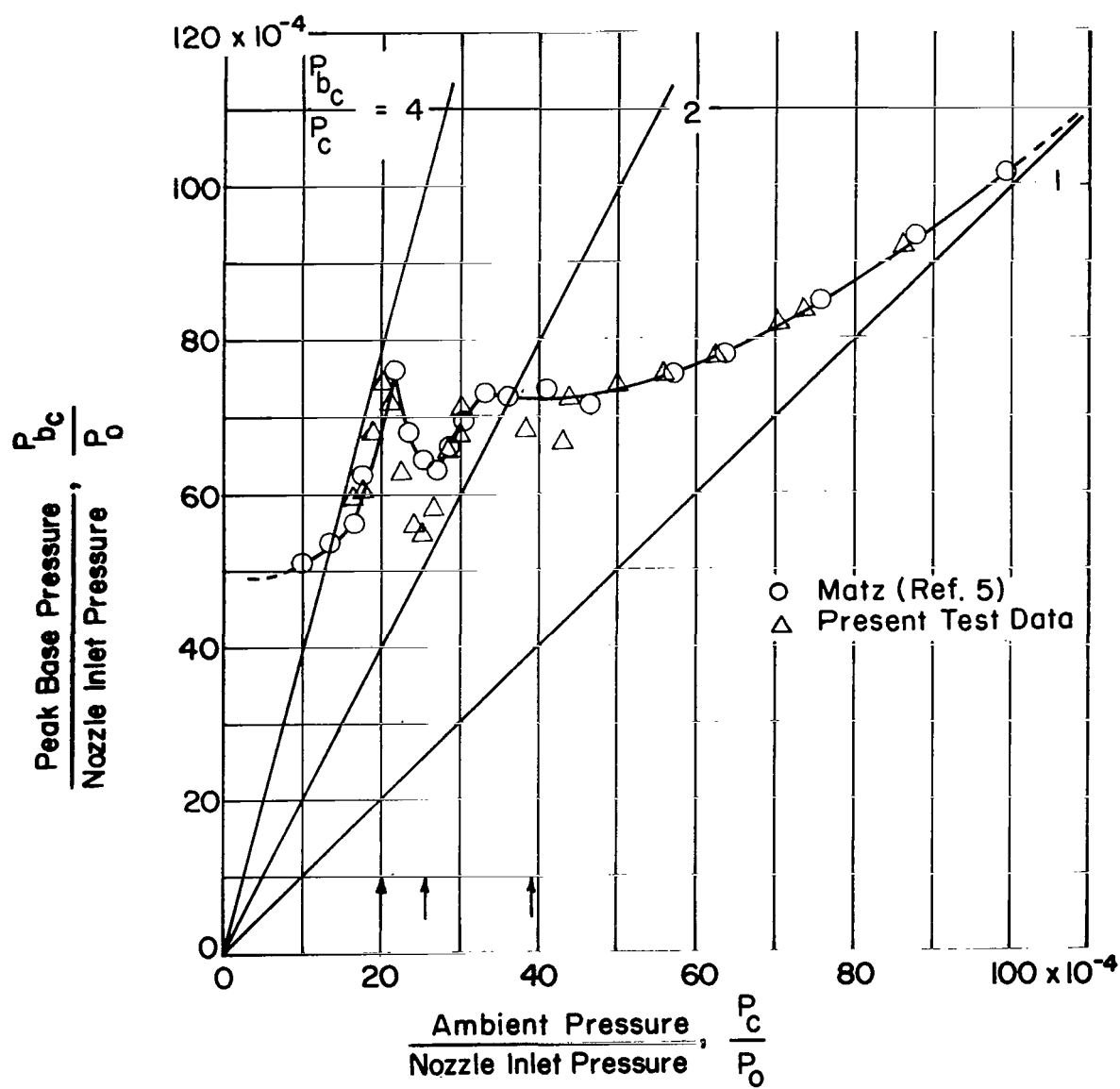
FIGURE 1.   BASE PRESSURE CHARACTERISTIC CURVE
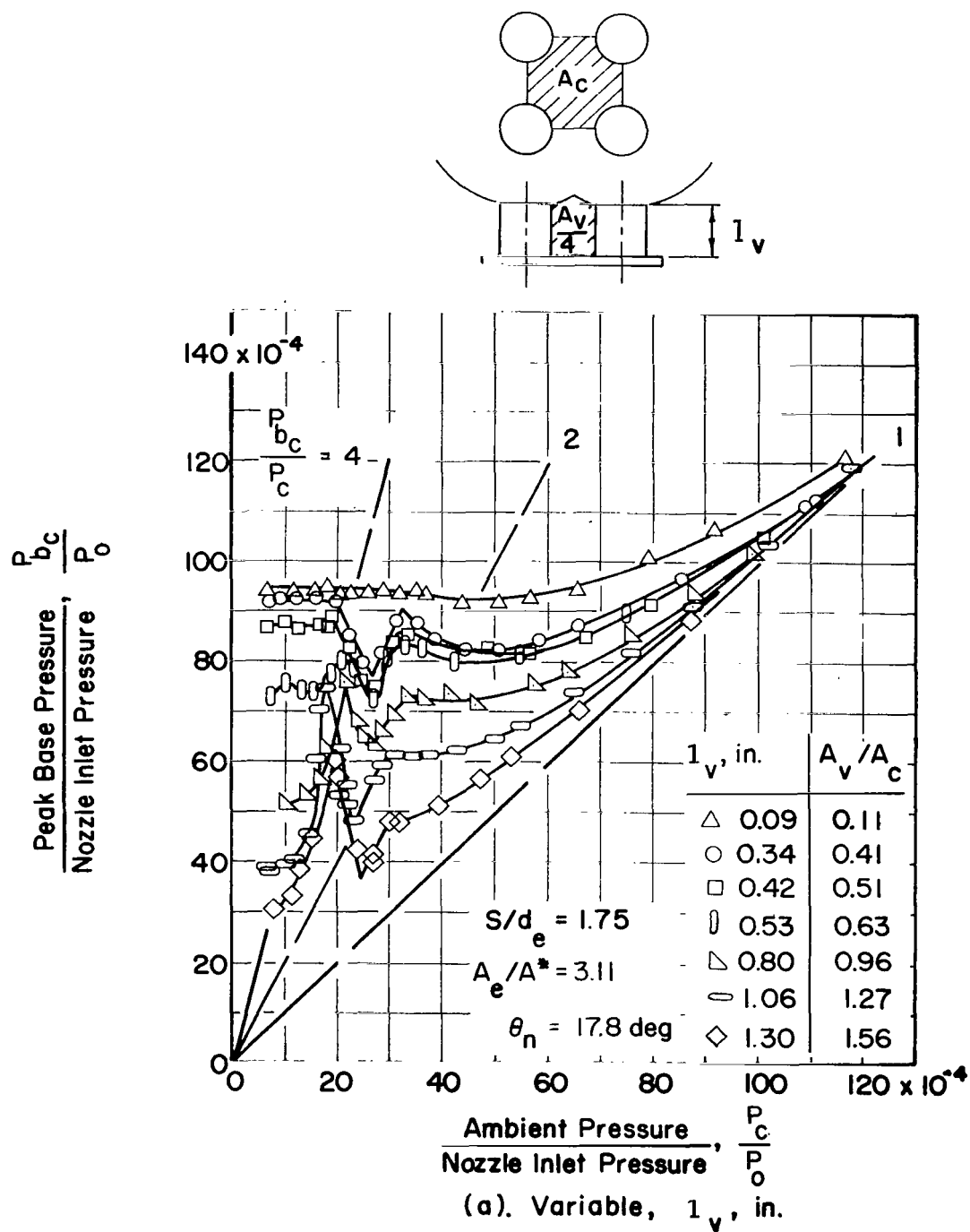
FIGURE 2. EFFECT OF HEAT SHIELD LOCATION ON BASE
PRESSURE CHARACTERISTICS

Section AA

Dimensions in inches
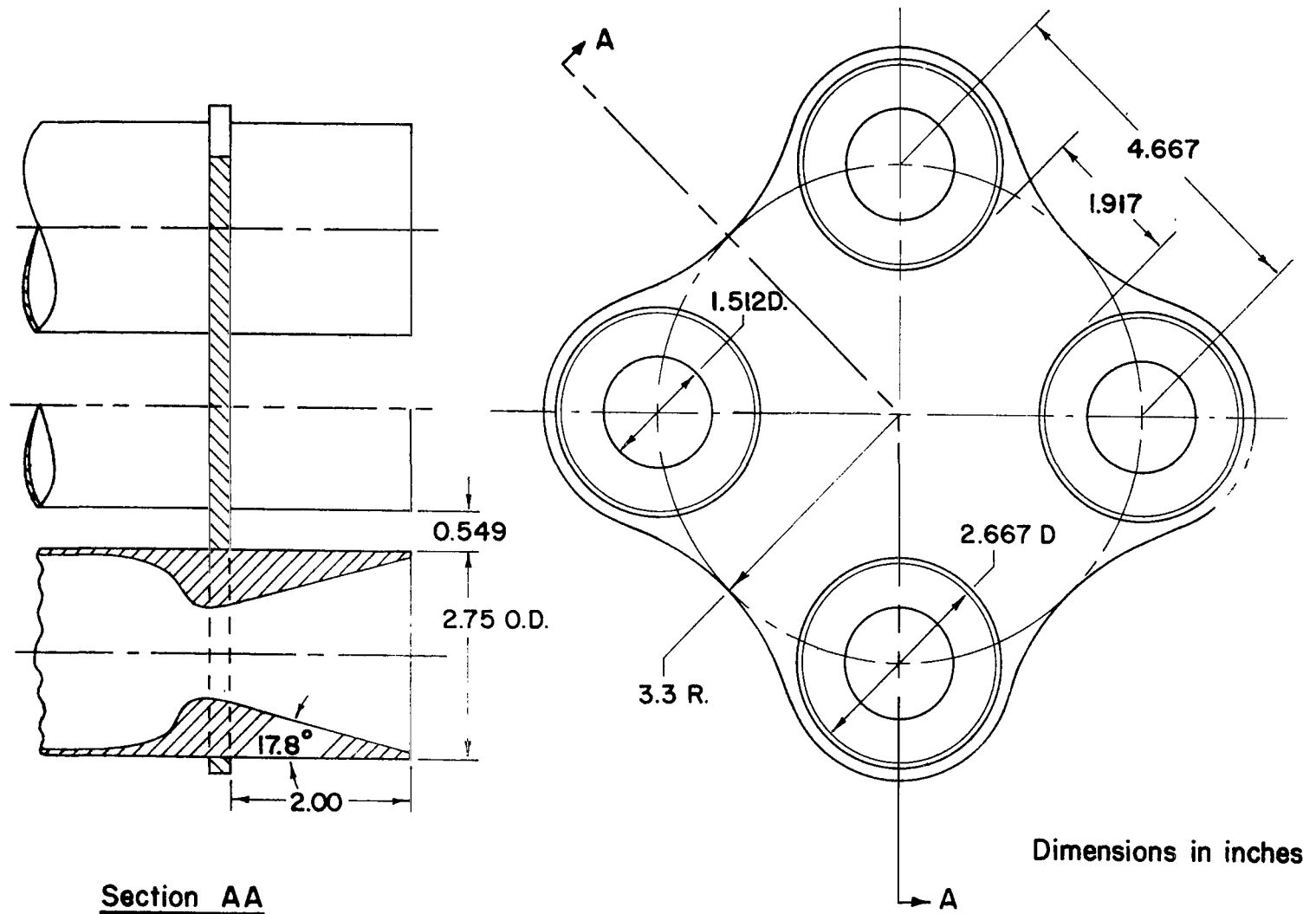
FIGURE 3. MODEL CONFIGURATION
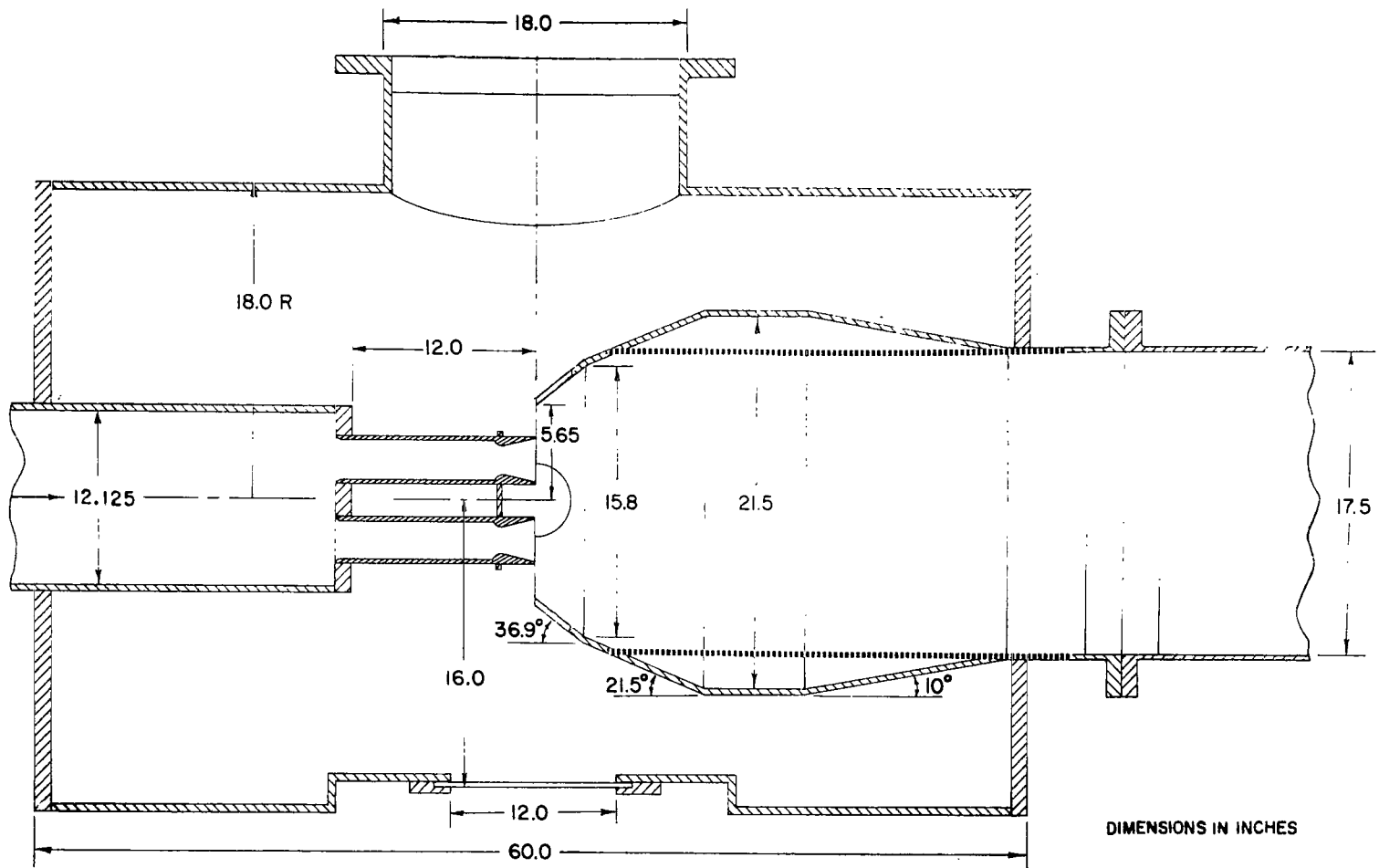
FIGURE 4.   TEST CELL-DIFFUSER-MODEL SCHEMATIC

DIMENSIONS IN INCHES
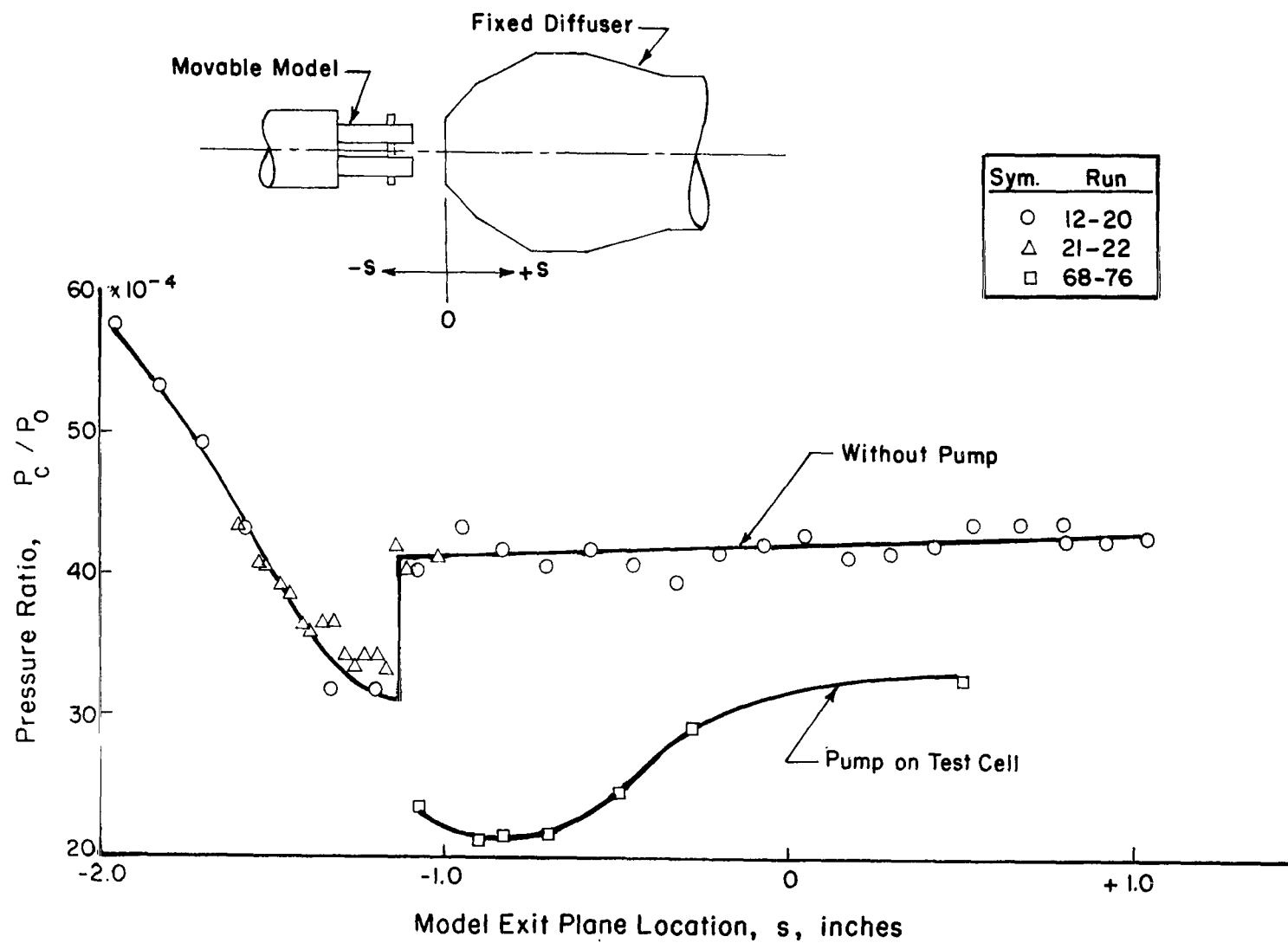
FIGURE 5.   OPTIMIZATION OF MODEL LOCATION RELATIVE TO
DIFFUSER ENTRANCE

Diffuser

Heat Shield

Static Pressure Taps on Nozzle
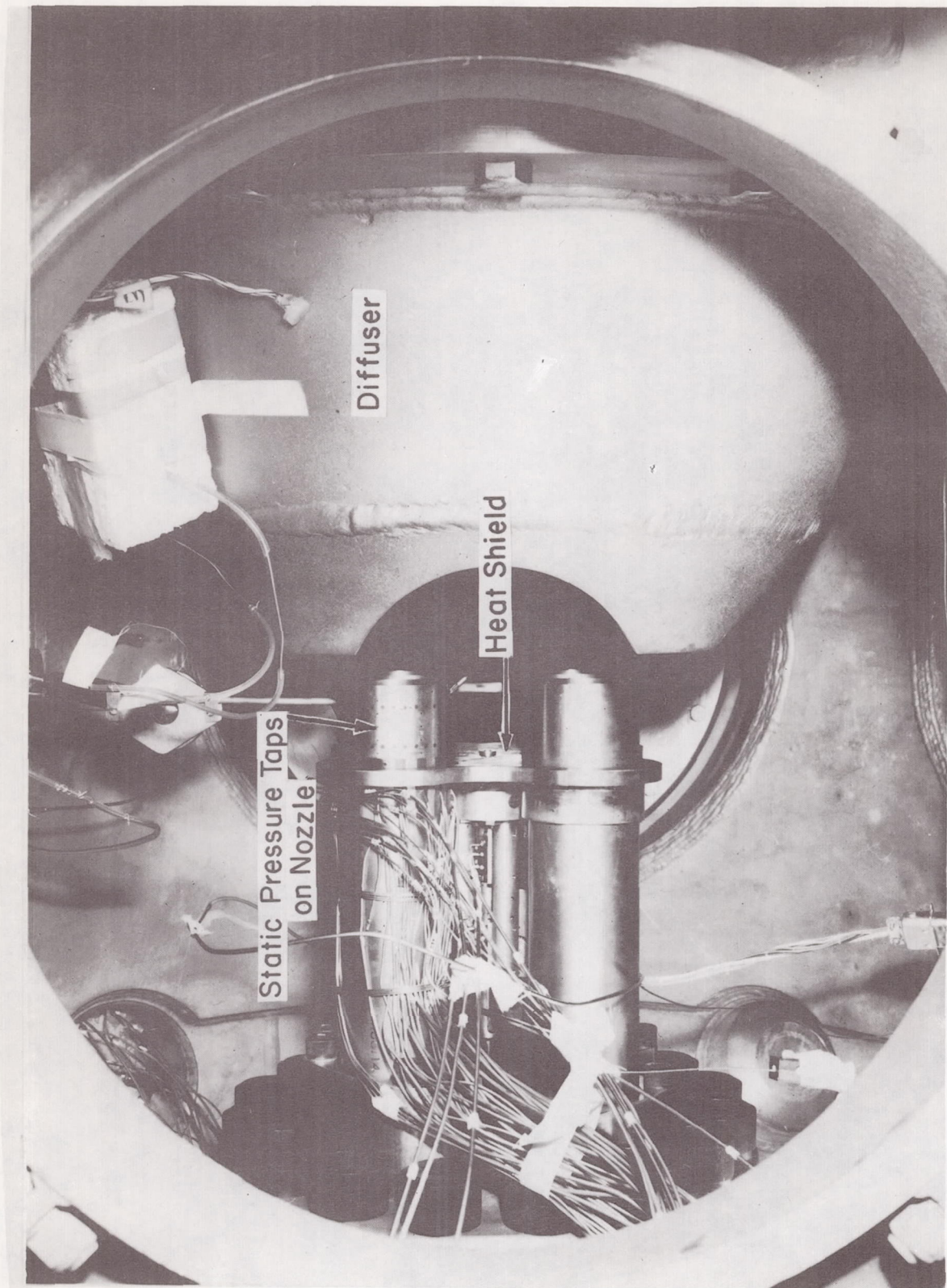
FIGURE 6. PHOTOGRAPH OF MODEL AND DIFFUSER

27

Vacuum Sphere

Tunnel "E"

18" Valve

20° "Y" Section

Window ℄

Centerline 5 ft. Above Floor

24" O.D. Duct

18" O.D. Duct

36" Test Cell

I. T. Building

```
0   2   4   6   8   10
```
scale in feet
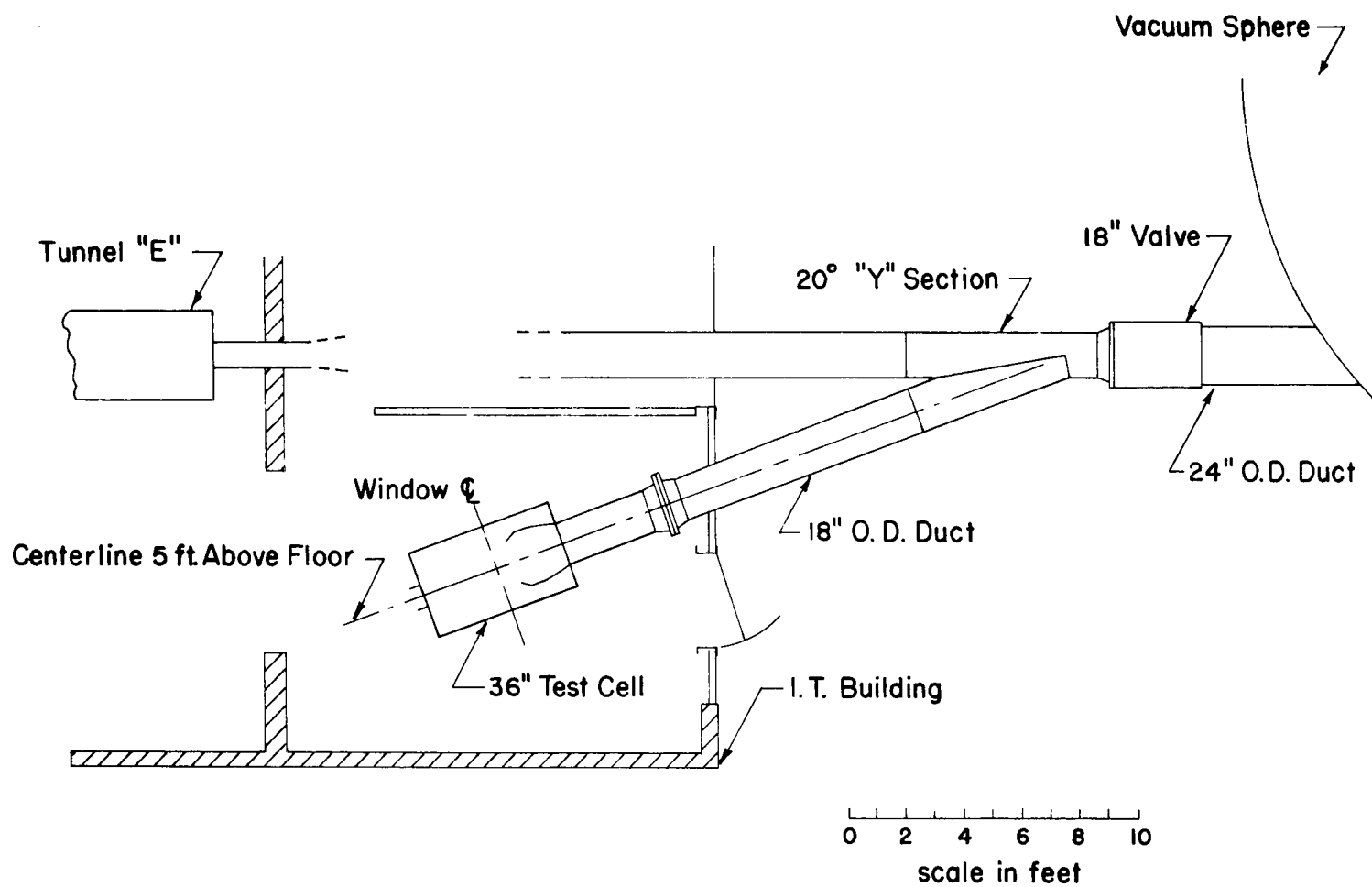
FIGURE 7.   SCHEMATIC OF TEST SET-UP AT VKF AREA "E"

High Pressure
Dry Air
Bottle

200,000 cu. ft.
Vacuum
Sphere

Model, Test Cell, & Ejector

Valve A

Valve B

Atmospheric
Inbleed
Valve

Valve C

Valve E

Vacuum
Pump

Exhaust
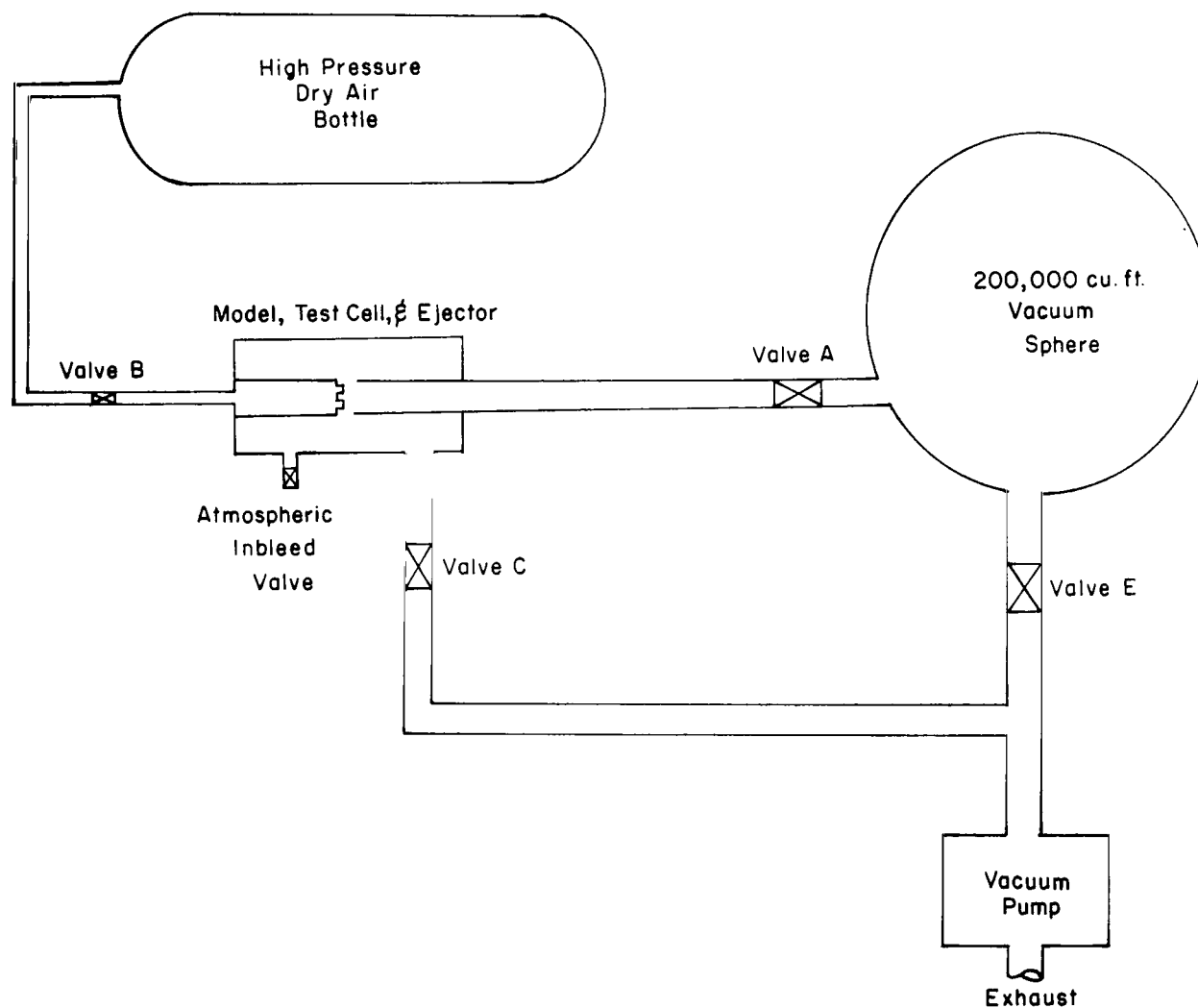
FIGURE 8.   VALVE LOCATIONS AND NOMENCLATURE

0.385"

Solder
Fillets

0.190"

30°

0.075"

0.025"

0.275"

Wire Shaft
0.011" Dia.

Stainless Steel Tubing
0.030" O.D. and 0.020" I.D.

Solder Fillets

Brass Round Stock
0.065" Dia.

End View (Partial)

0.008"
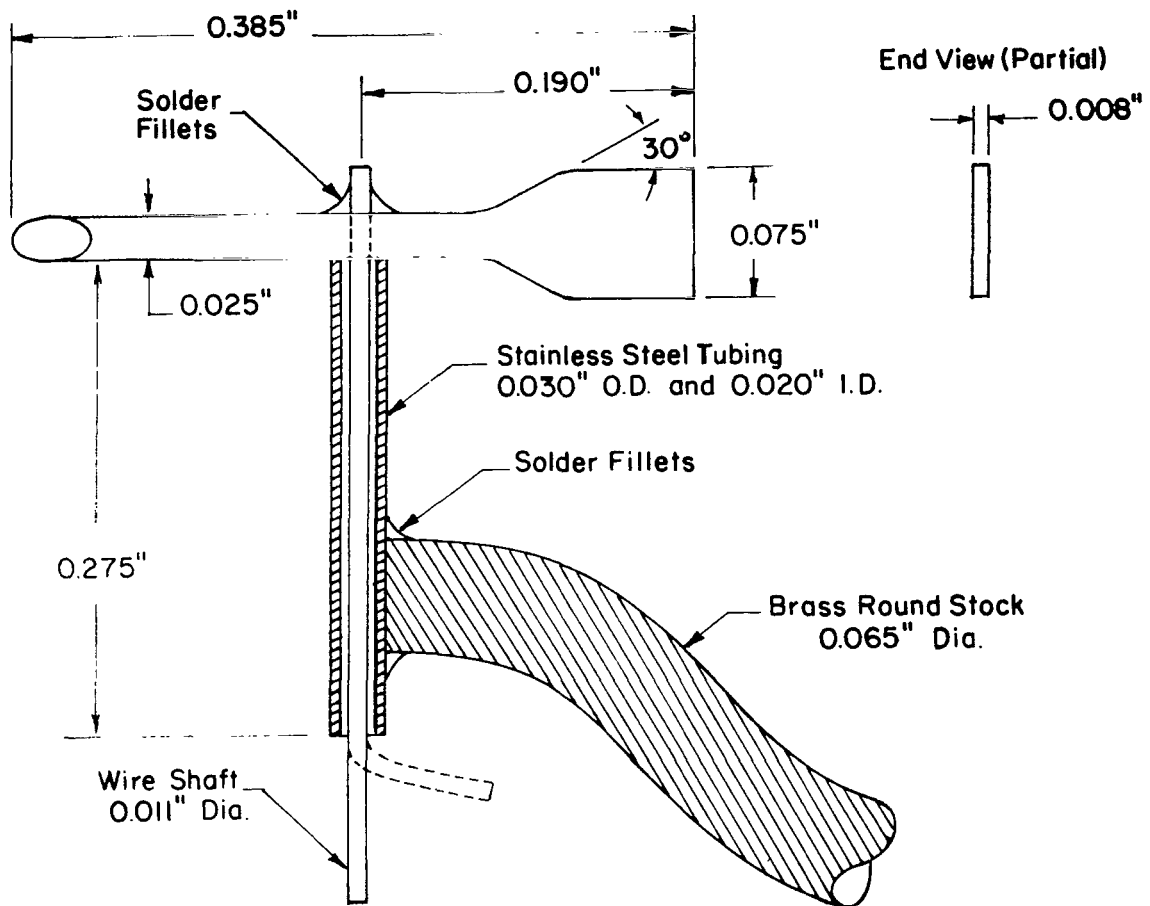
Note: Vane Not Shown in Cross Section
Approximate Scale: I inch = 0.10 inch

FIGURE 9. SCHEMATIC OF WIND VANE
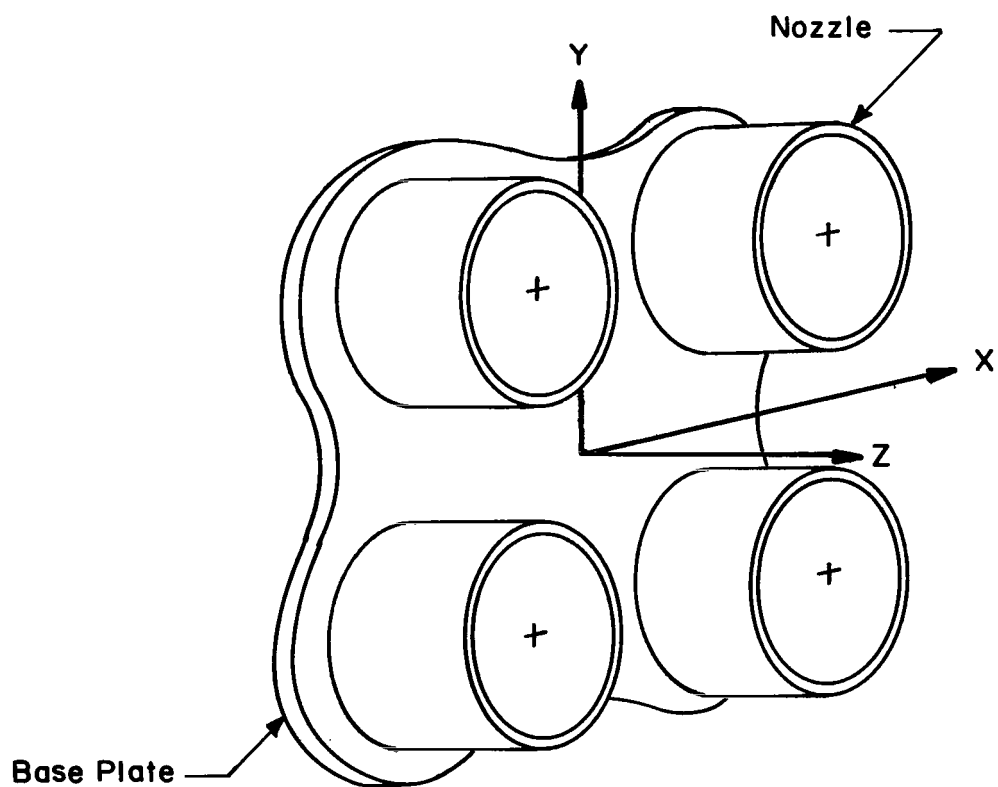
FIGURE 10.   COORDINATE SYSTEM
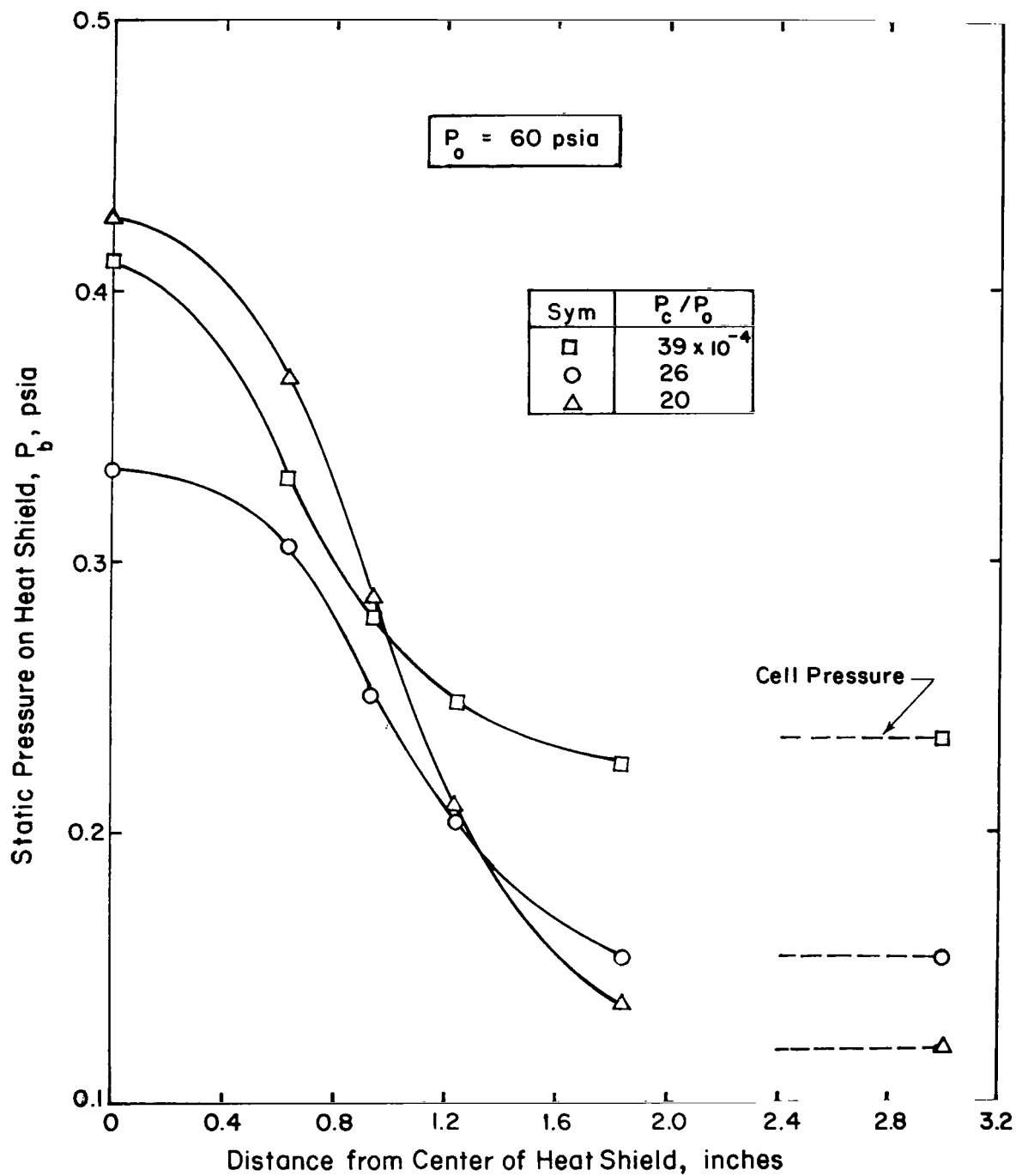
FIGURE 11.   PRESSURE DISTRIBUTIONS ON HEAT SHIELD
ALONG RADIAL LINE BETWEEN NOZZLES
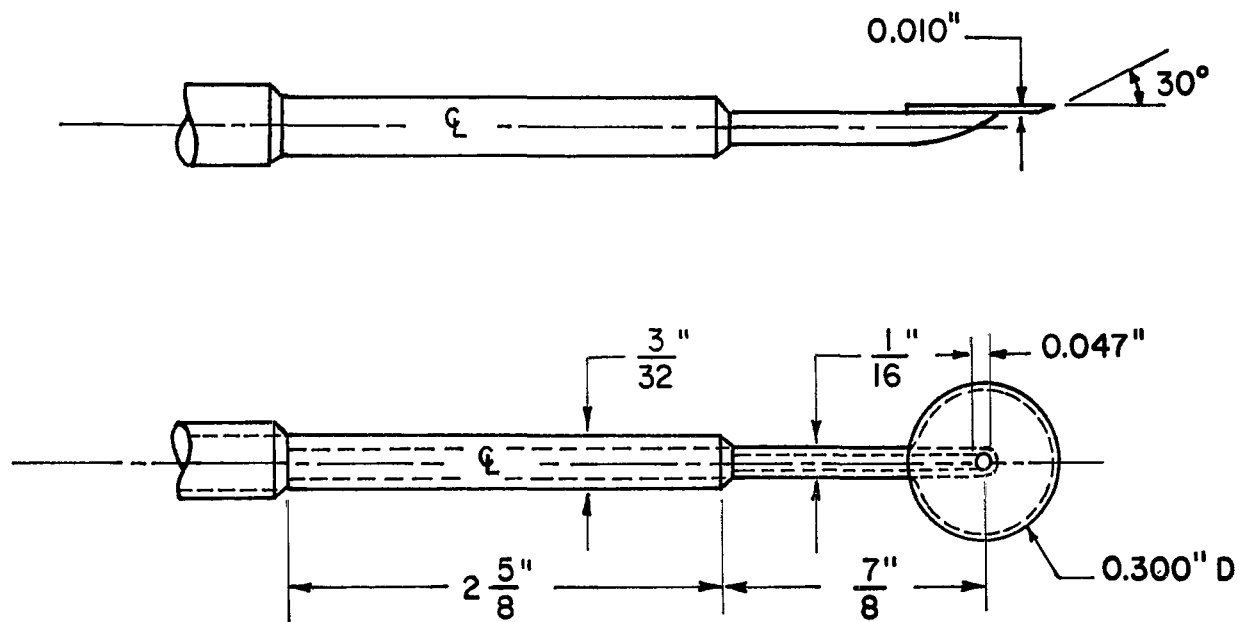
FIGURE 12.   SCHEMATIC OF STATIC PRESSURE PROBE
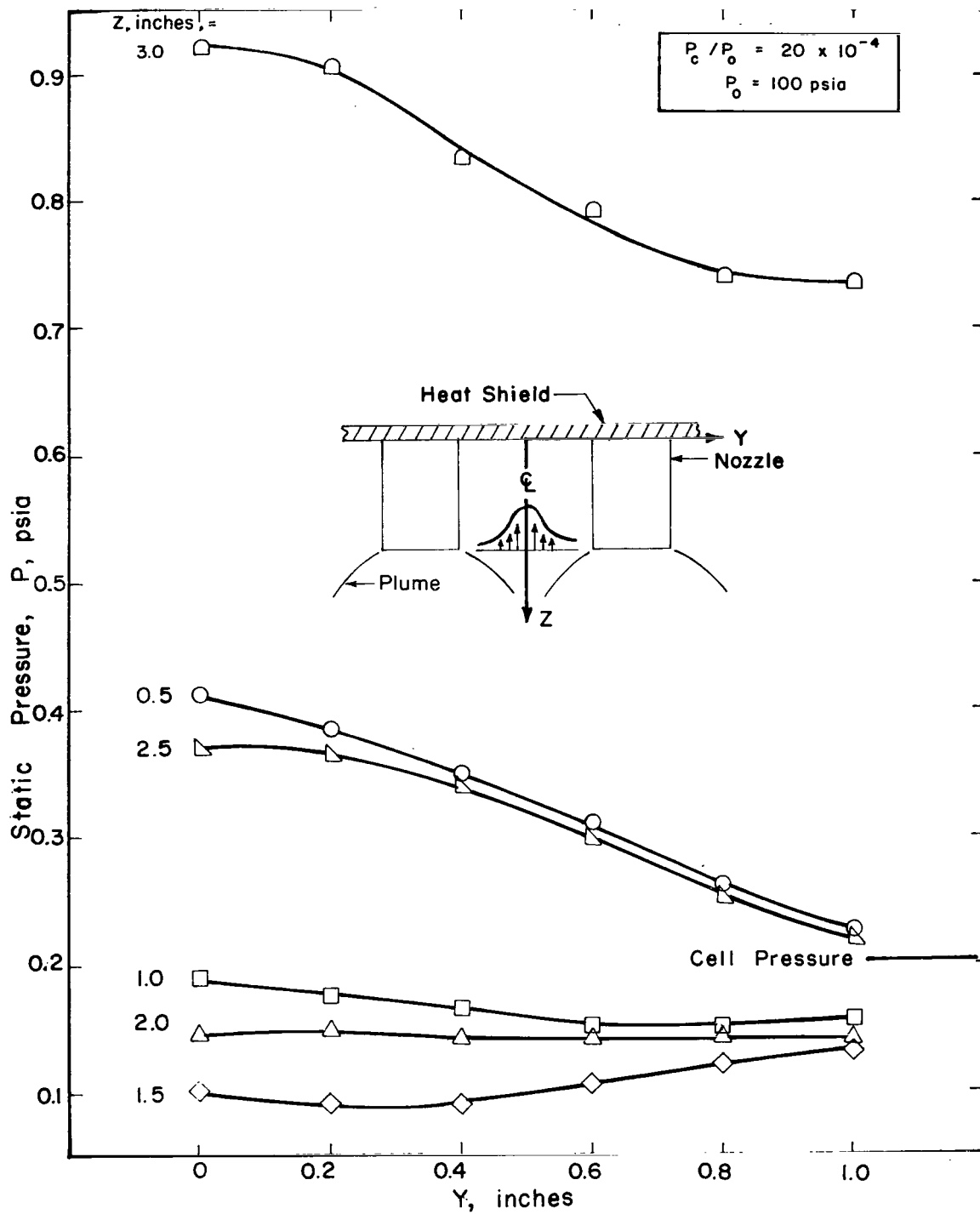
FIGURE 13.   STATIC PRESSURE IN REVERSE JET
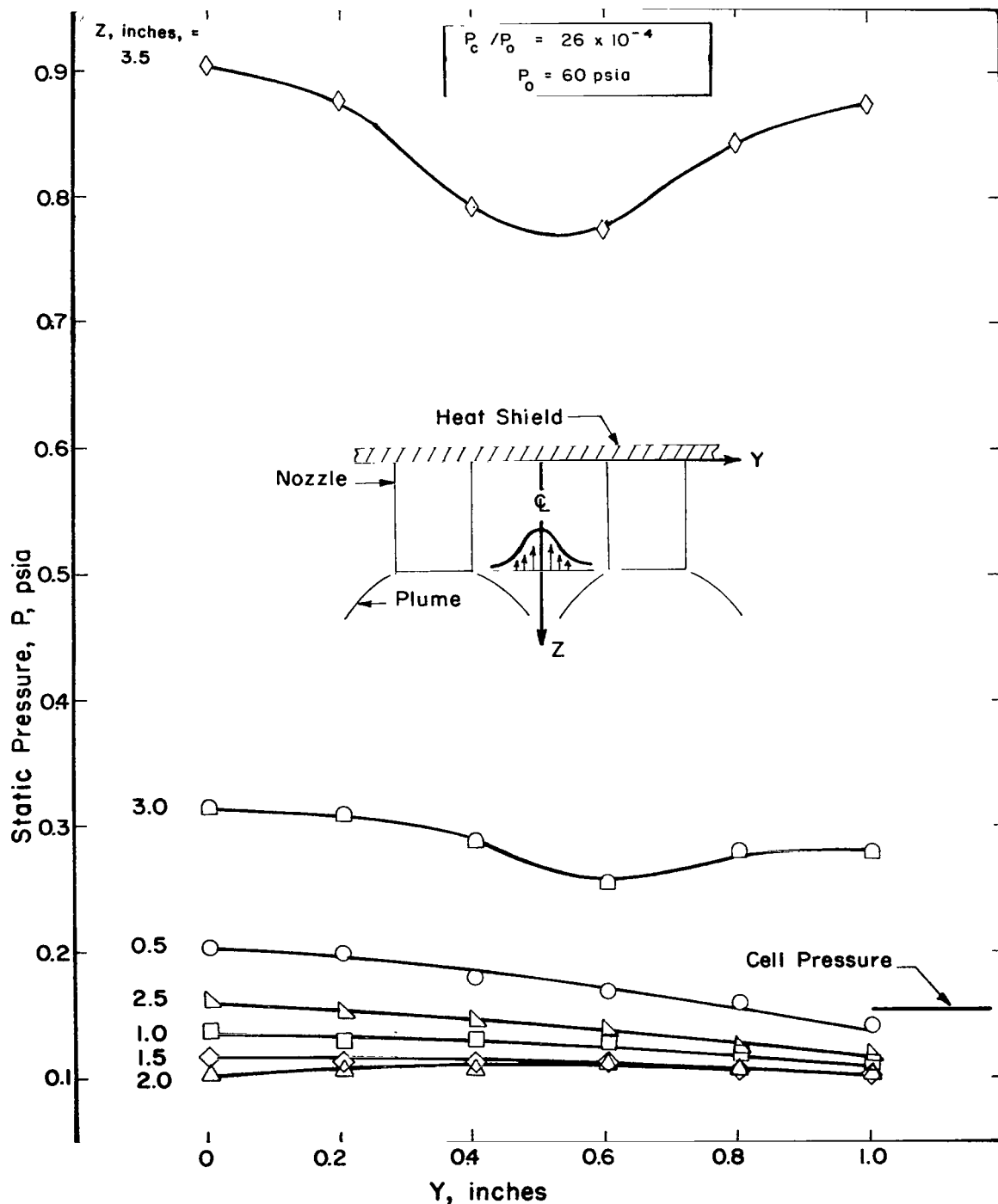
FIGURE 14.   STATIC PRESSURE IN REVERSE JET
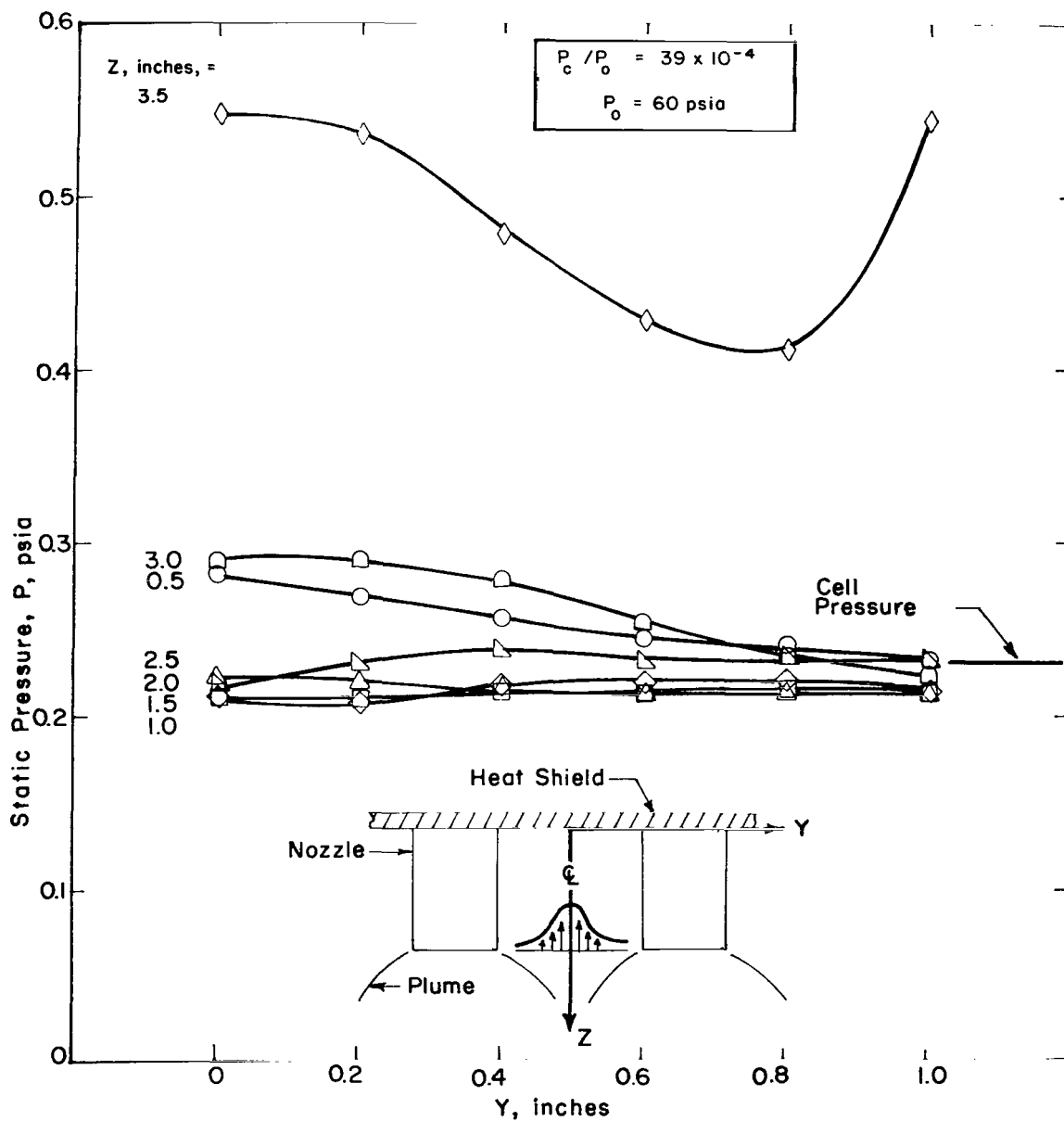
FIGURE 15. STATIC PRESSURE IN REVERSE JET

Coordinates in inches
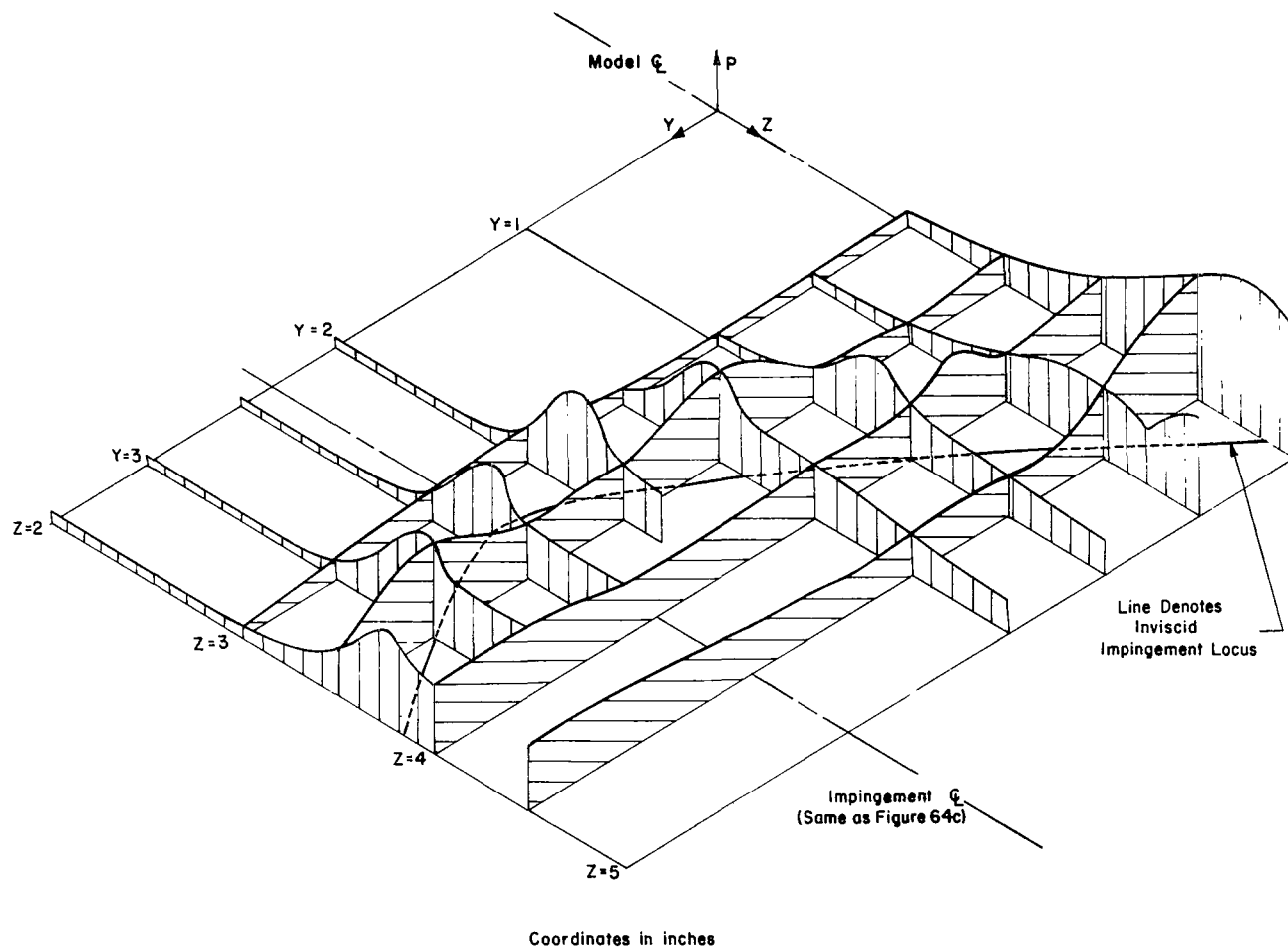
FIGURE 16. STATIC PRESSURE FIELD IN PLANE OF IMPINGEMENT
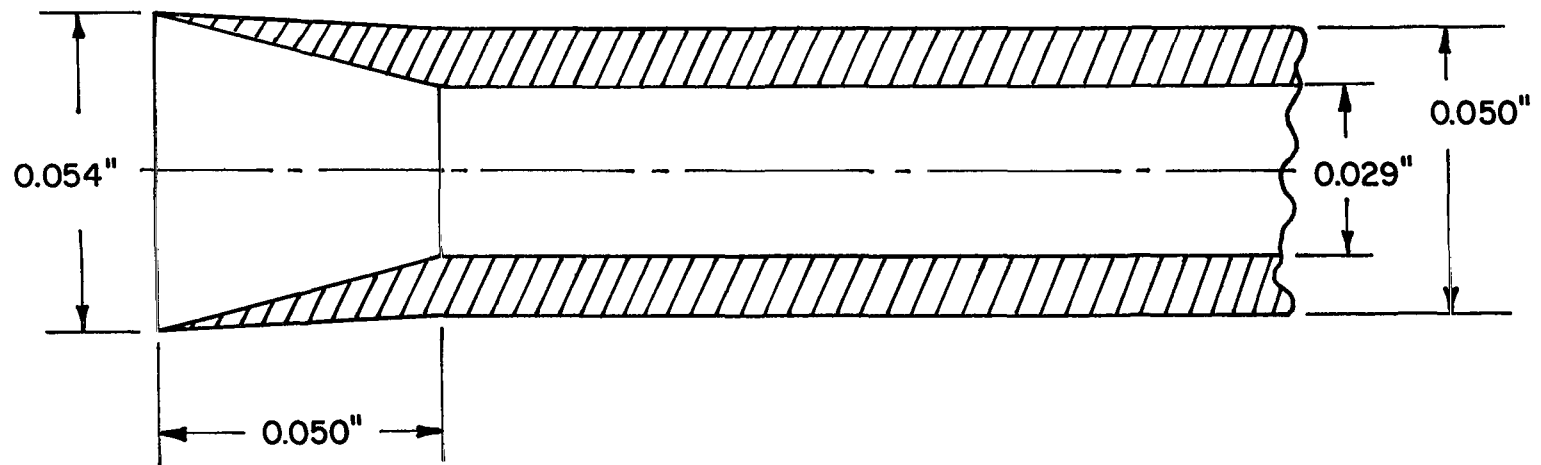
Note: Total Included Angle of Inlet = 28°
Approximate Scale: I inch = 0.0333 inch

FIGURE 17. GEOMETRY OF IMPACT PRESSURE TUBE INLET
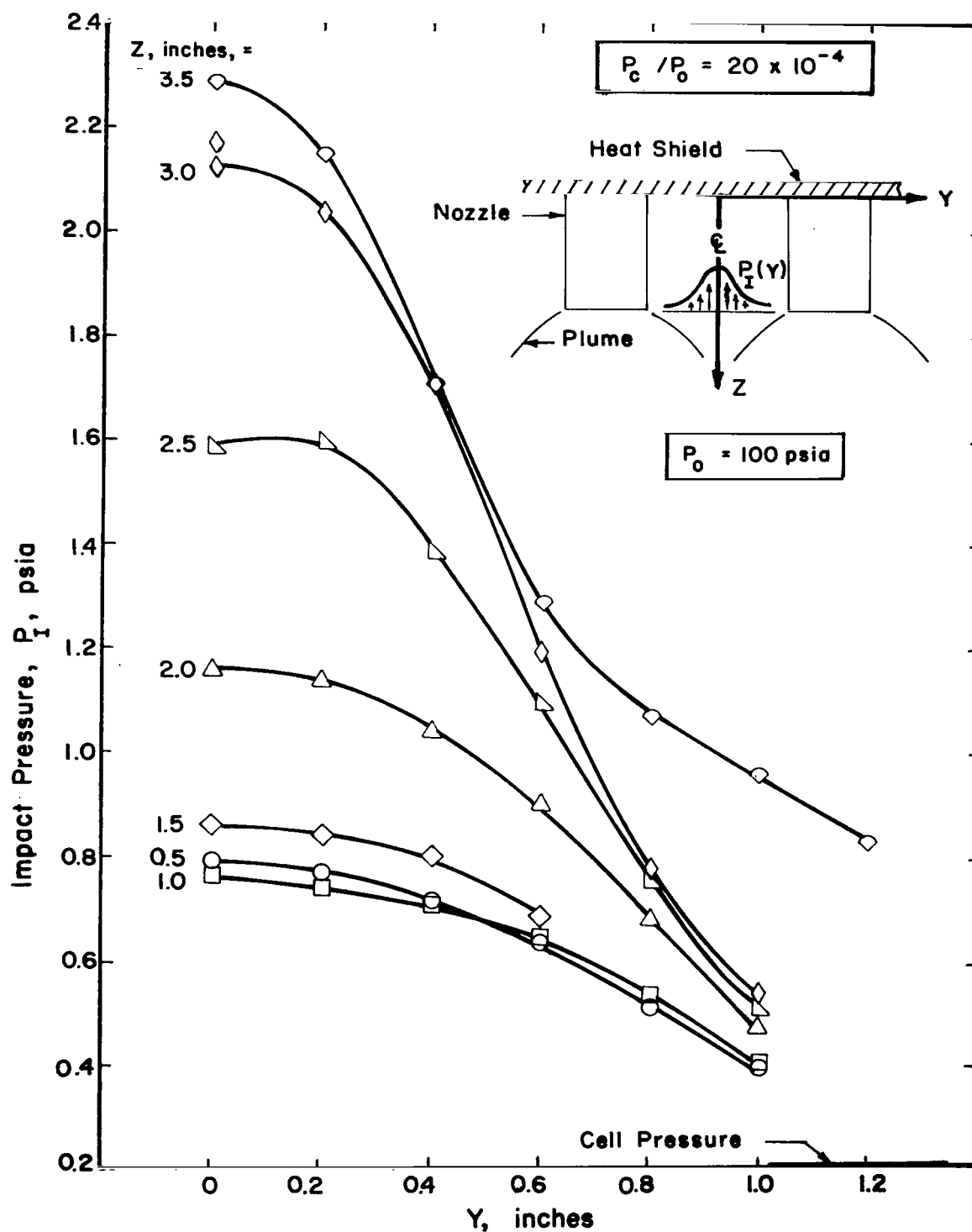
FIGURE 18. IMPACT PRESSURE IN REVERSE JET
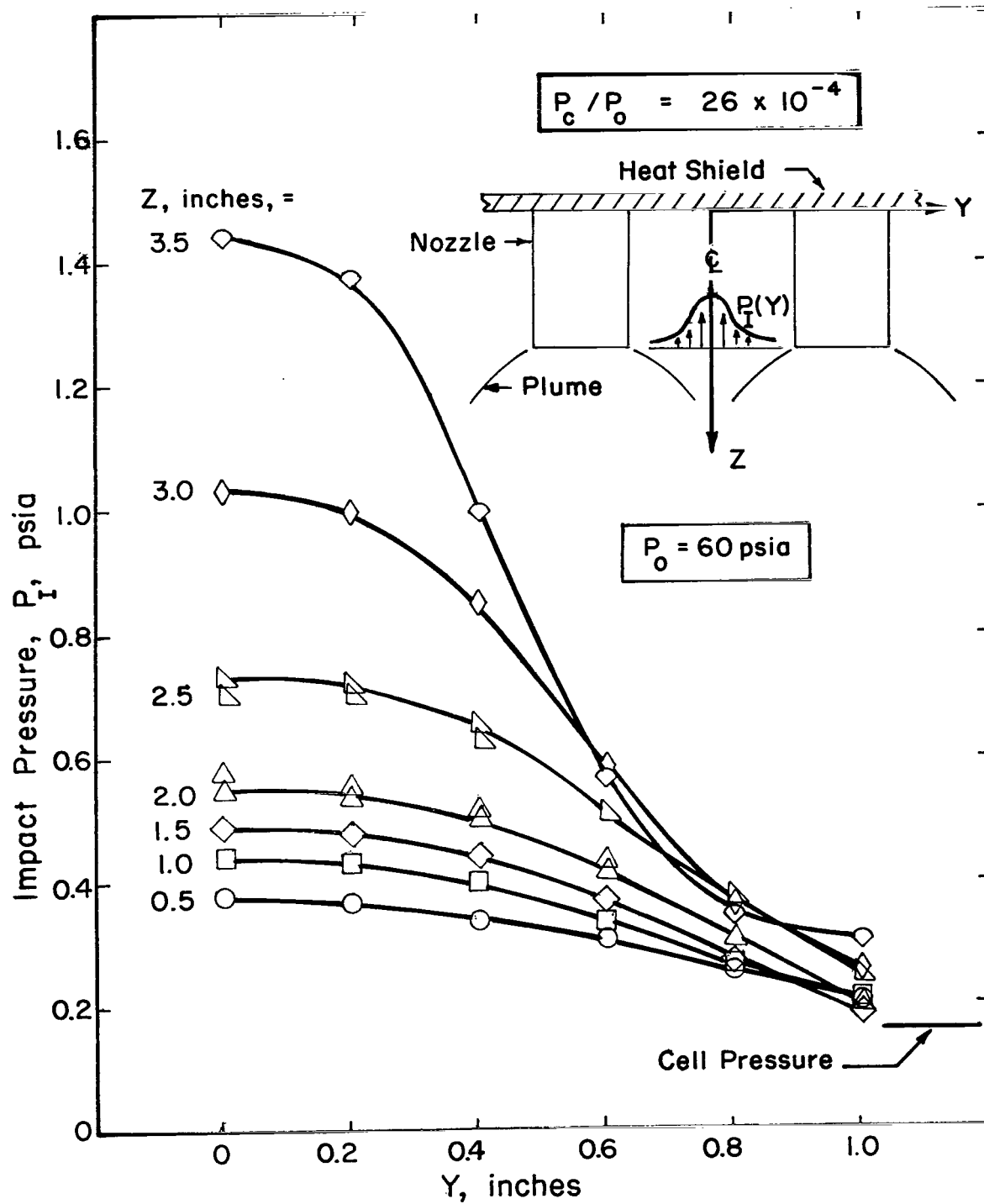
FIGURE 19. IMPACT PRESSURE IN REVERSE JET
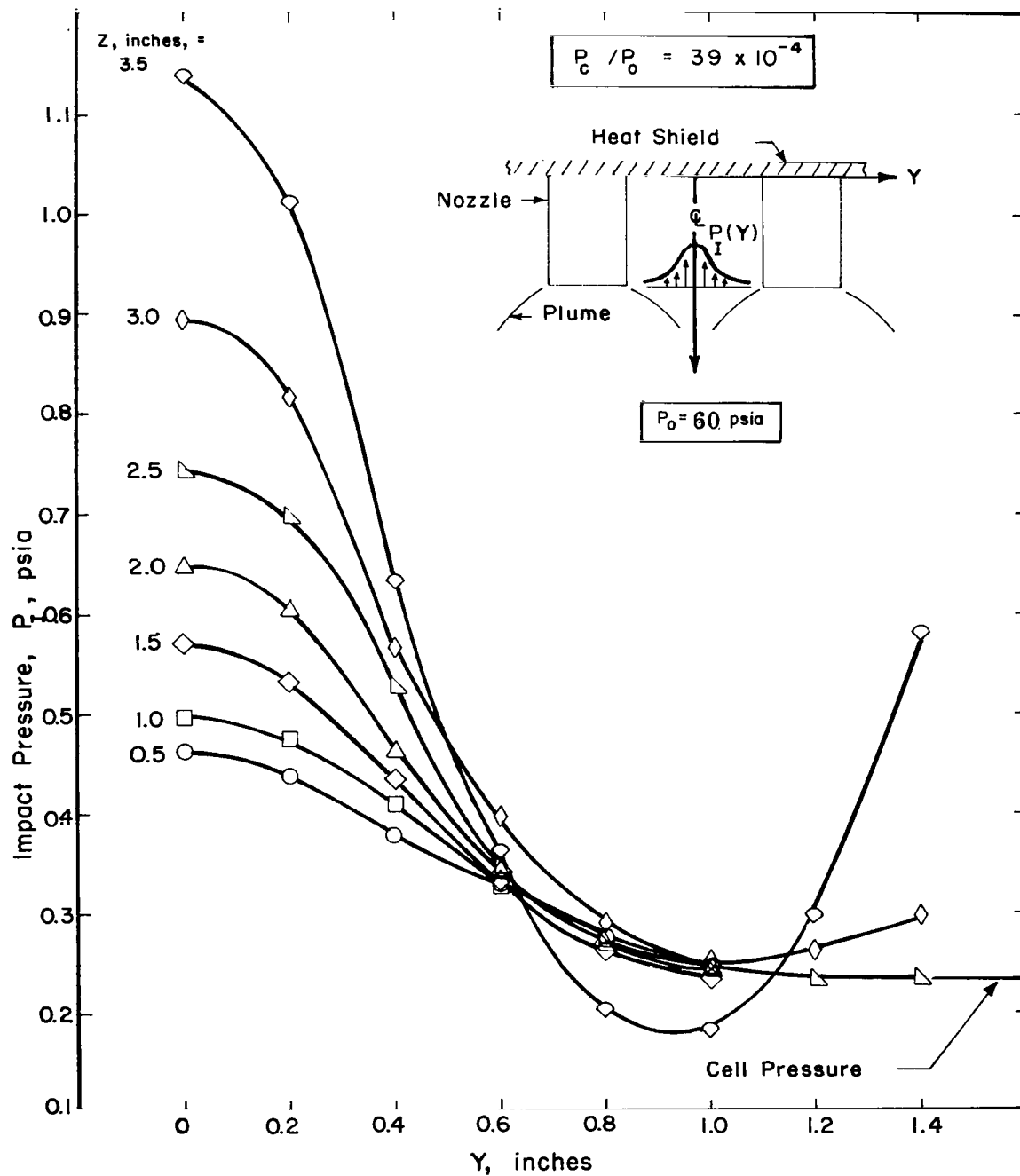
FIGURE 20.   IMPACT PRESSURE IN REVERSE JET
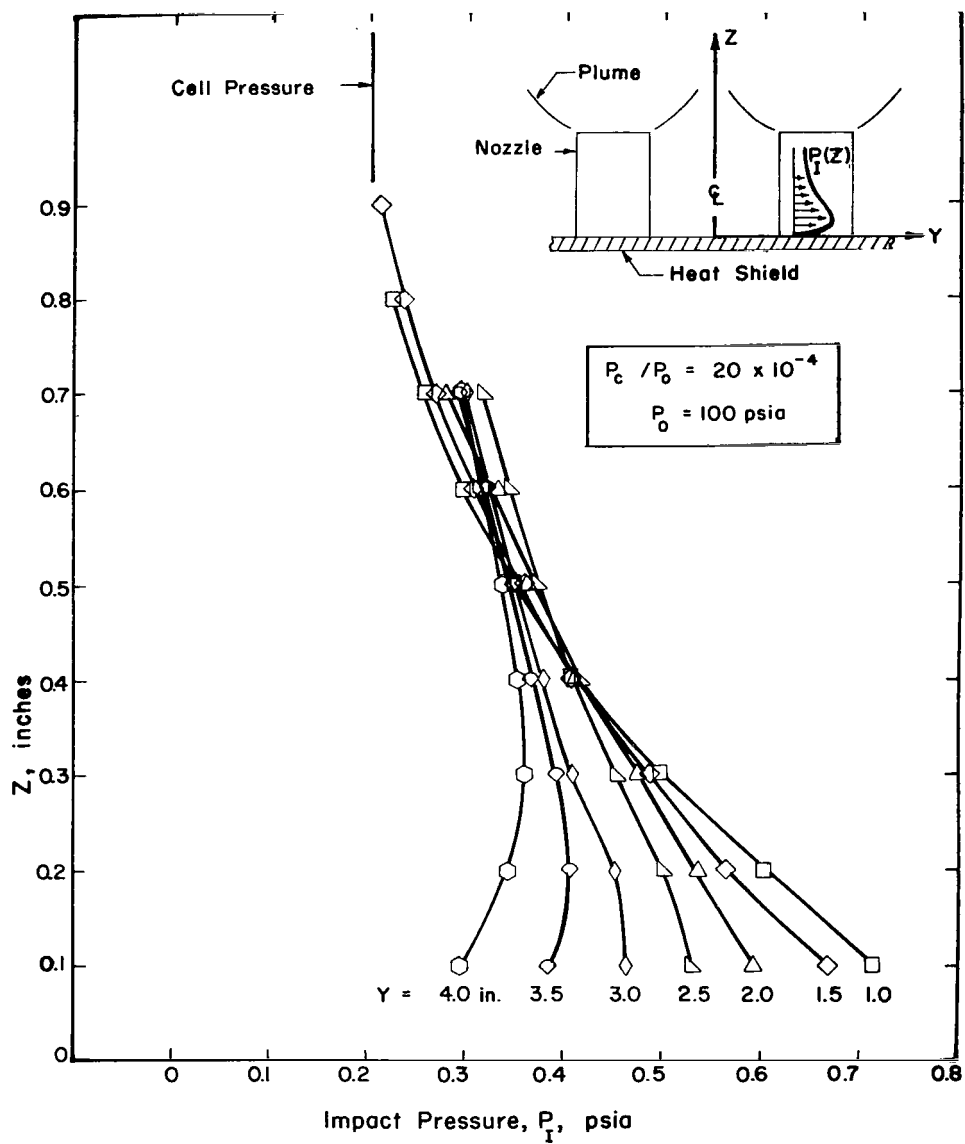
FIGURE 21.   IMPACT PRESSURE IN WALL JET
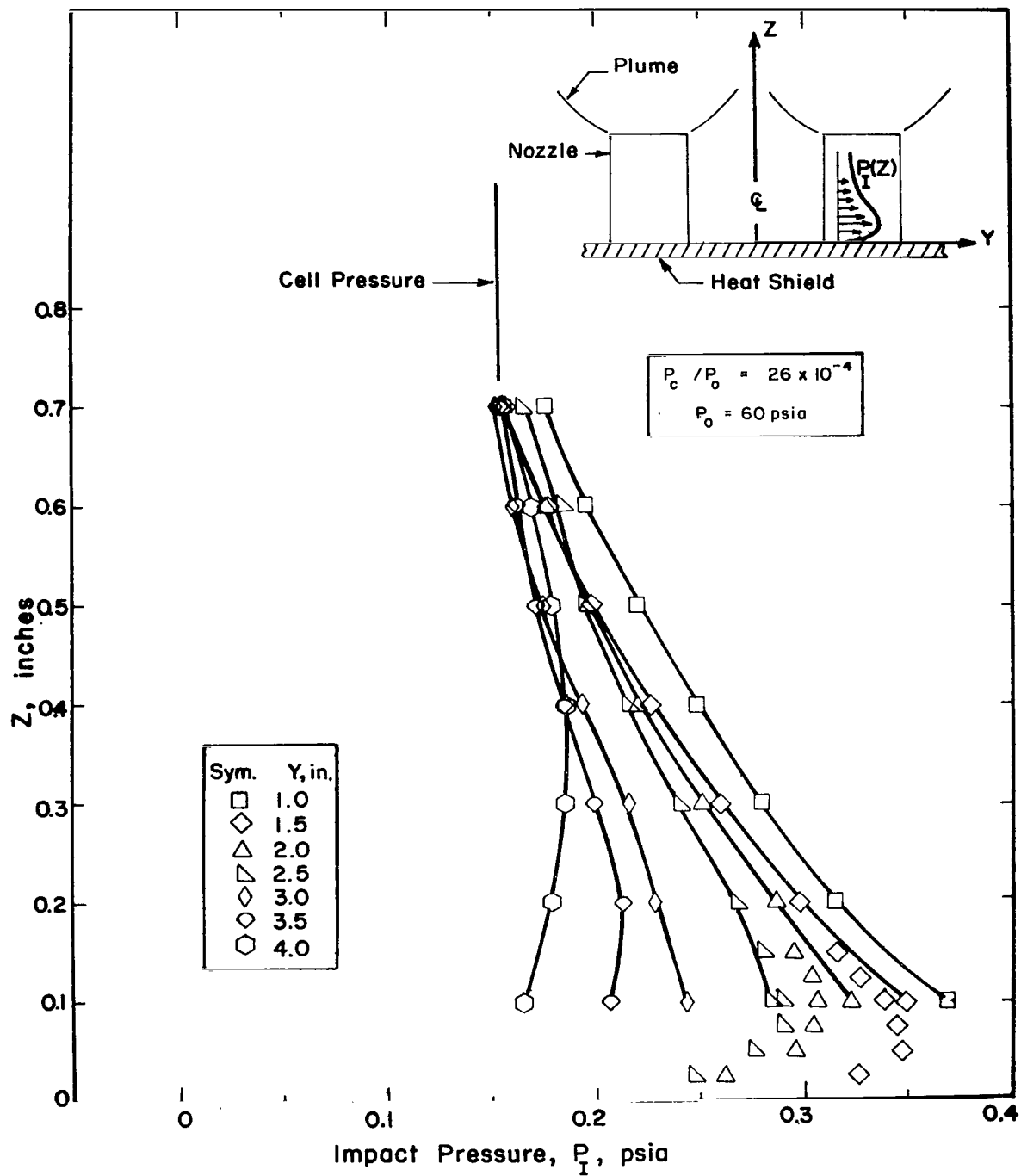
FIGURE 22. IMPACT PRESSURE IN WALL JET
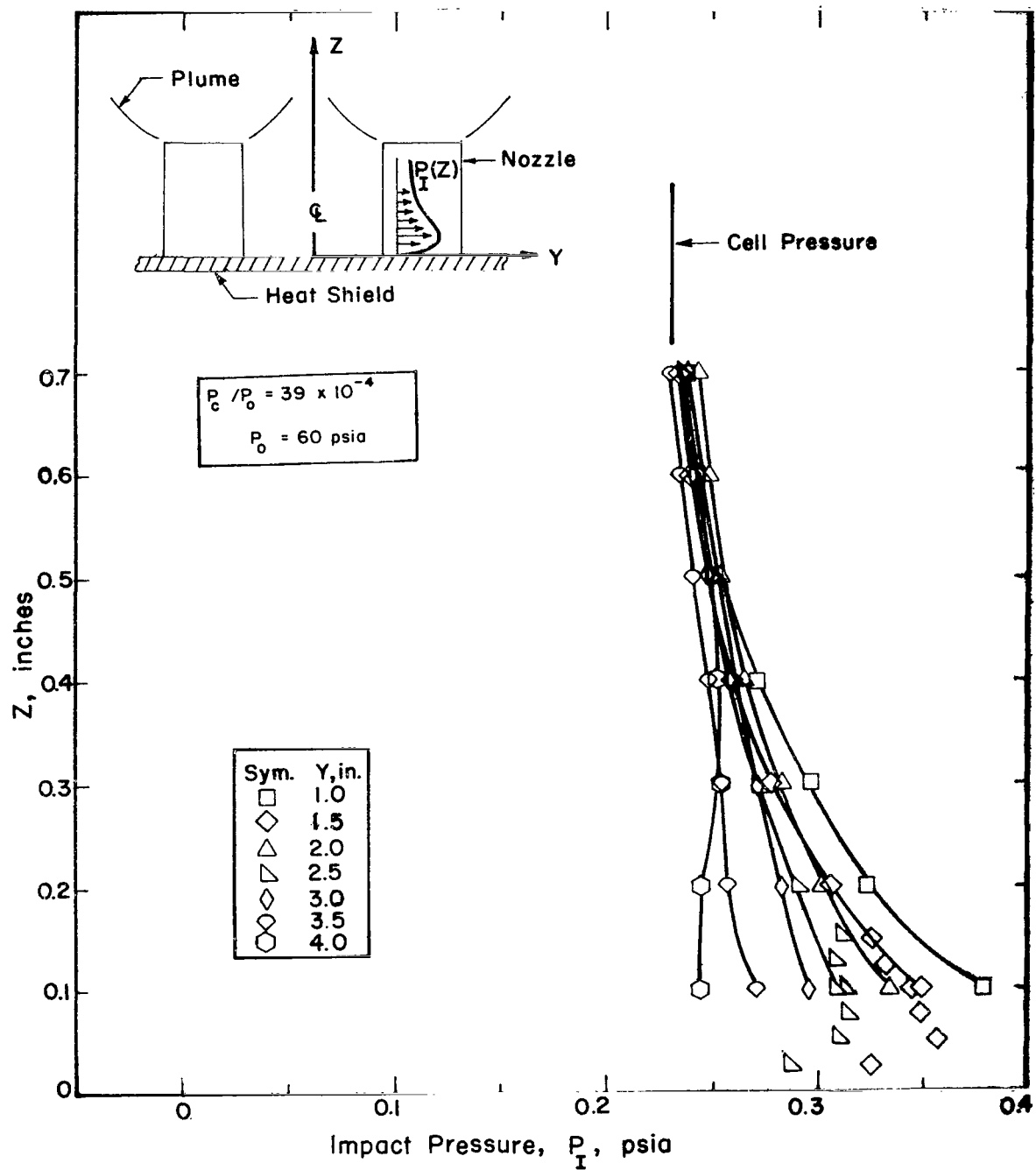
FIGURE 23.   IMPACT PRESSURE IN WALL JET

$$P_c / P_o = 20 \times 10^{-4}$$

$$P_o = 60 \text{ psia}$$

Streamline Flow Directions

Inviscid Plume Impingement Line

Nozzle

Nozzle

Heat Shield

Impact Pressure Scale: 0 1 2 3 4 psia

Geometric Scale: 0 1 inch
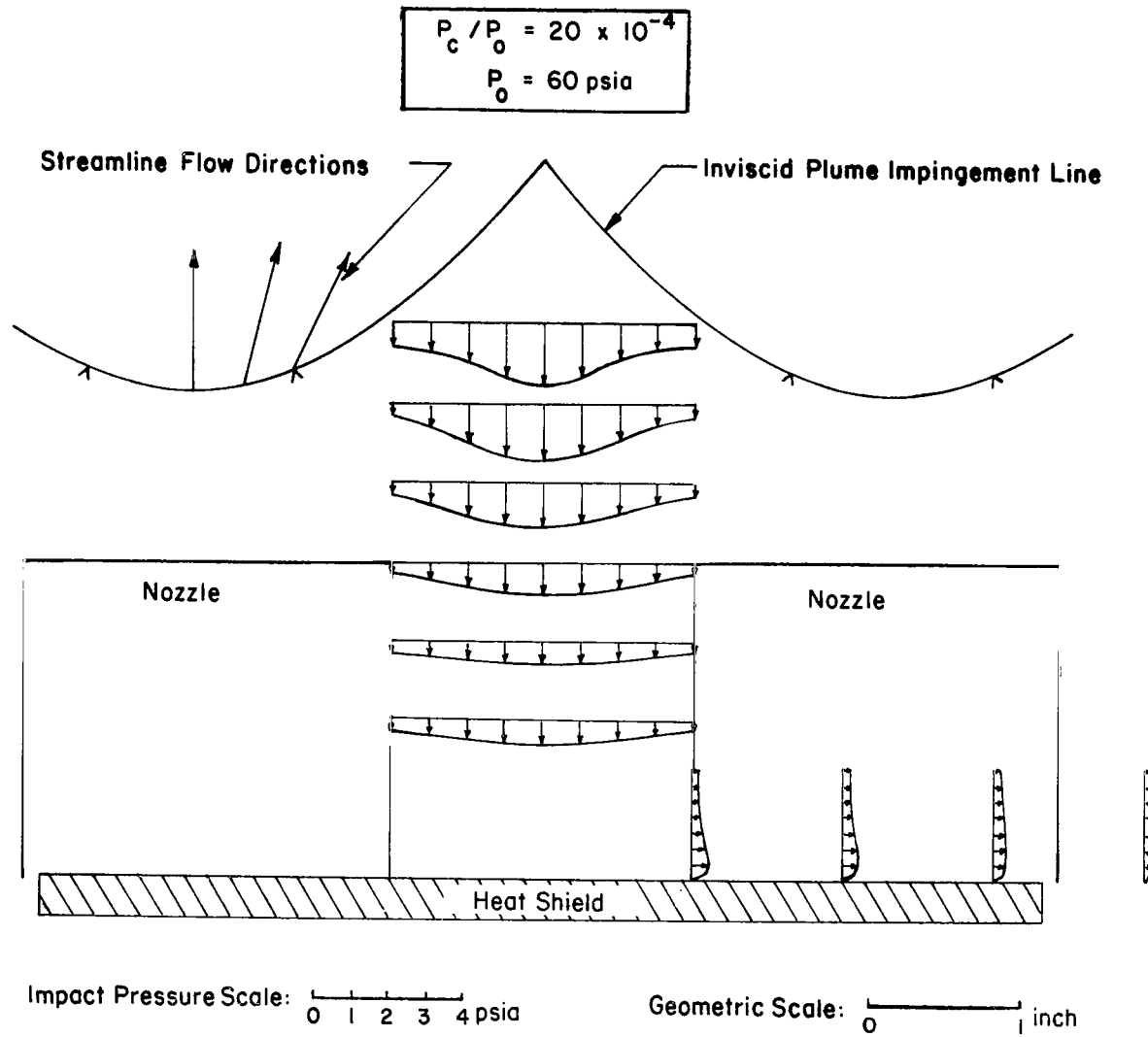
FIGURE 24. REVERSE JET AND WALL JET IMPACT PRESSURE PROFILES

$$P_c / P_0 = 26 \times 10^{-4}$$
$$P_0 = 60 \text{ psia}$$

Streamline Flow Directions

Inviscid Plume Impingement Line

Nozzle

Nozzle

Heat Shield

Impact Pressure Scale:

0 1 2 3 4 psia

Geometric Scale:

0   1 inch
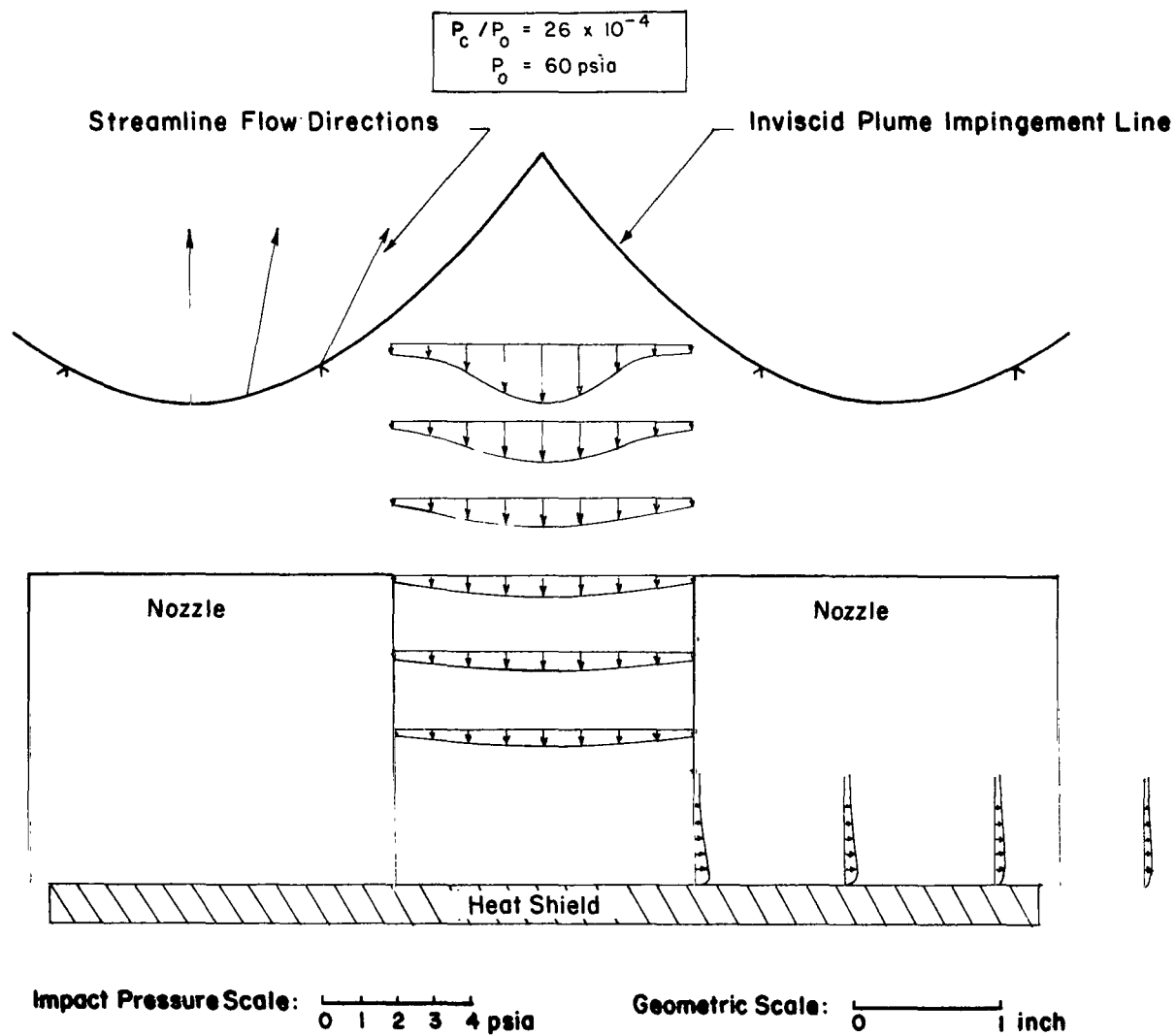
FIGURE 25.   REVERSE JET AND WALL JET IMPACT PRESSURE PROFILES

$$P_c / P_0 = 39 \times 10^{-4}$$
$$P_0 = 60 \text{ psia}$$

Streamline Flow Directions — Inviscid Plume Impingement Line

Nozzle

Nozzle

Heat Shield

Impact Pressure Scale: 0 1 2 3 4 psia

Geometric Scale: 0 ———— 1 inch
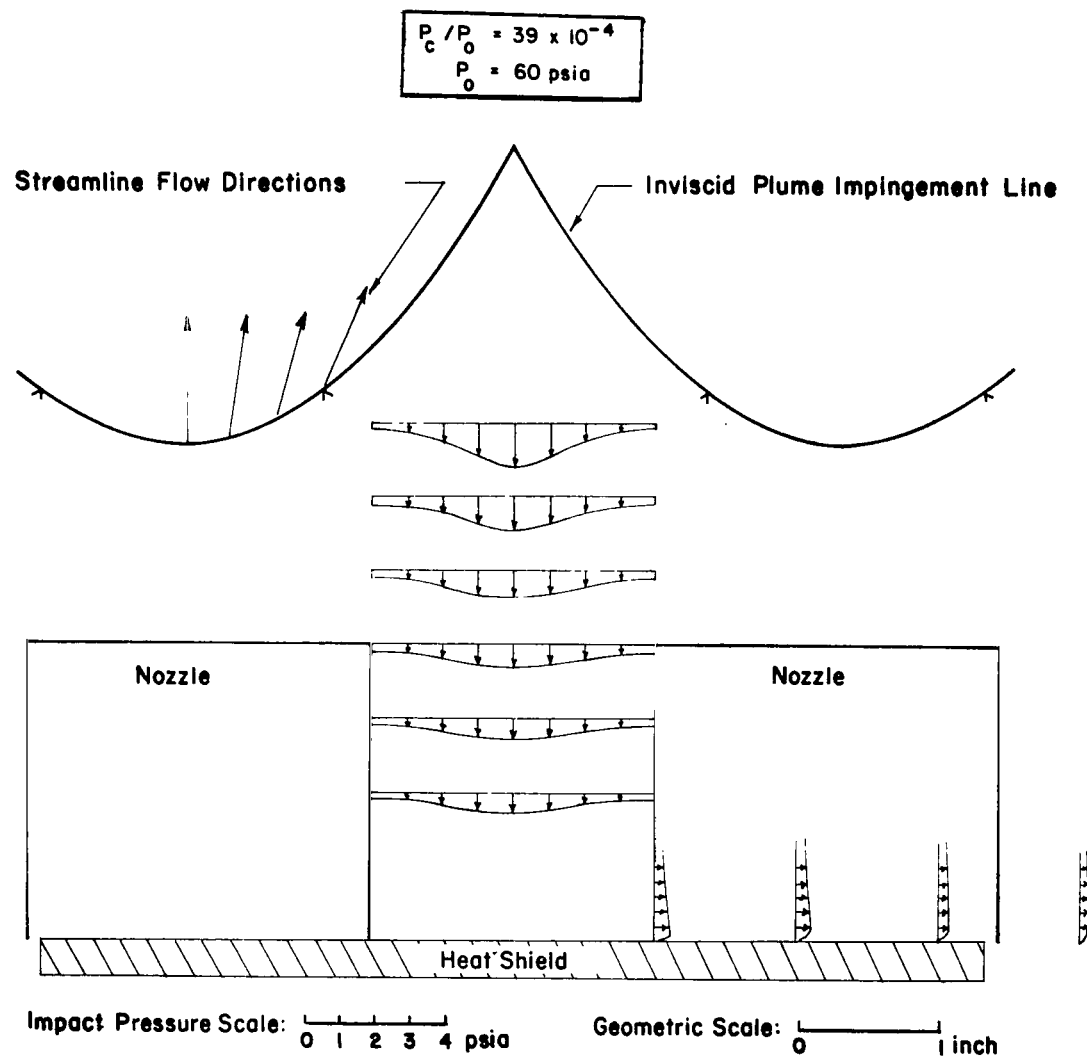
FIGURE 26. REVERSE JET AND WALL JET IMPACT PRESSURE PROFILES
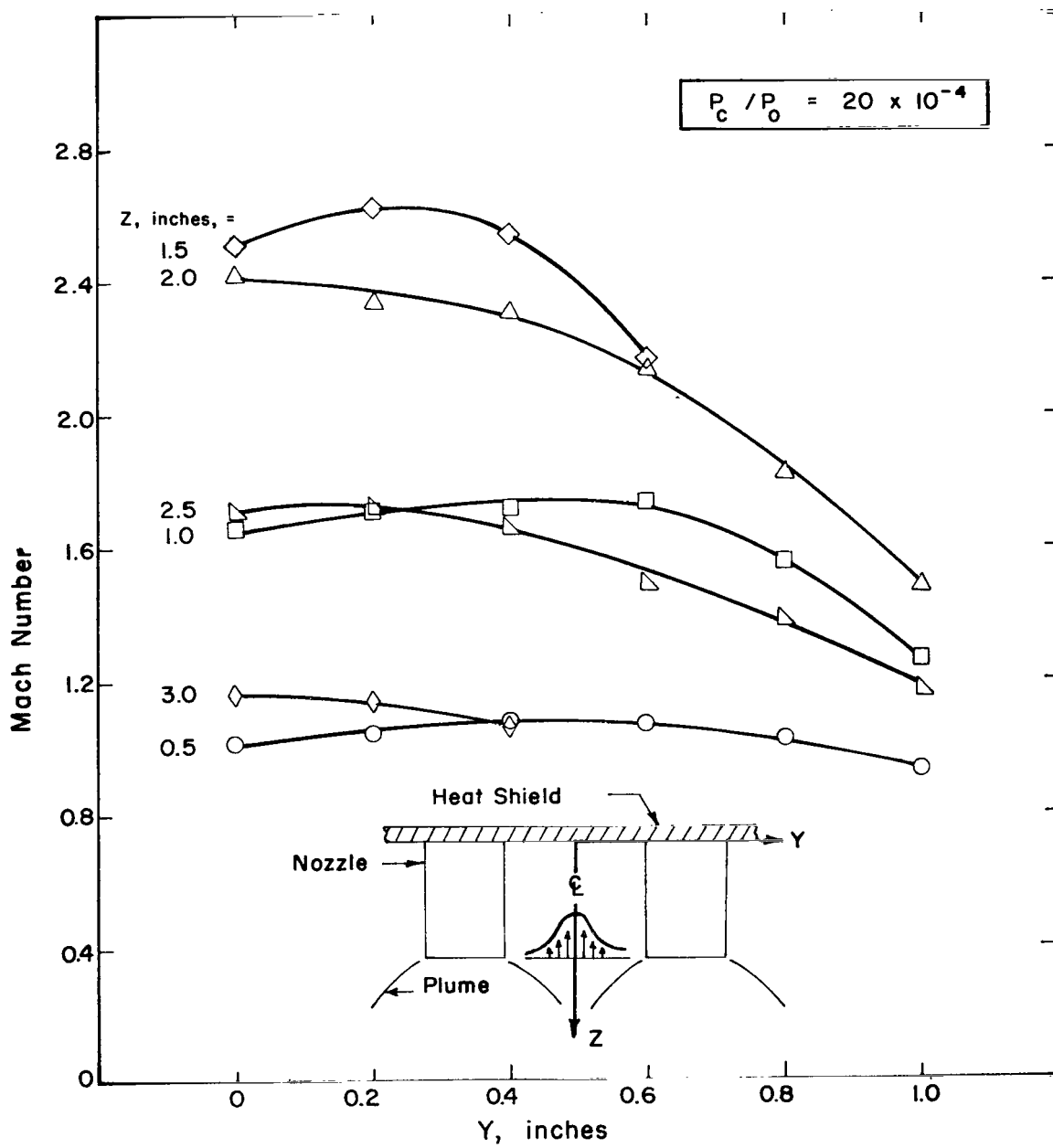
FIGURE 27. MACH NUMBER IN REVERSE JET
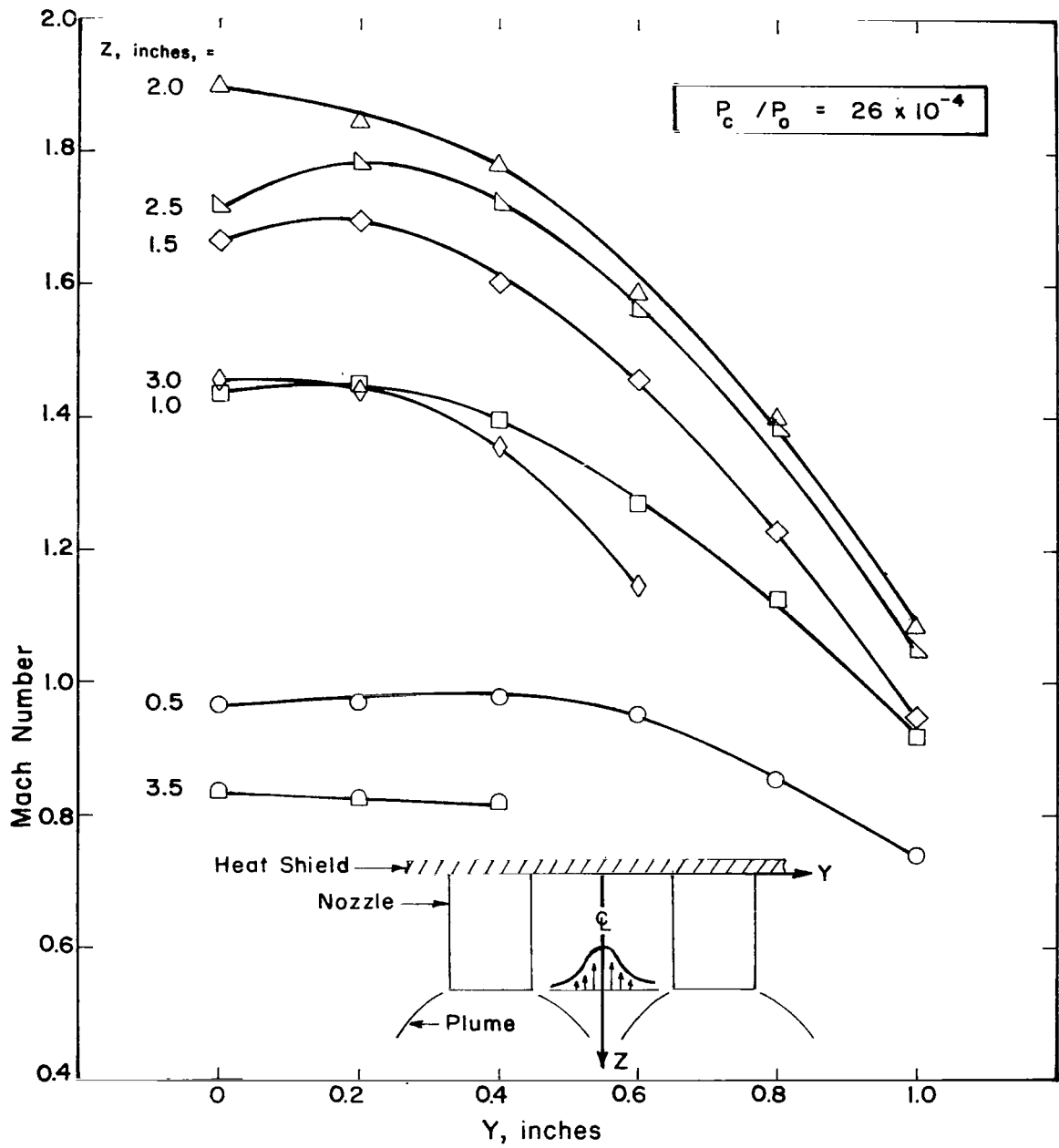
FIGURE 28.   MACH NUMBER IN REVERSE JET
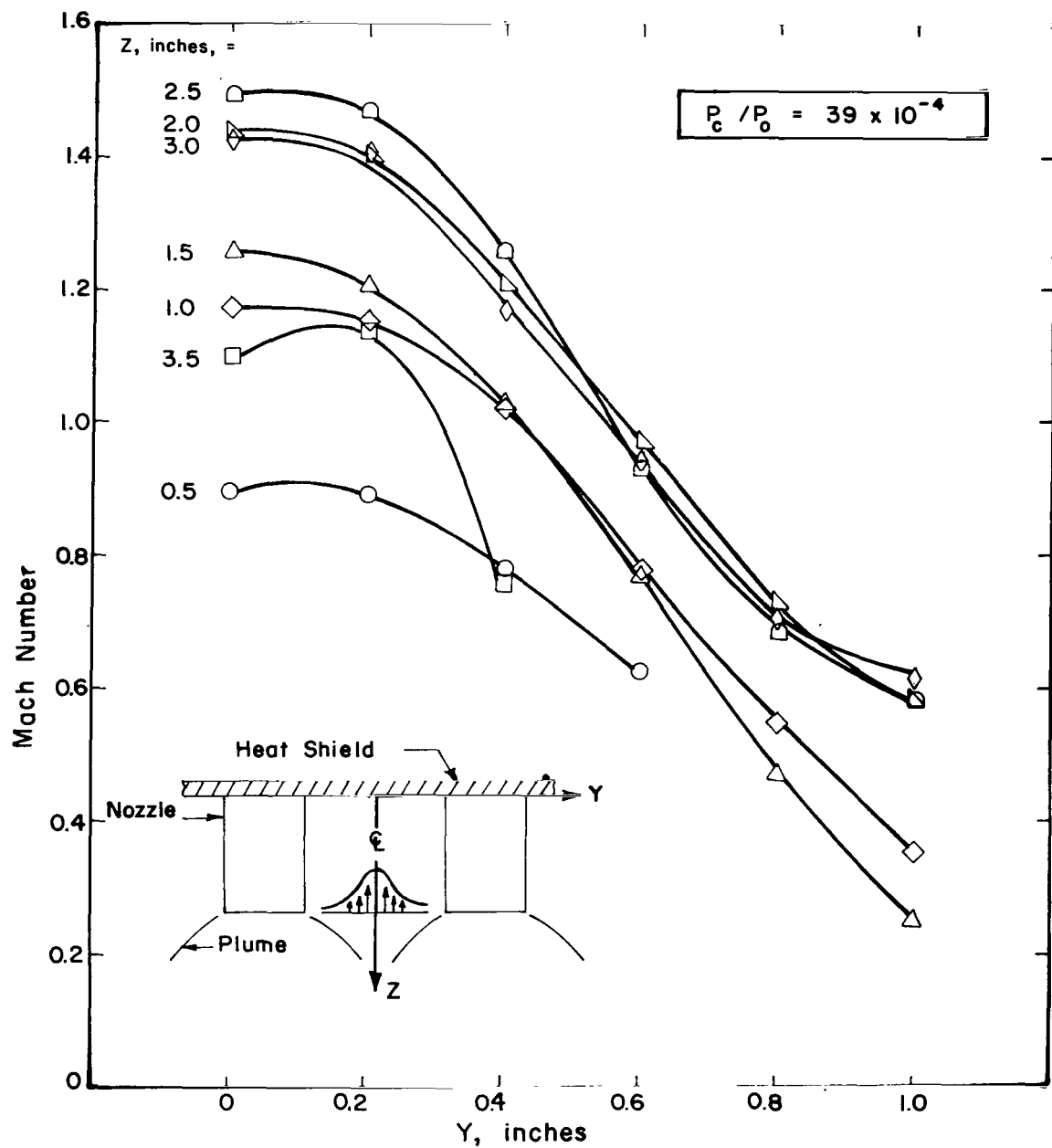
FIGURE 29.   MACH NUMBER IN REVERSE JET
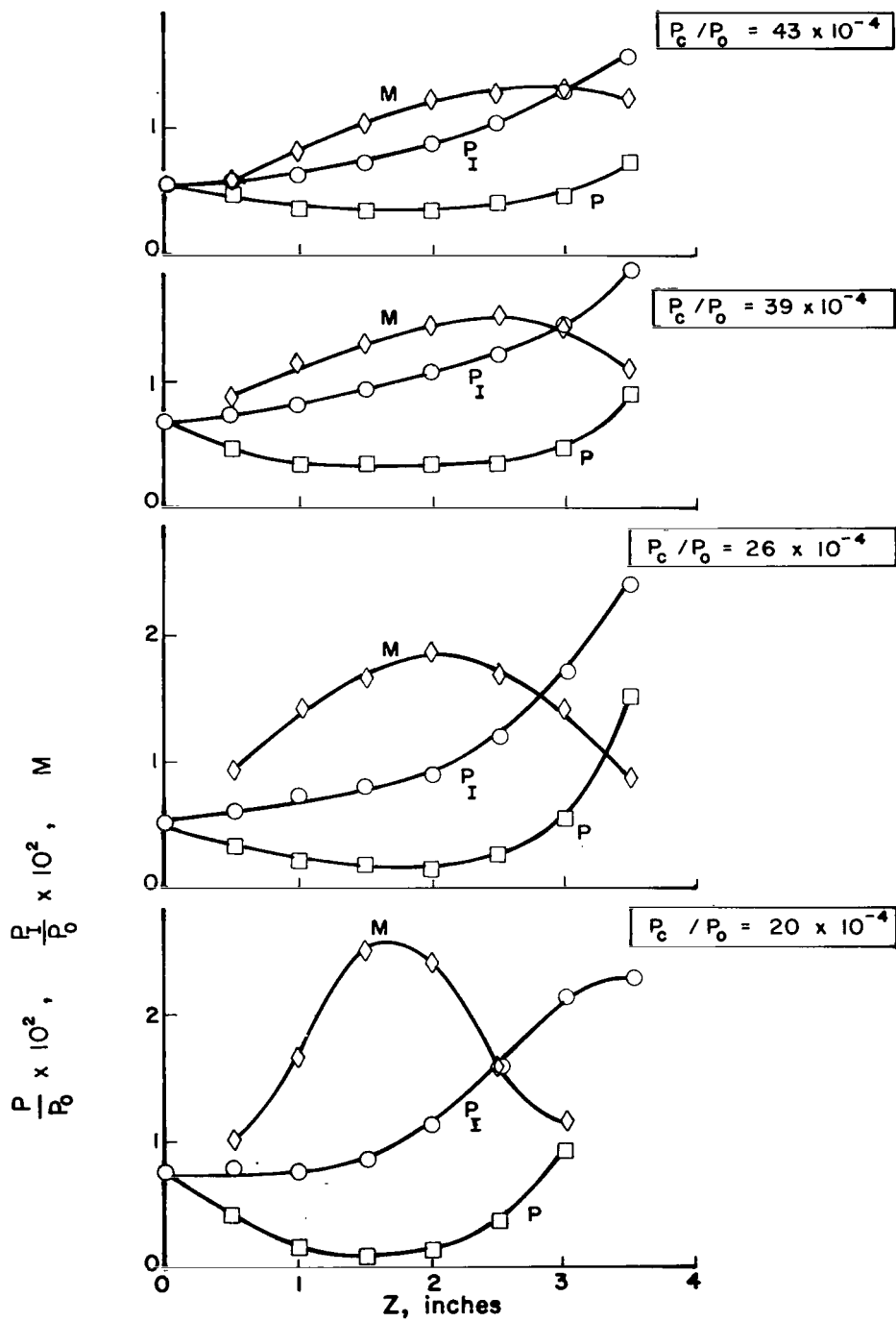
FIGURE 30. VARIATIONS ALONG MODEL CENTERLINE
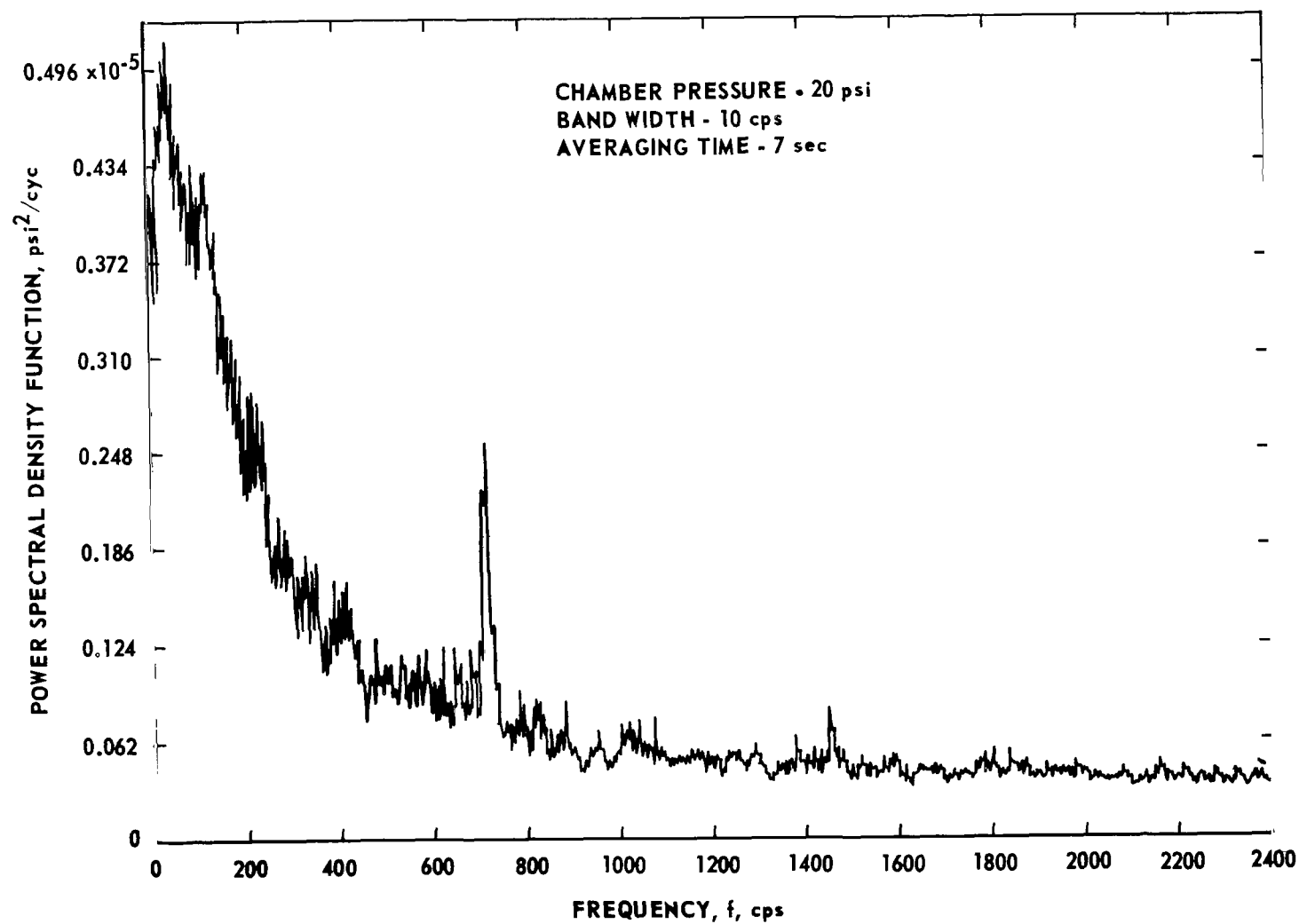
FIGURE 31. SPECTRUM OF CONDENSER MICROPHONE OUTPUT LOCATED ON
CENTER OF HEAT SHIELD

CHAMBER PRESSURE - 20 psi
BAND WIDTH - 50 cps
AVERAGING TIME - 5 sec
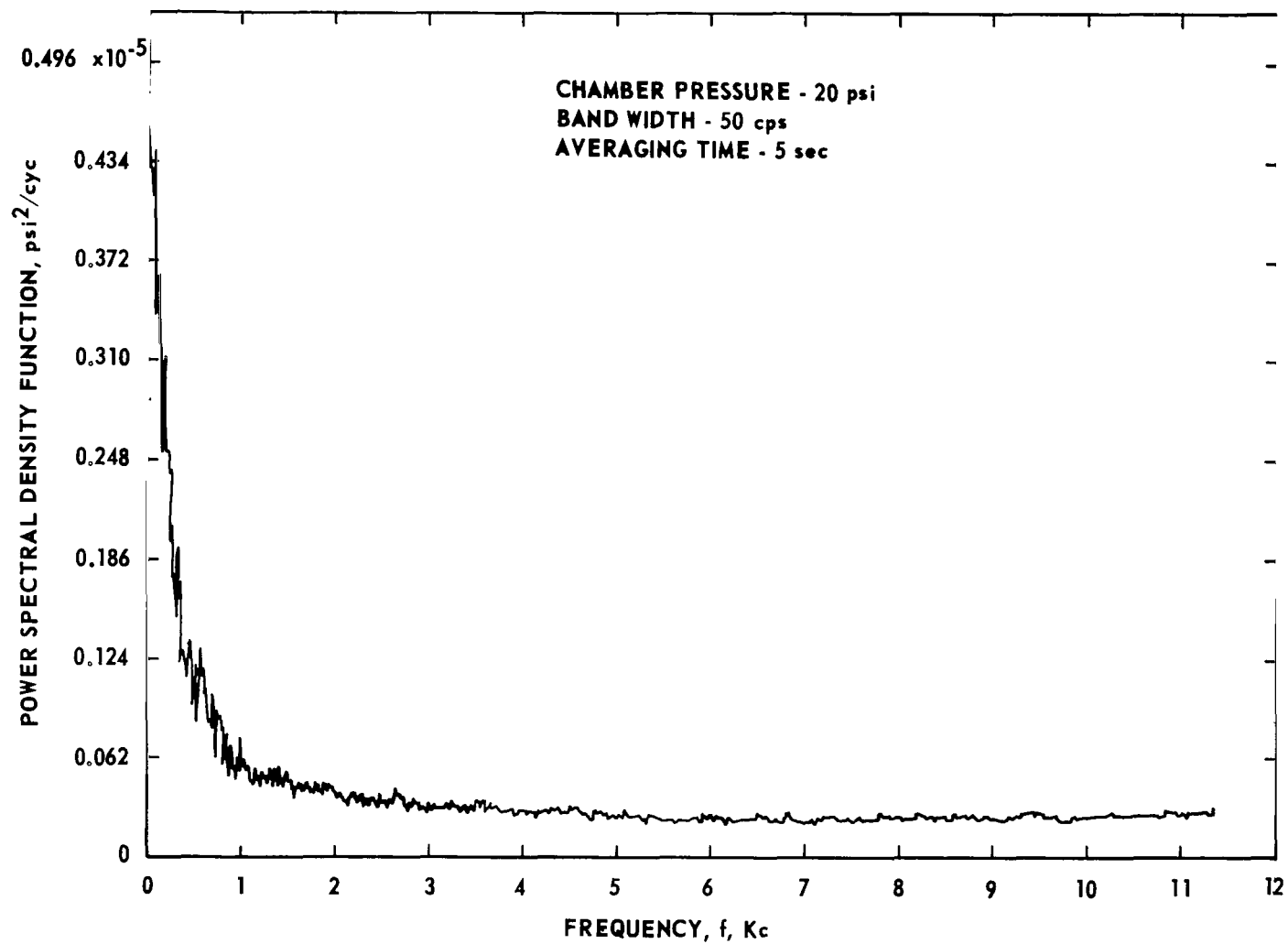
FIGURE 32. SPECTRUM OF CONDENSER MICROPHONE OUTPUT LOCATED ON
CENTER OF HEAT SHIELD
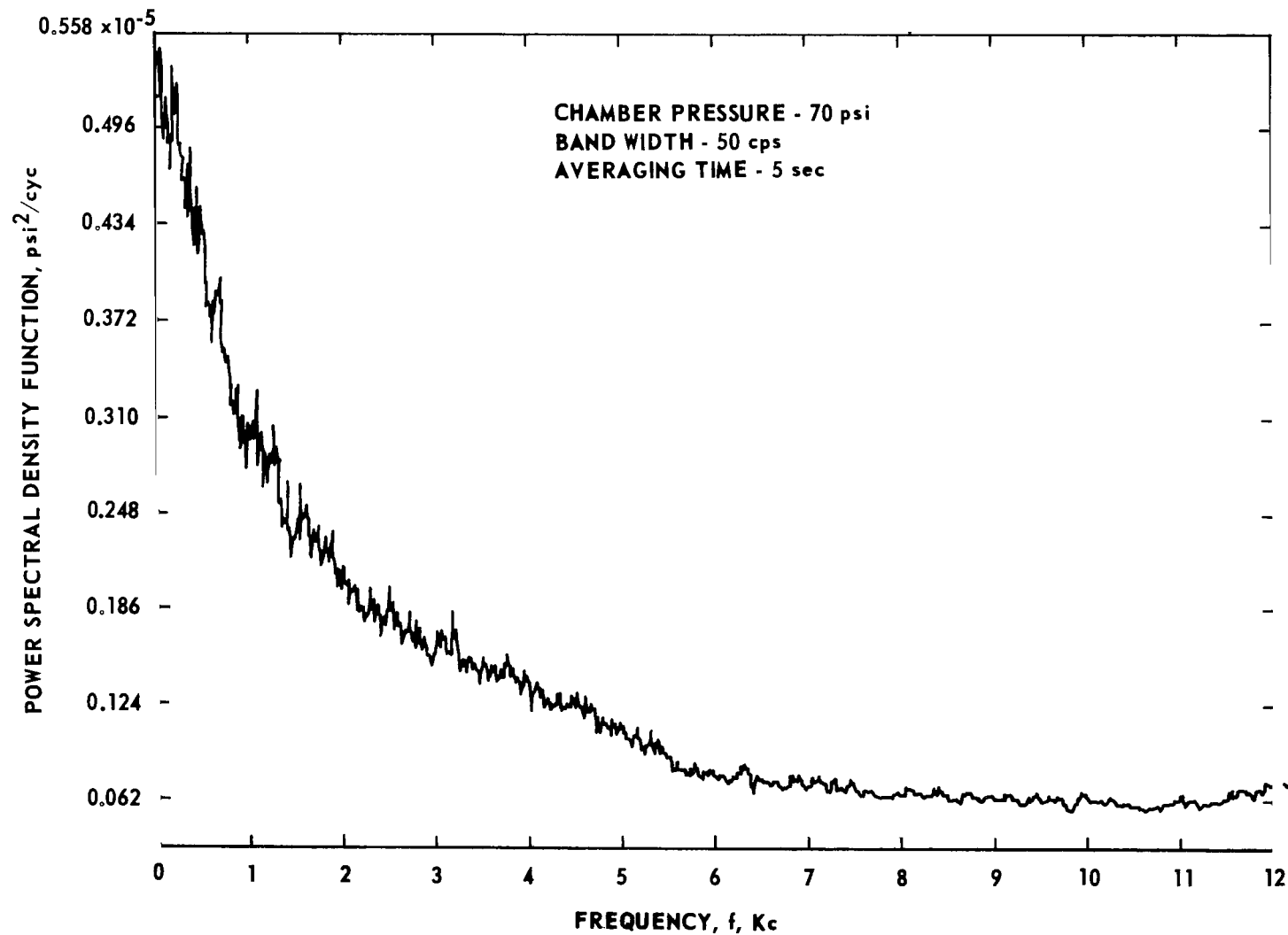
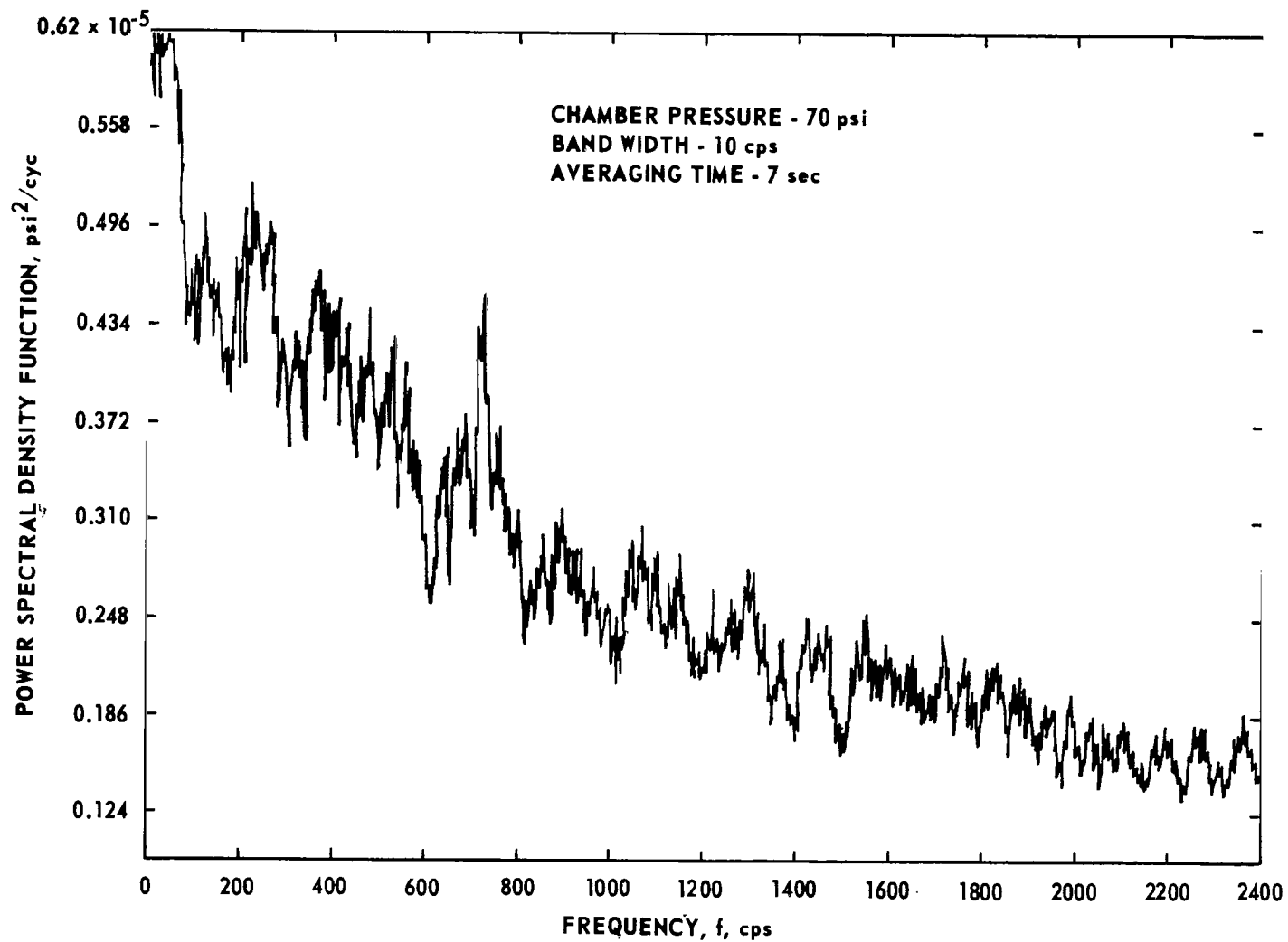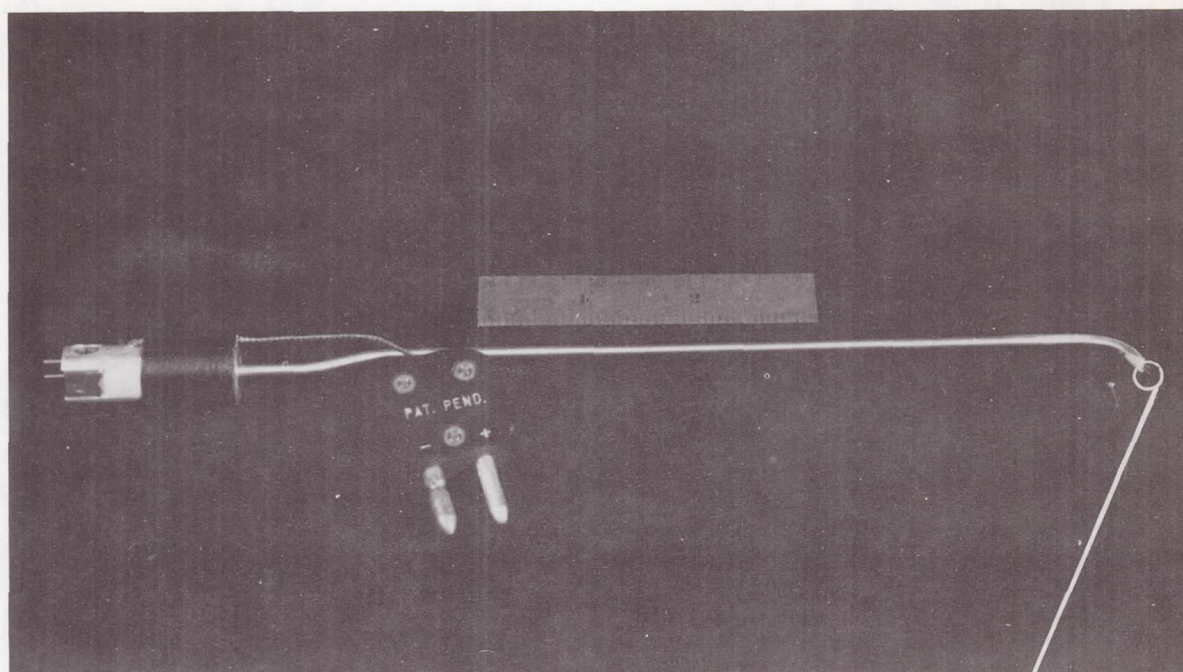FIGURE 33. SPECTRUM OF CONDENSER MICROPHONE OUTPUT LOCATED ON CENTER OF HEAT SHIELD

FIGURE 34.   SPECTRUM OF CONDENSER MICROPHONE OUTPUT LOCATED ON
CENTER OF HEAT SHIELD
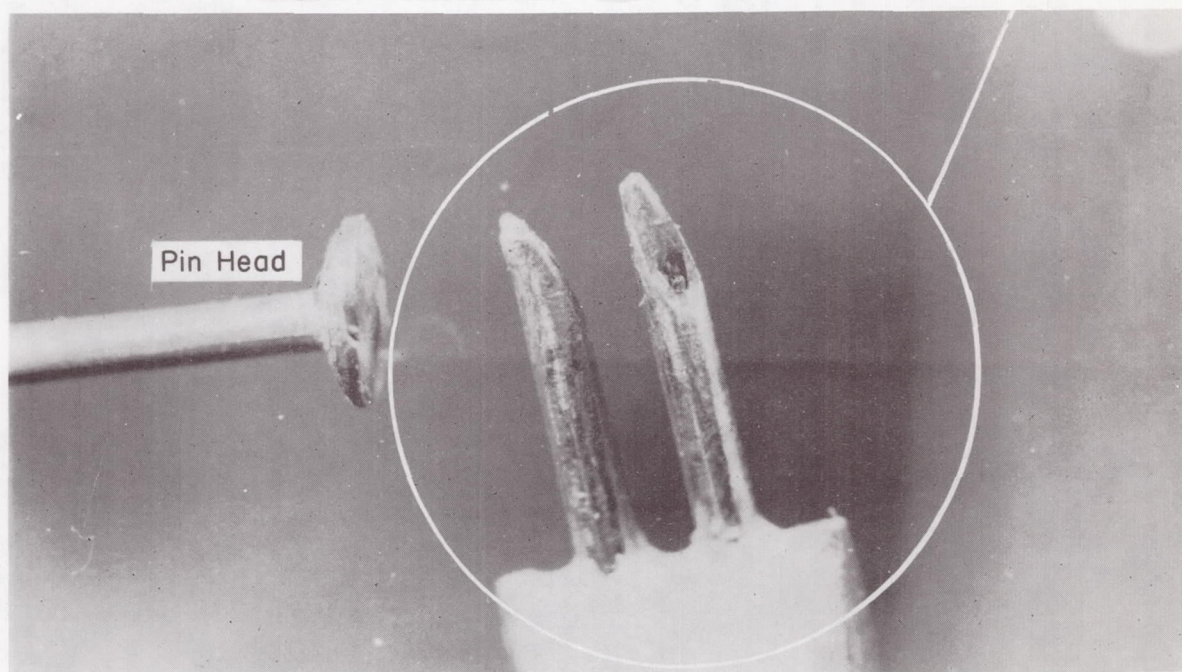
Magnification of Probe Tip is Approximately 19

Pin Head

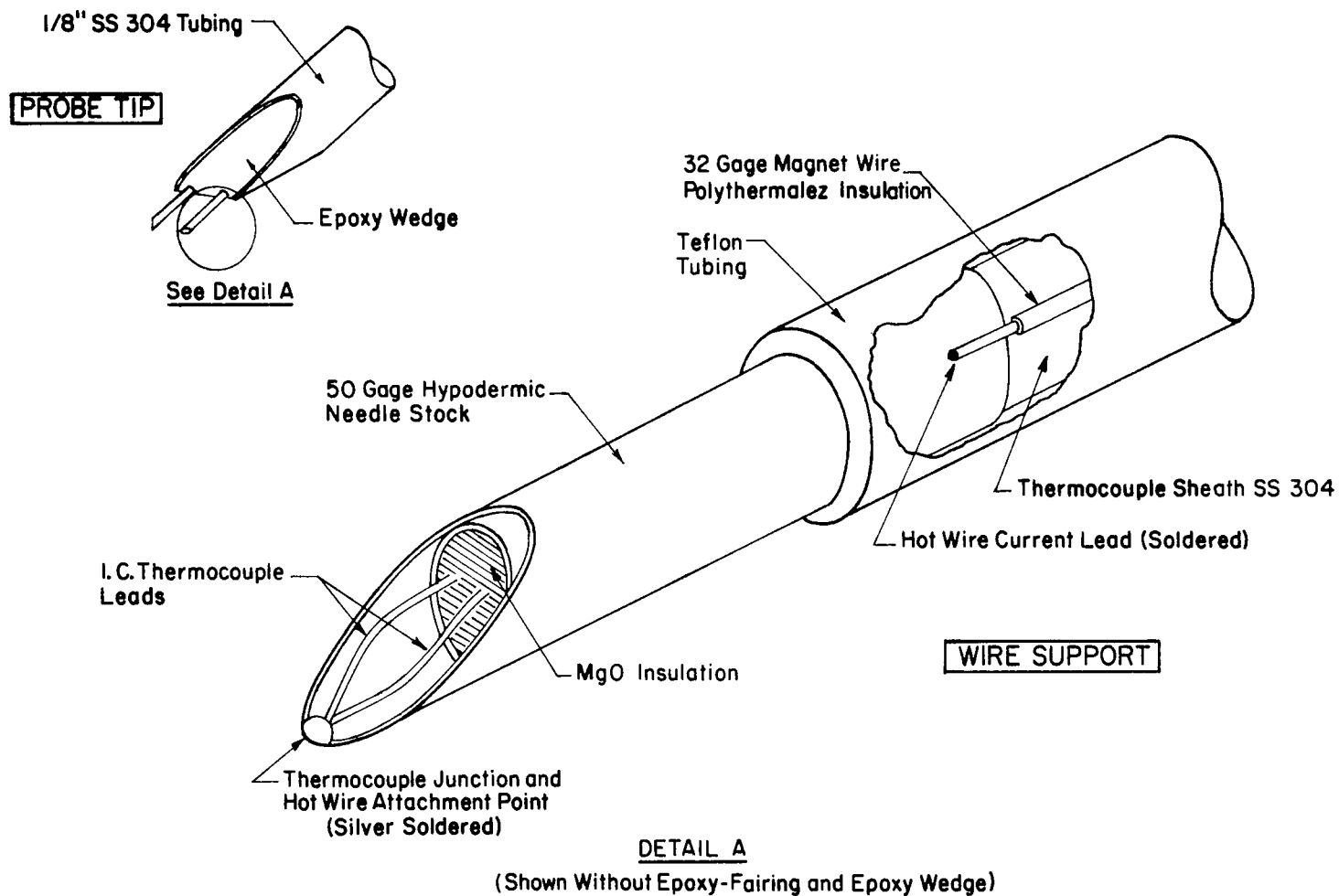FIGURE 35.   PHOTOGRAPHS OF HOT WIRE PROBE

1/8" SS 304 Tubing

PROBE TIP

Epoxy Wedge

See Detail A

32 Gage Magnet Wire
Polythermalez Insulation

Teflon
Tubing

50 Gage Hypodermic
Needle Stock

Thermocouple Sheath SS 304

Hot Wire Current Lead (Soldered)

I. C. Thermocouple
Leads

WIRE SUPPORT

MgO Insulation

Thermocouple Junction and
Hot Wire Attachment Point
(Silver Soldered)

DETAIL A

(Shown Without Epoxy-Fairing and Epoxy Wedge)

FIGURE 36.   SCHEMATIC OF HOT WIRE PROBE
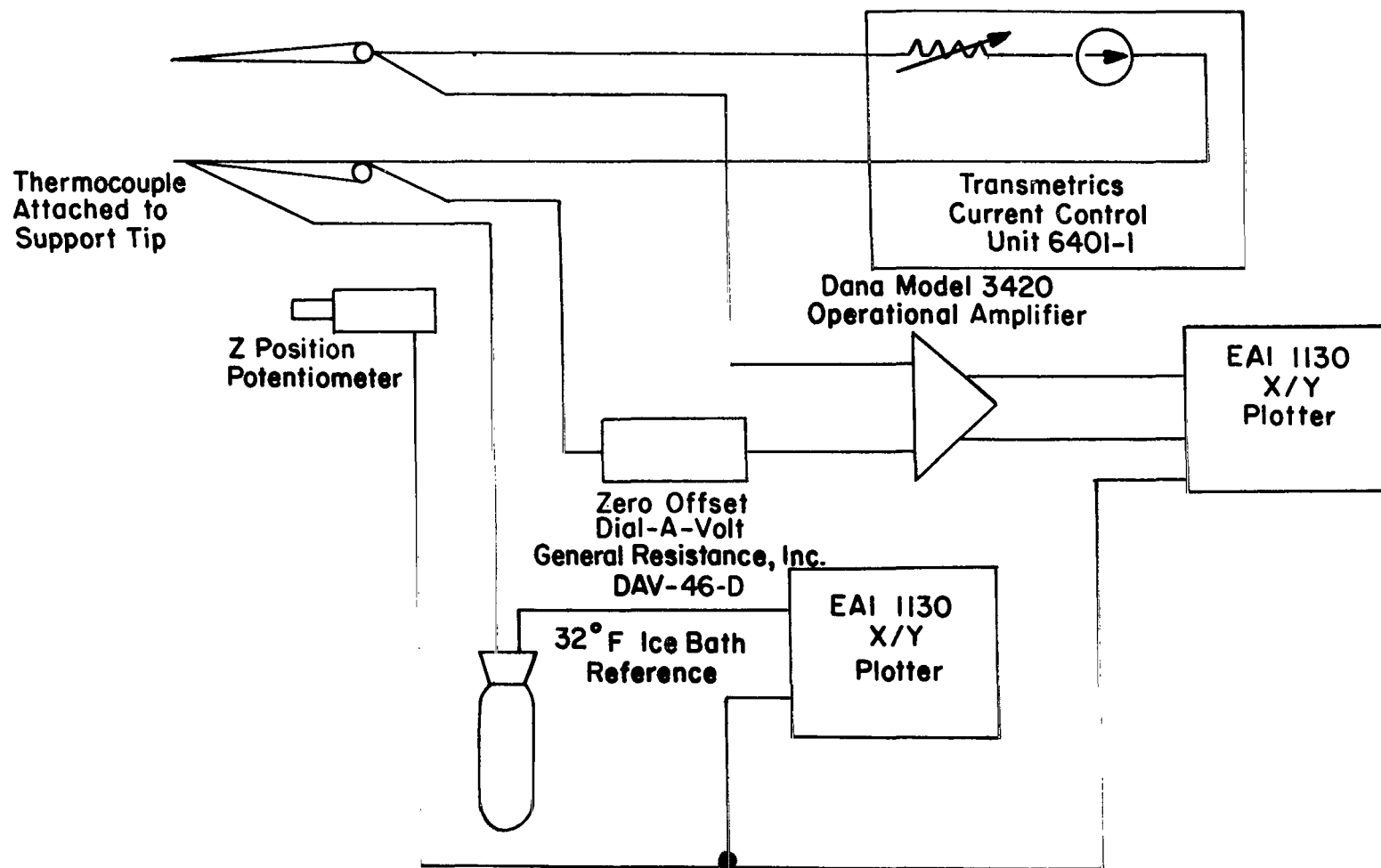
FIGURE 37. SCHEMATIC OF ANEMOMETER AND RECORDING SYSTEM
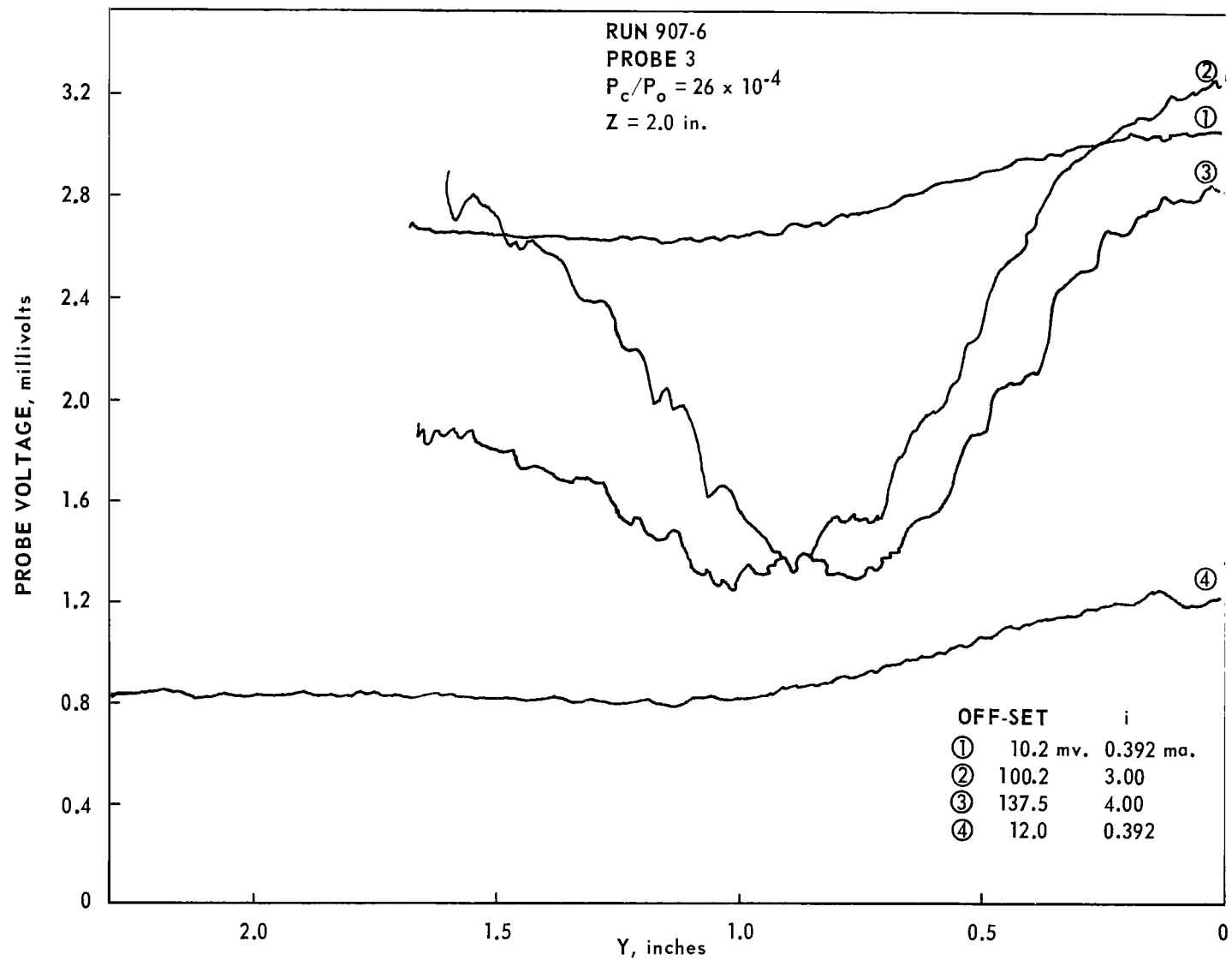
FIGURE 38. HOT WIRE DATA FROM PLOTTER
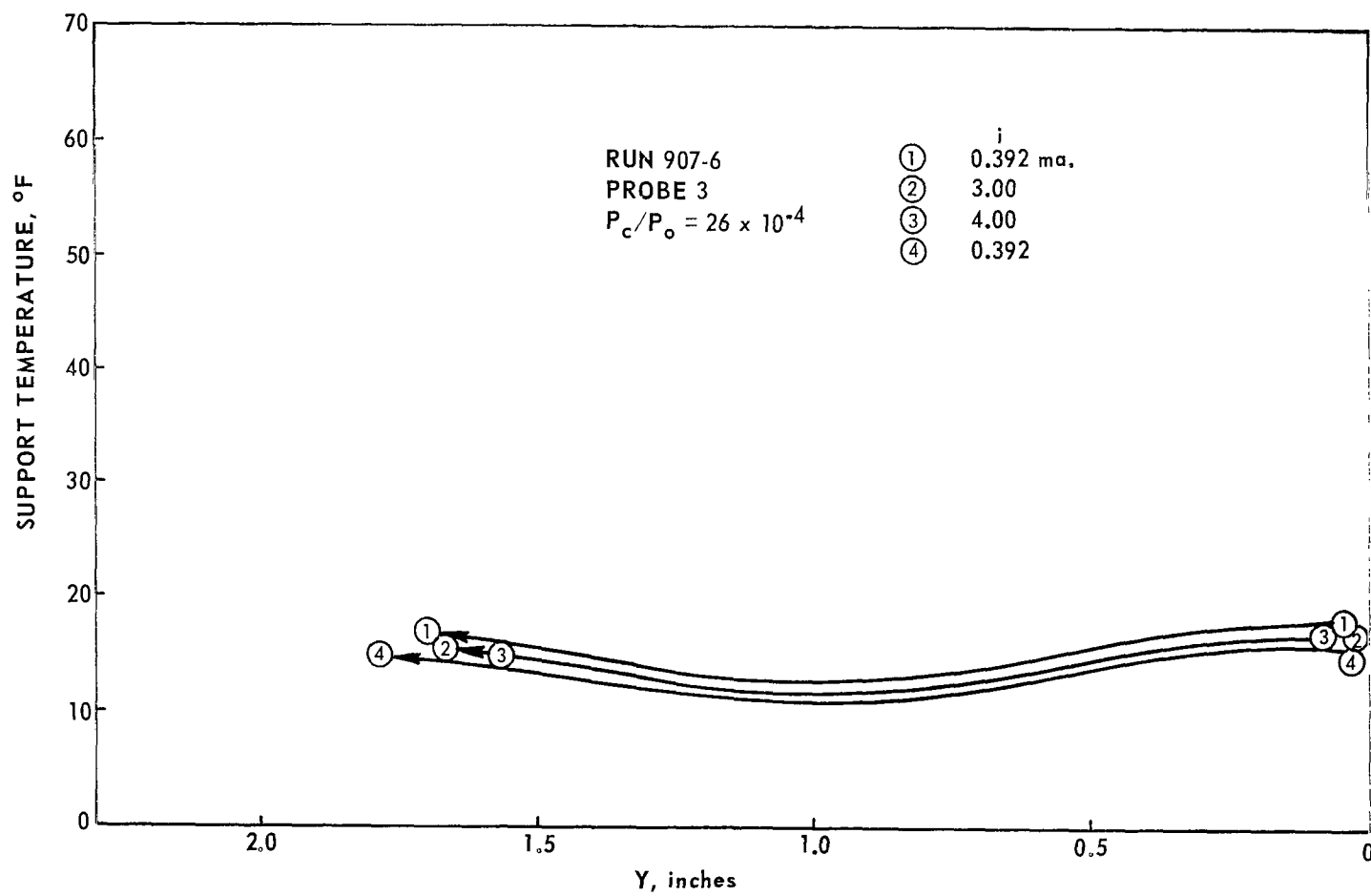
Chart annotations:

RUN 907-6
PROBE 3
$P_c/P_o = 26 \times 10^{-4}$
Z = 2.0 in.

Y-axis: PROBE VOLTAGE, millivolts

X-axis: Y, inches

OFF-SET		i	
①	10.2 mv.	0.392 ma.
②	100.2	3.00
③	137.5	4.00
④	12.0	0.392

FIGURE 39. SUPPORT TEMPERATURE DATA FROM PLOTTER

AEDC(ARO,INC.)ARNOLD AFS, TENNESSEE
VON KARMAN GAS DYNAMICS FACILITY
GAS DYNAMIC WIND TUNNEL,SUPERSONIC(E)

PAGE NO. ONE
RUN   GROUP
V07   6   0   0   0

PO	TO	0	0	0	REF1	REF2	REF3
6.920E 01	5.0700E 02	6.0197E 01	0	0	2.2793E-03	0	-9.2080E-03

PC				TC	TNW		
	0	0	0	5.3500E 02	4.7700E 02	5.4300E 02	4.6000E 02
1.545E-01	2.375E-01	1.246E-01	2.083E-01	1.533E-01	2.925E-01	P	
2.557E-03	3.944E-03	3.265E-03	3.461E-03	2.541E-03	4.461E-03	P/PO	
1.000E 00	1.537E 00	1.144E 00	1.348E 00	9.900E-01	1.693E 00	P/P	

TRACE ① (FIGURE 38)

5.153E 01	5.0700E 02	6.1574E 01	0	0	2.6349E-03	0	-9.2080E-03
	0	0	0	5.3500E 02	4.7600E 02	5.4300E 02	4.6000E 02
1.538E-01	3.047E-01	2.033E-01	2.525E-01	1.512E-01	3.323E-01	P	
2.497E-03	4.947E-03	3.301E-03	4.099E-03	2.455E-03	5.395E-03	P/PO	
1.000E 00	1.931E 00	1.322E 00	1.641E 00	9.830E-01	2.161E 00	P/P	

6.094E-01	5.0550E-02	6.0942E-01	0	0	3.2562E-03	9.3730E-03	-9.2080E-03
	0	0	9.3980E-03	5.3450E 02	4.7500E 02	5.4300E 02	4.6000E 02
1.576E-01	2.441E-01	1.887E-01	2.135E-01	1.557E-01	2.977E-01	P	
2.546E-03	4.005E-03	3.095E-03	3.503E-03	2.555E-03	4.855E-03	P/PO	
1.000E 00	1.549E 00	1.197E 00	1.355E 00	9.861E-01	1.889E 00	P/P	

TRACE ②

6.065E 01	5.0550E 02	6.0562E 01	0	0	3.2562E-03	9.3730E-03	-9.2080E-03
	0	0	9.3980E-03	5.345E 02	4.7600E 02	5.4300E 02	4.6000E 02
1.566E-01	2.984E-01	2.033E-01	2.514E-01	1.545E-01	3.315E-01	P	
2.531E-03	4.919E-03	3.351E-03	4.144E-03	2.533E-03	5.465E-03	P/PO	
1.000E 00	1.906E 00	1.298E 00	1.606E 00	9.934E-01	2.117E 00	P/P	

6.040E 01	5.0600E 02	6.0475E 01	0	0	3.9374E-03	1.4397E-02	-9.2080E-03
	0	0	1.4097E-02	5.3450E 02	4.7500E 02	5.4300E 02	4.6000E 02
1.569E-01	2.524E-01	1.907E-01	2.200E-01	1.536E-01	2.991E-01	P	
2.534E-03	4.174E-03	3.154E-03	3.533E-03	2.539E-03	4.945E-03	P/PO	
1.000E 00	1.609E 00	1.215E 00	1.403E 00	9.790E-01	1.937E 00	P/P	

TRACE ③

6.040E 01	5.0600E 02	6.0475E 01	0	0	4.5535E-03	1.8796E-02	0
	0	0	1.8796E-02	5.345E 02	4.7500E 02	5.4300E 02	4.6000E 02
1.572E-01	3.032E-01	2.032E-01	2.520E-01	1.542E-01	3.315E-01	P	
2.539E-03	5.013E-03	3.300E-03	4.167E-03	2.550E-03	5.432E-03	P/PO	
1.000E 00	1.929E 00	1.293E 00	1.604E 00	9.912E-01	2.105E 00	P/P	

6.094E-01	5.0600E-02	6.0942E 01	0	0	2.9335E-03	1.4397E-02	-9.2080E-03
	0	0	1.4097E-02	5.345E 02	4.7500E 02	5.4300E 02	4.6000E 02
1.566E-01	2.389E-01	1.873E-01	2.184E-01	1.554E-01	2.955E-01	P	
2.559E-03	3.920E-03	3.074E-03	3.452E-03	2.550E-03	4.767E-03	P/PO	
1.000E 00	1.526E 00	1.196E 00	1.344E 00	9.924E-01	1.855E 00	P/P	

TRACE ④

6.040E 01	5.0600E 02	6.0475E 01	0	0	3.9374E-03	1.4397E-02	-9.2080E-03
	0	0	1.4097E-02	5.3400E 02	4.7500E 02	5.4300E 02	4.6000E 02
1.555E-01	3.018E-01	2.022E-01	2.503E-01	1.536E-01	3.322E-01	P	
2.571E-03	4.491E-03	3.343E-03	4.139E-03	2.539E-03	5.467E-03	P/PO	
1.000E 00	1.941E 00	1.309E 00	1.610E 00	9.877E-01	2.124E 00	P/P	

PO = Plenum Pressure   TO = Plenum Temperature   PC = Cell Pressure   TC = Cell Temperature   TNW = Nozzle Lip Temperature

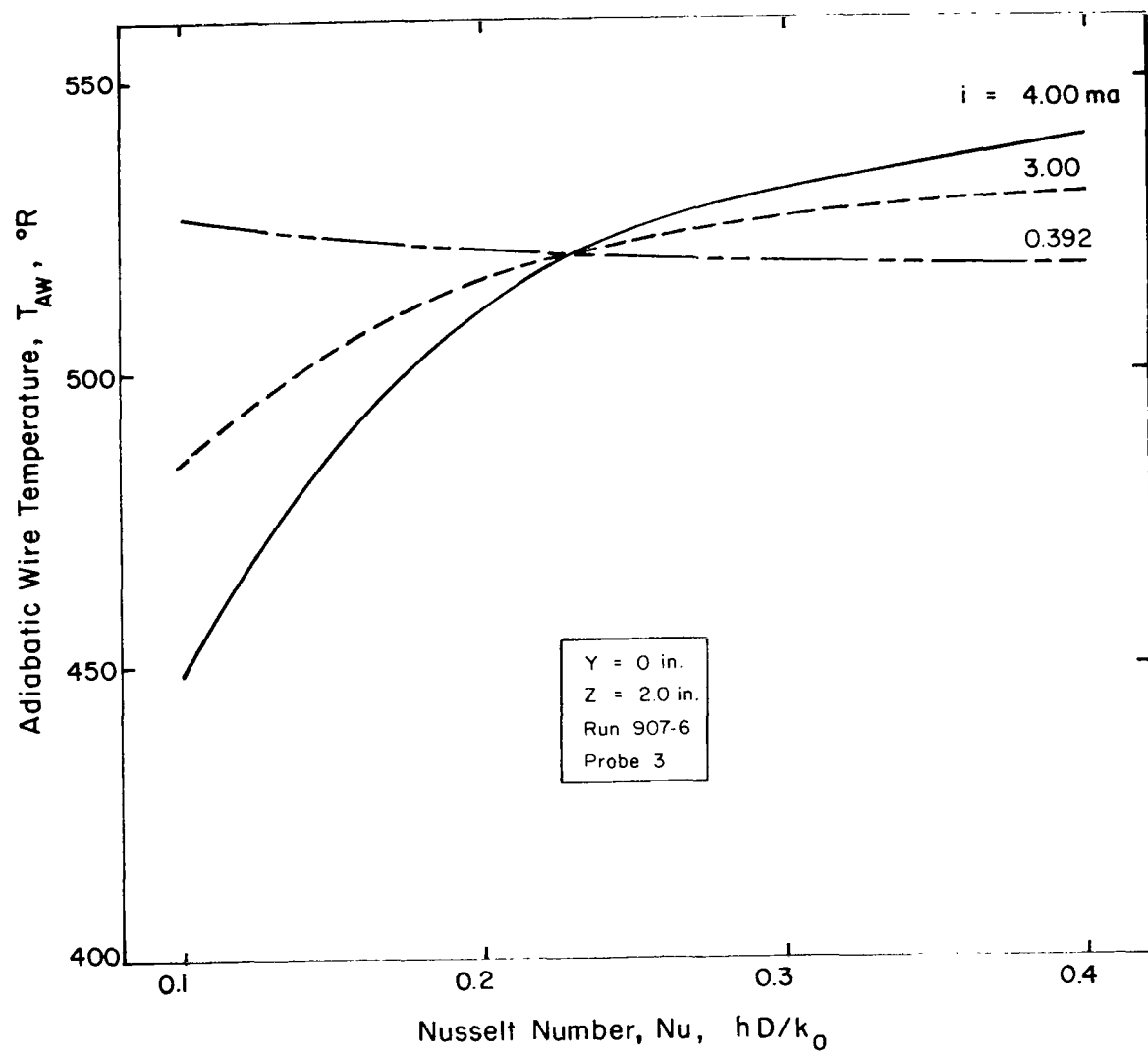FIGURE 40.   EXAMPLE OUTPUT FROM THE VKF DATA SYSTEM
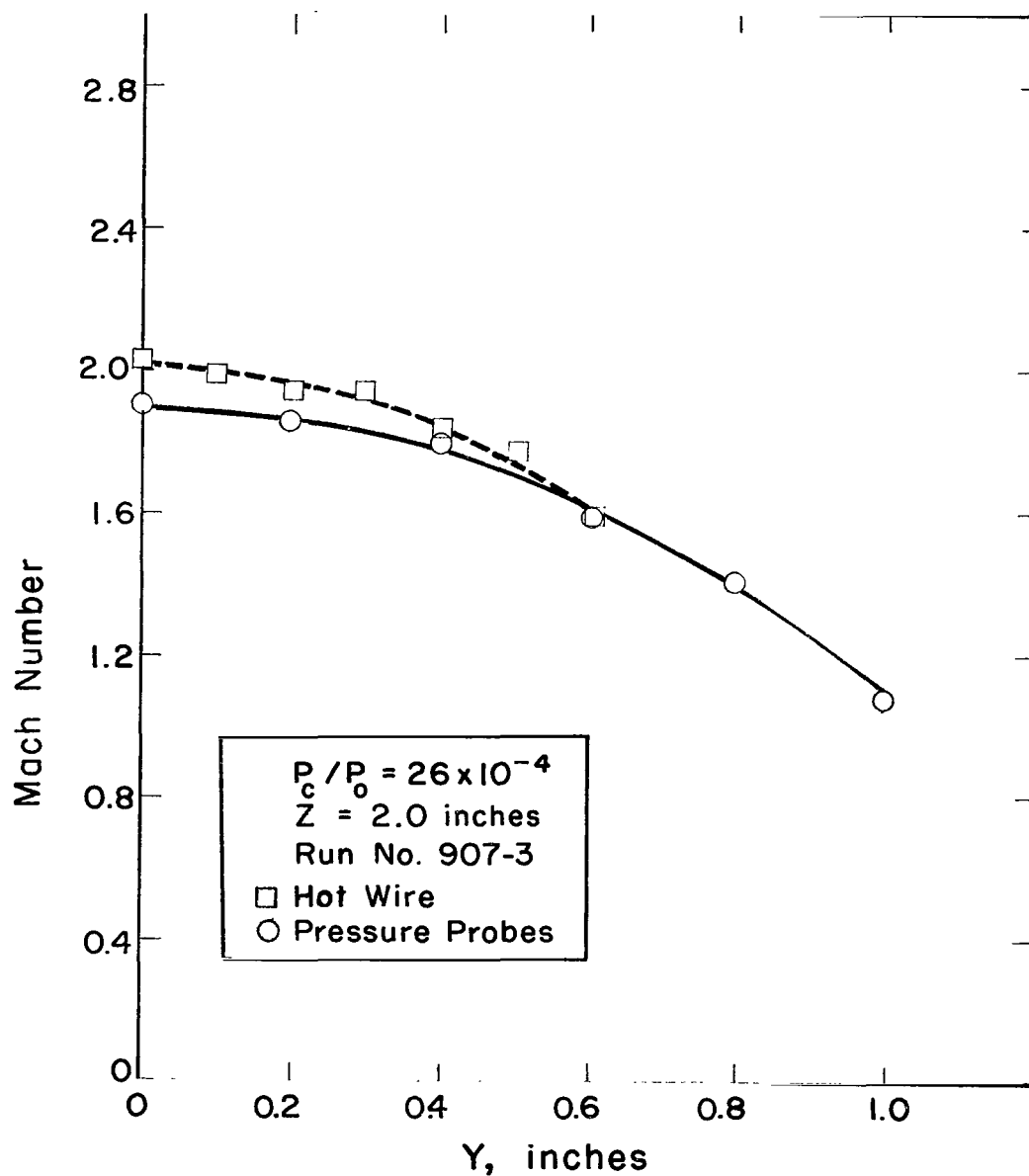
FIGURE 41. FINITE WIRE EQUATION

FIGURE 42.   COMPARISON OF REVERSE JET MACH NUMBER AS OBTAINED
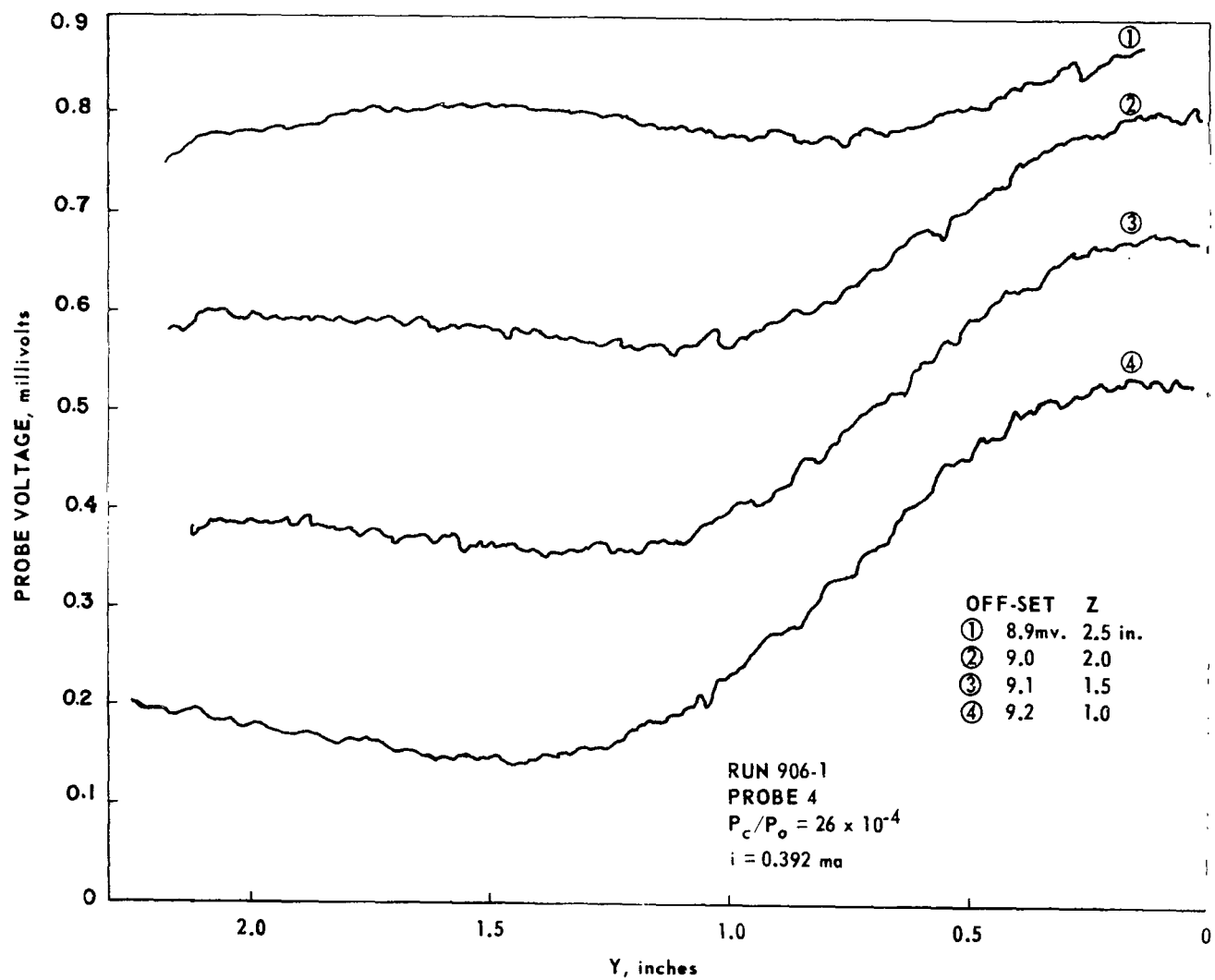FROM HOT WIRE AND PRESSURE INSTRUMENTATION
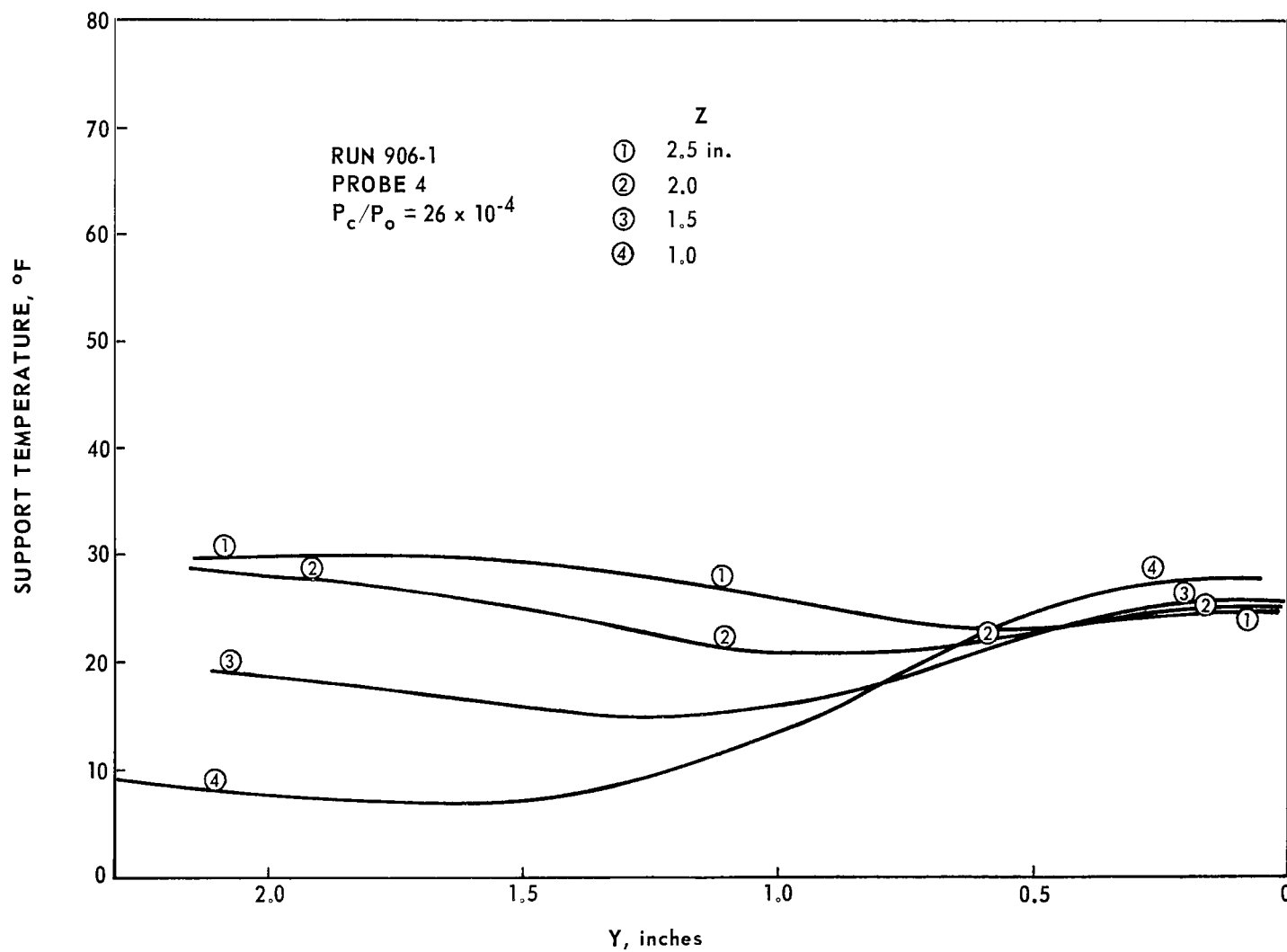
FIGURE 43.   HOT WIRE DATA FROM PLOTTER

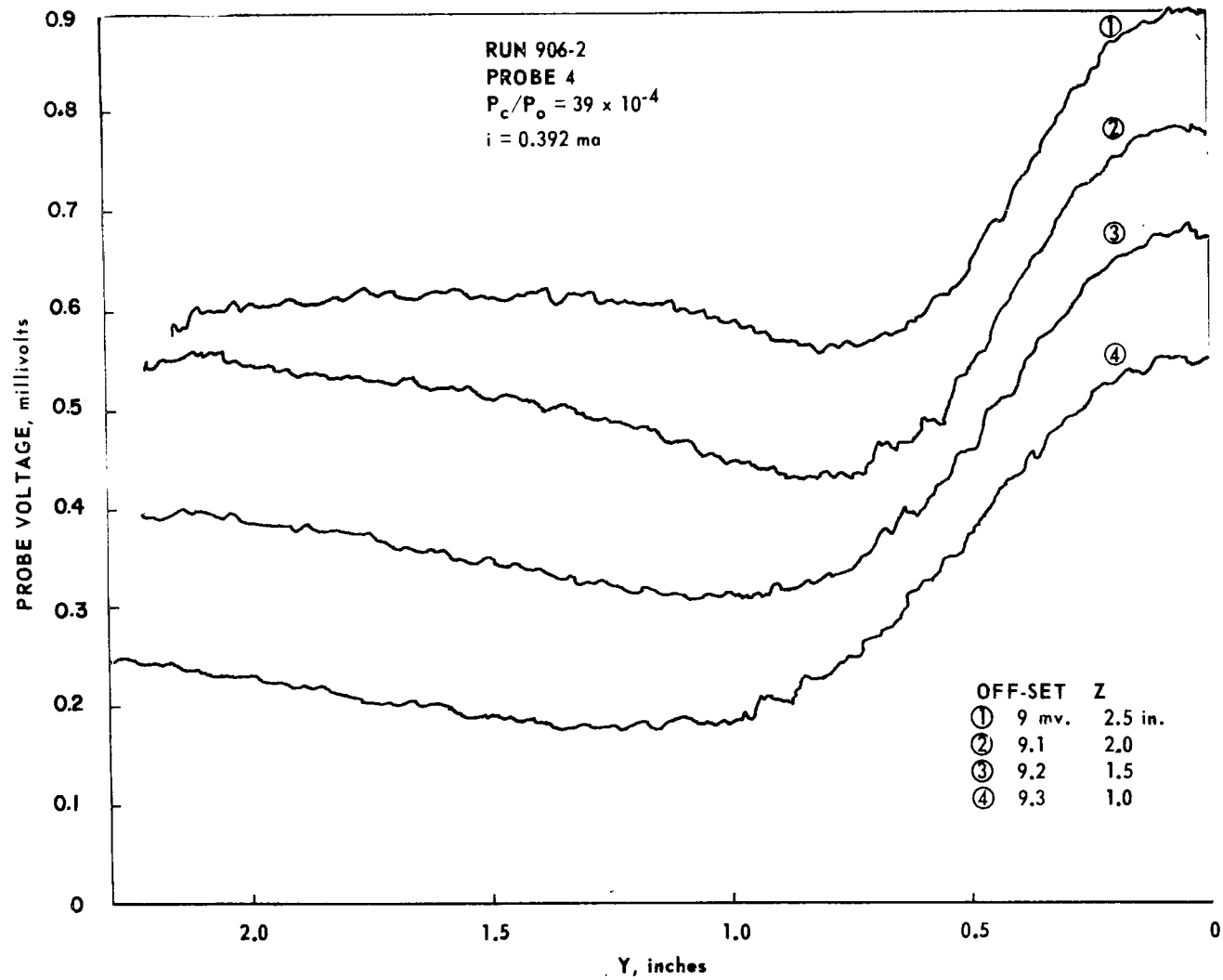FIGURE 44. SUPPORT TEMPERATURE DATA FROM PLOTTER

FIGURE 45. HOT WIRE DATA FROM PLOTTER

RUN 906-2
PROBE 4
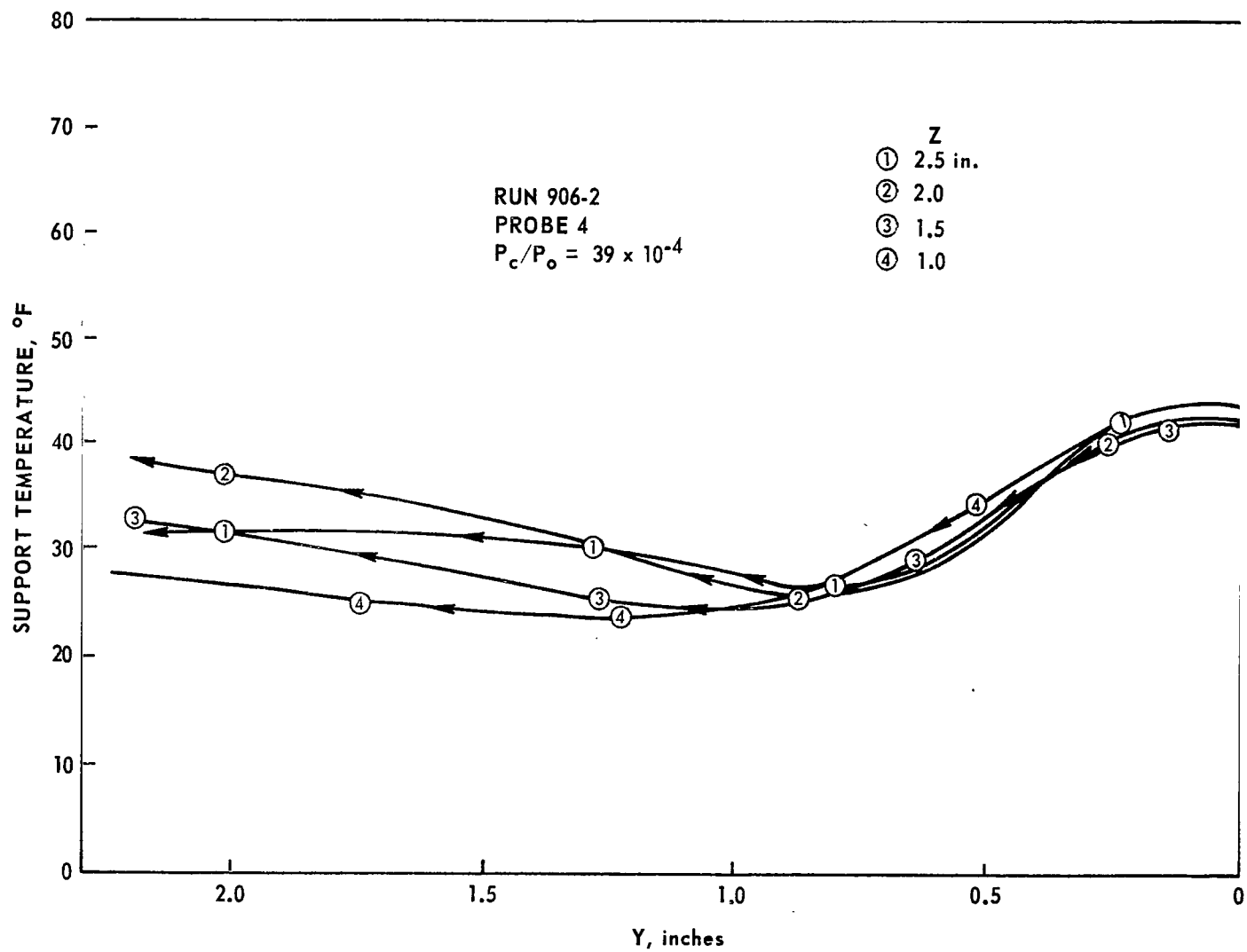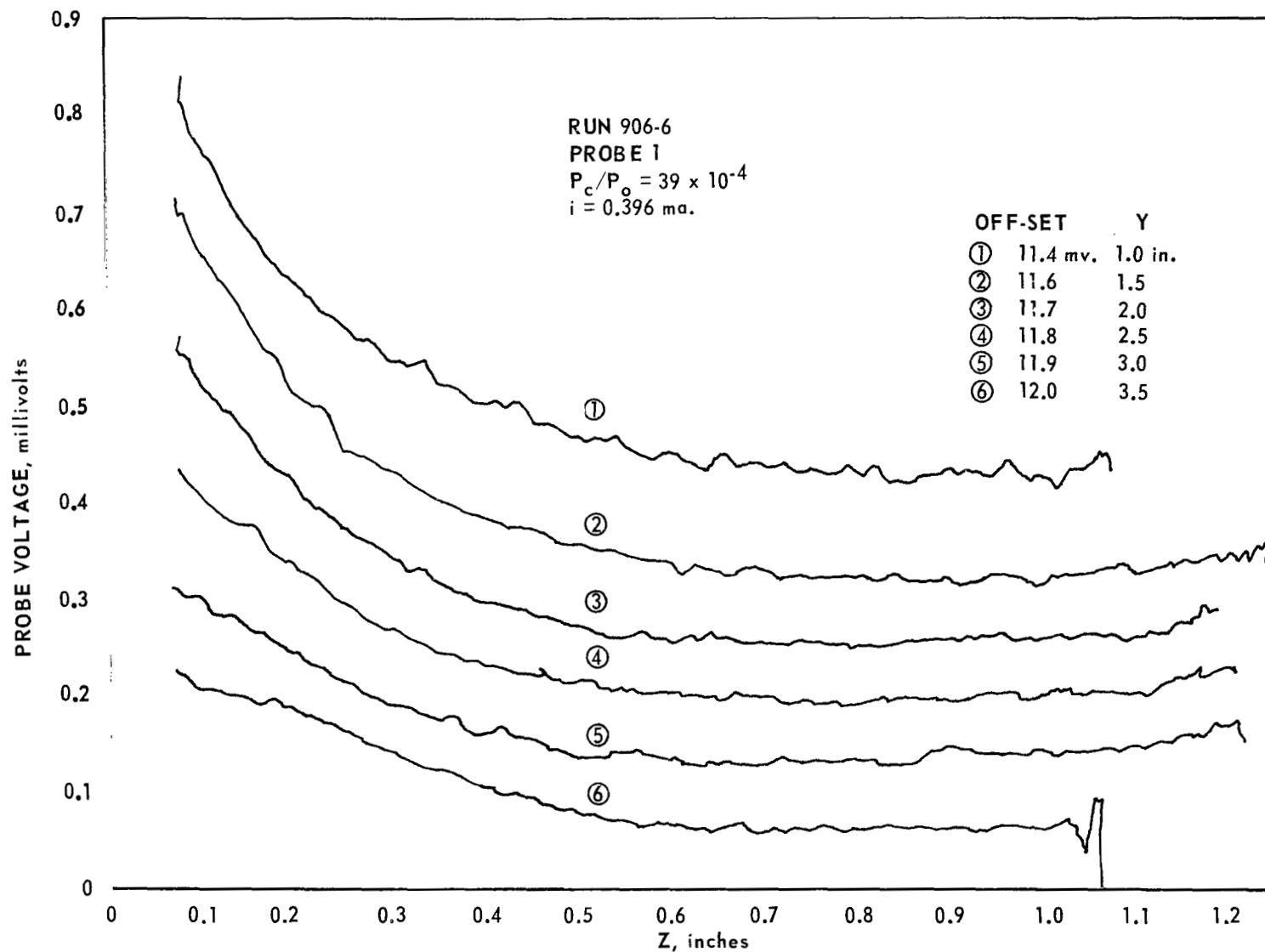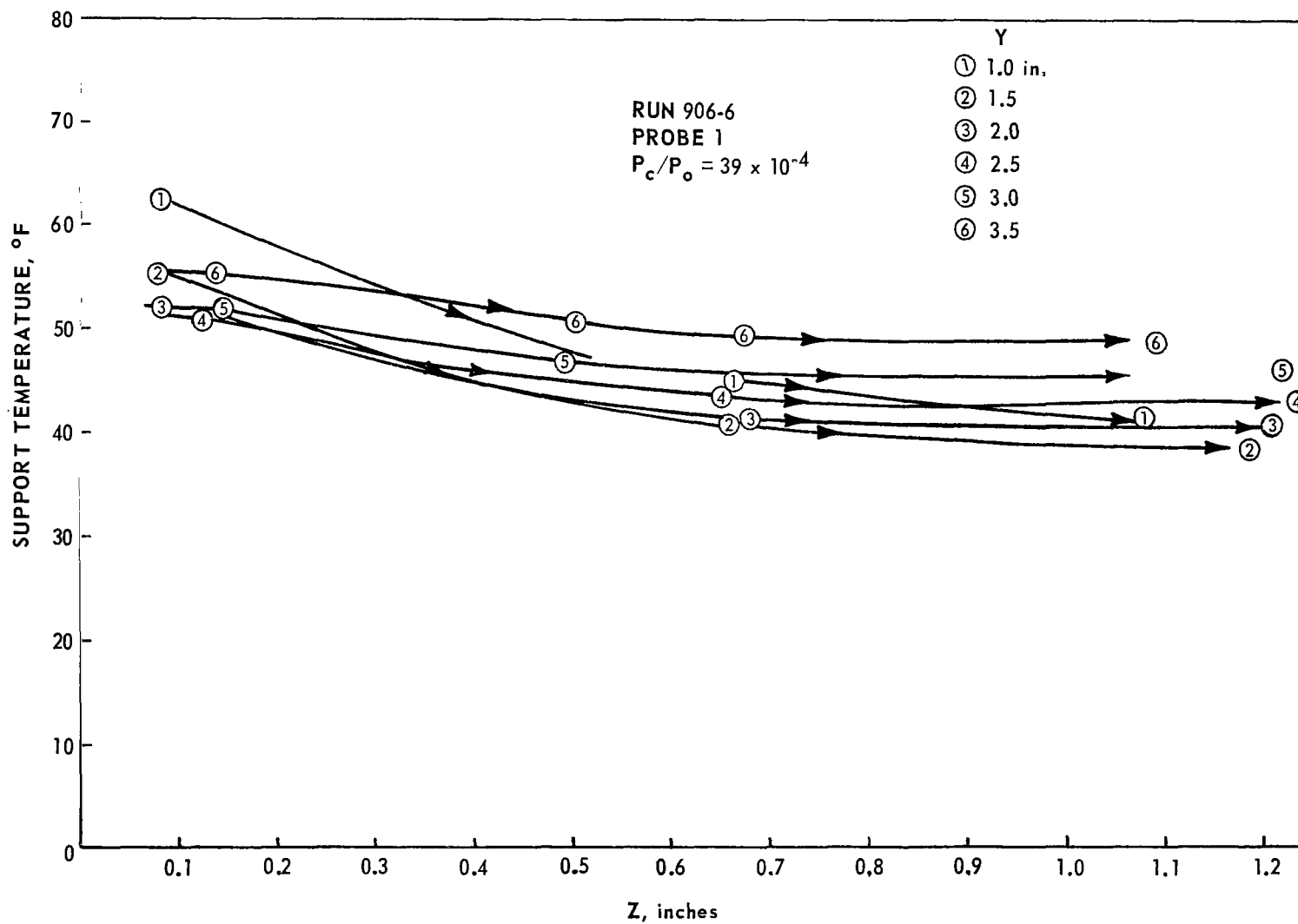$P_c/P_o = 39 \times 10^{-4}$

Z
① 2.5 in.
② 2.0
③ 1.5
④ 1.0

SUPPORT TEMPERATURE, °F

80

70

60

50

40

30

20

10

0

2.0   1.5   1.0   0.5   0

Y, inches

FIGURE 46.   SUPPORT TEMPERATURE DATA FROM PLOTTER

RUN 906-6
PROBE 1
$P_c/P_o = 39 \times 10^{-4}$
$i = 0.396$ ma.

	OFF-SET	Y
①	11.4 mv.	1.0 in.
②	11.6	1.5
③	11.7	2.0
④	11.8	2.5
⑤	11.9	3.0
⑥	12.0	3.5

PROBE VOLTAGE, millivolts

Z, inches

FIGURE 47.   HOT WIRE DATA FROM PLOTTER

FIGURE 48. SUPPORT TEMPERATURE DATA FROM PLOTTER
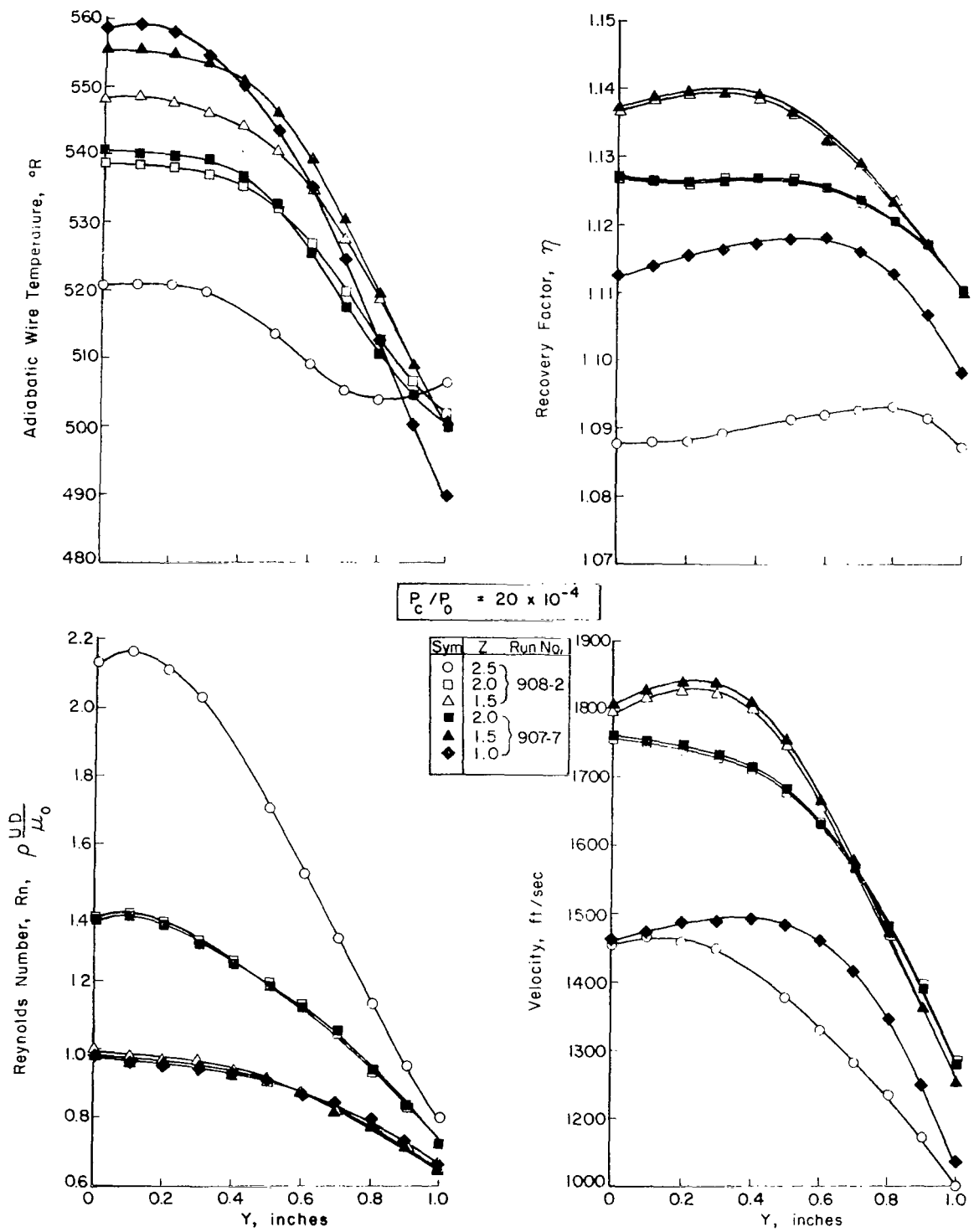
FIGURE 49.   FLOW FIELD PARAMETERS
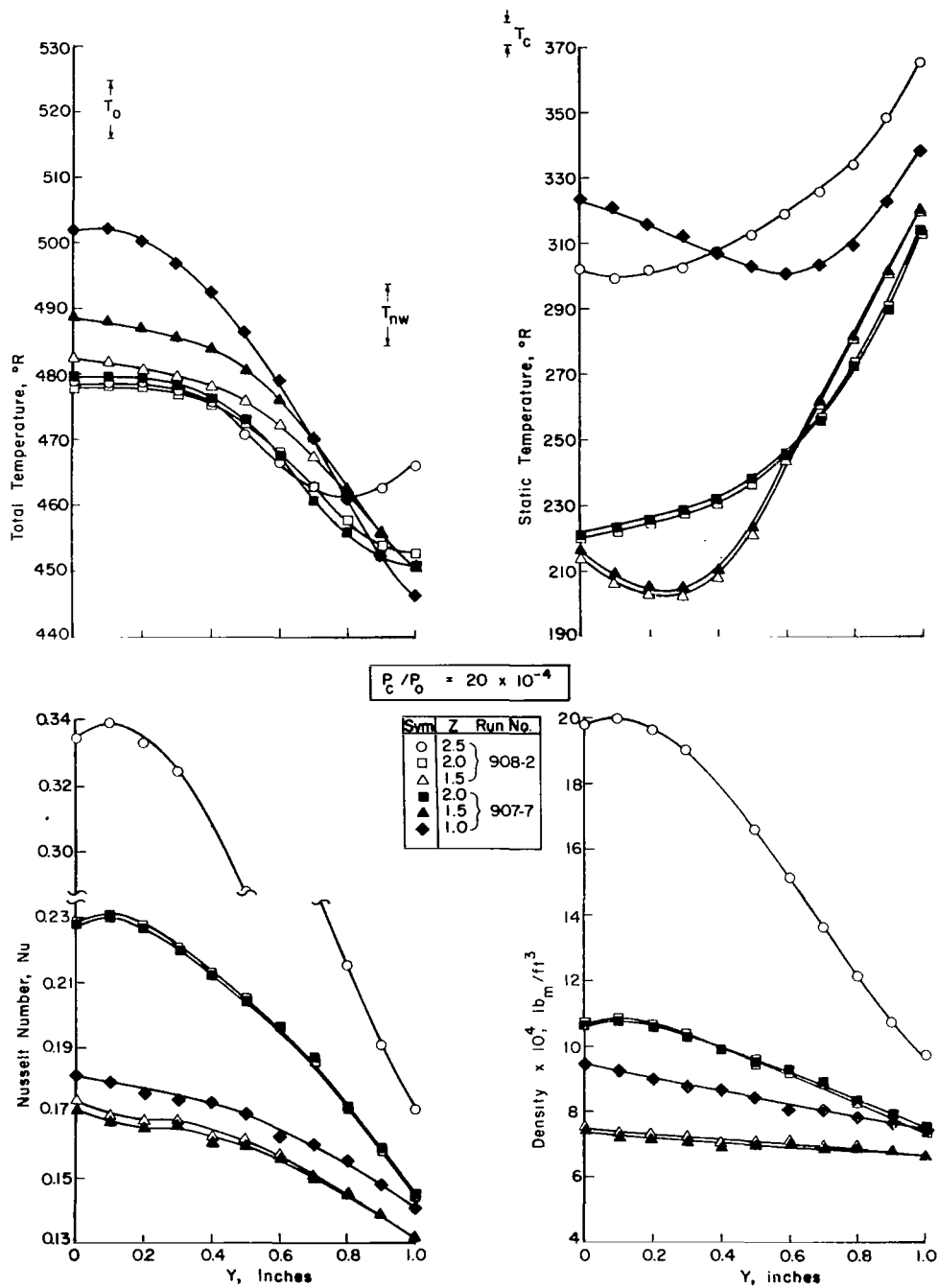
FIGURE 50.   FLOW FIELD PARAMETERS
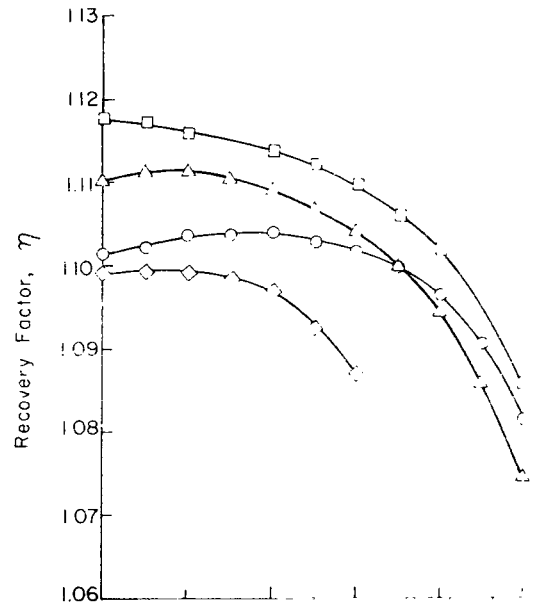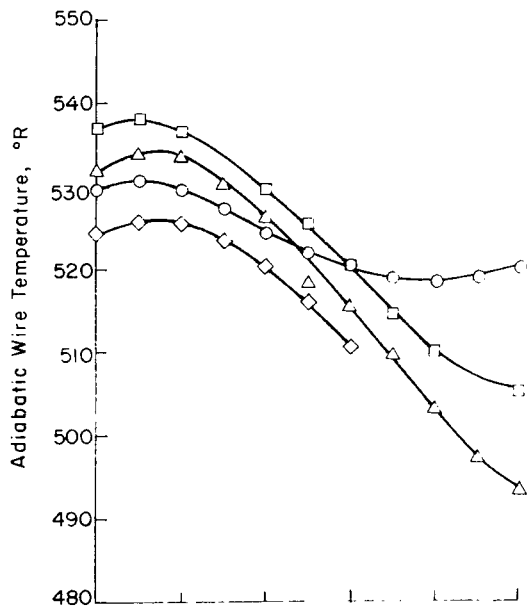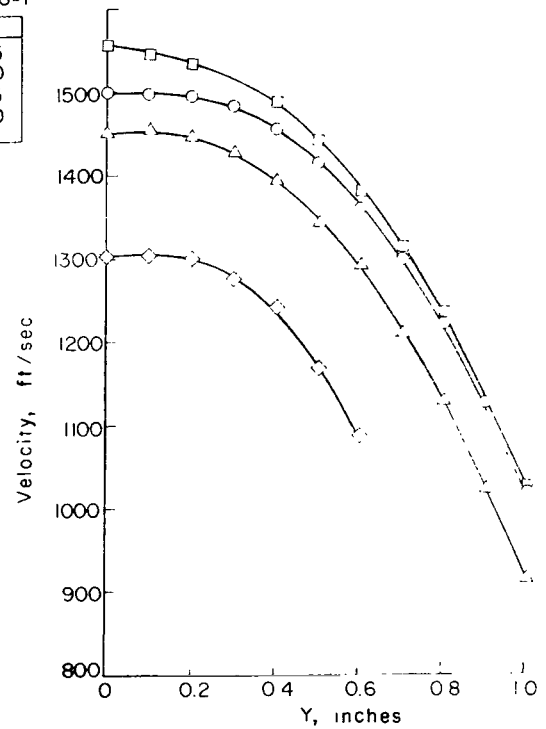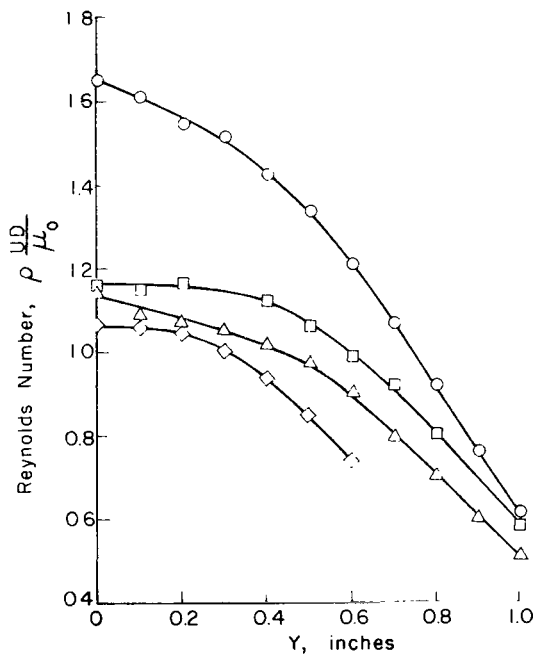
FIGURE 51. FLOW FIELD PARAMETERS
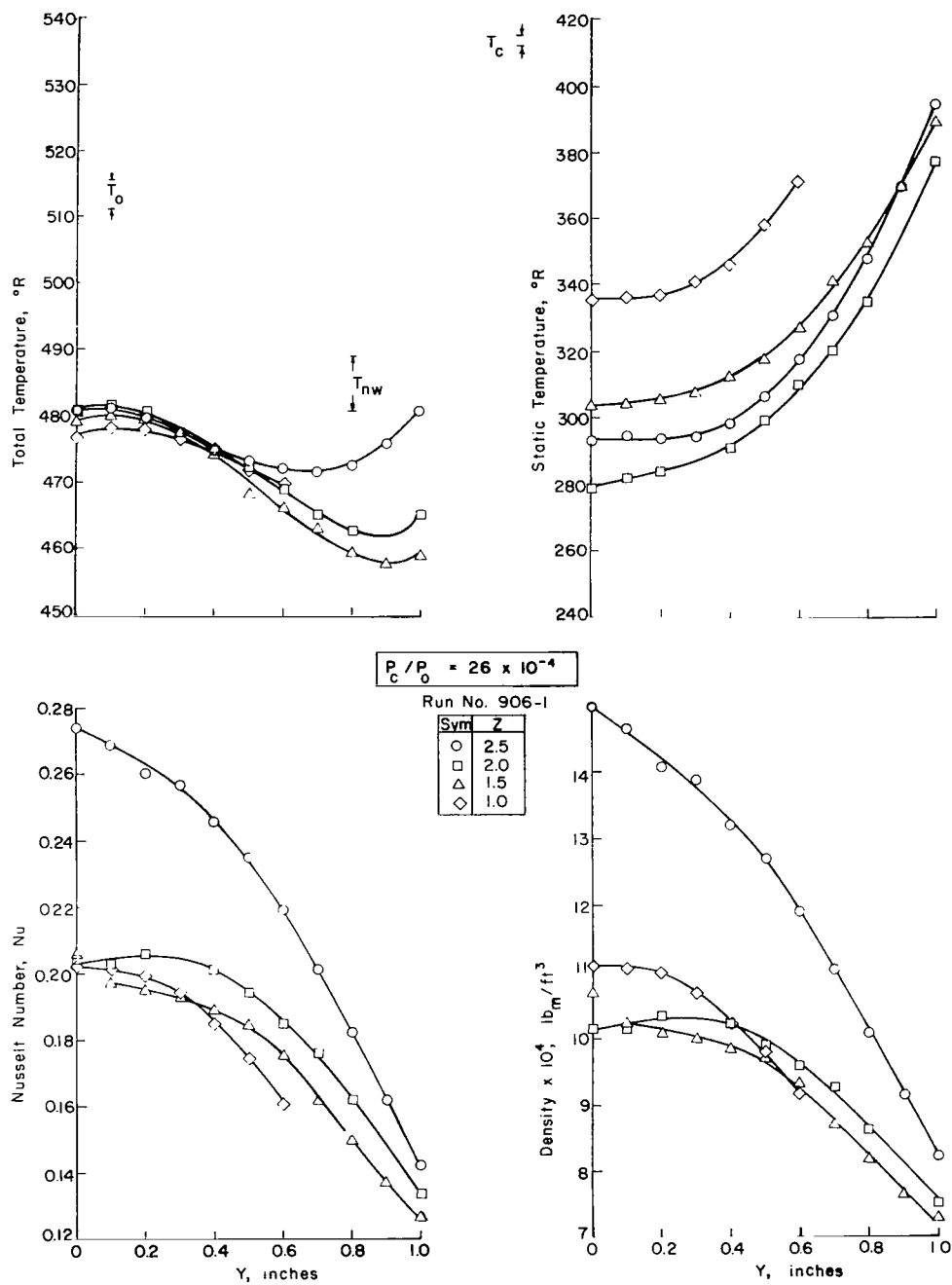
FIGURE 52.   FLOW FIELD PARAMETERS
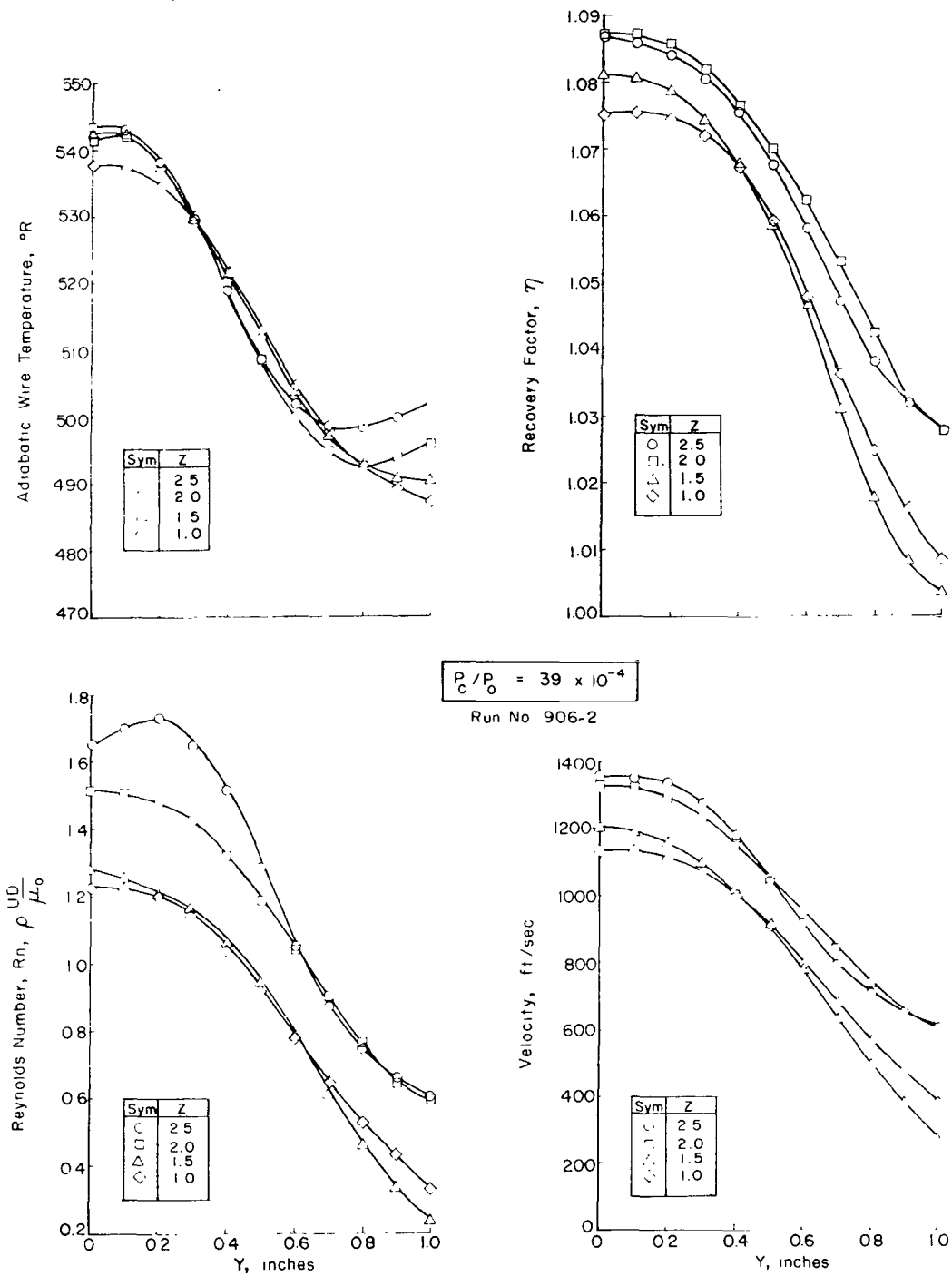
FIGURE 53. FLOW FIELD PARAMETERS
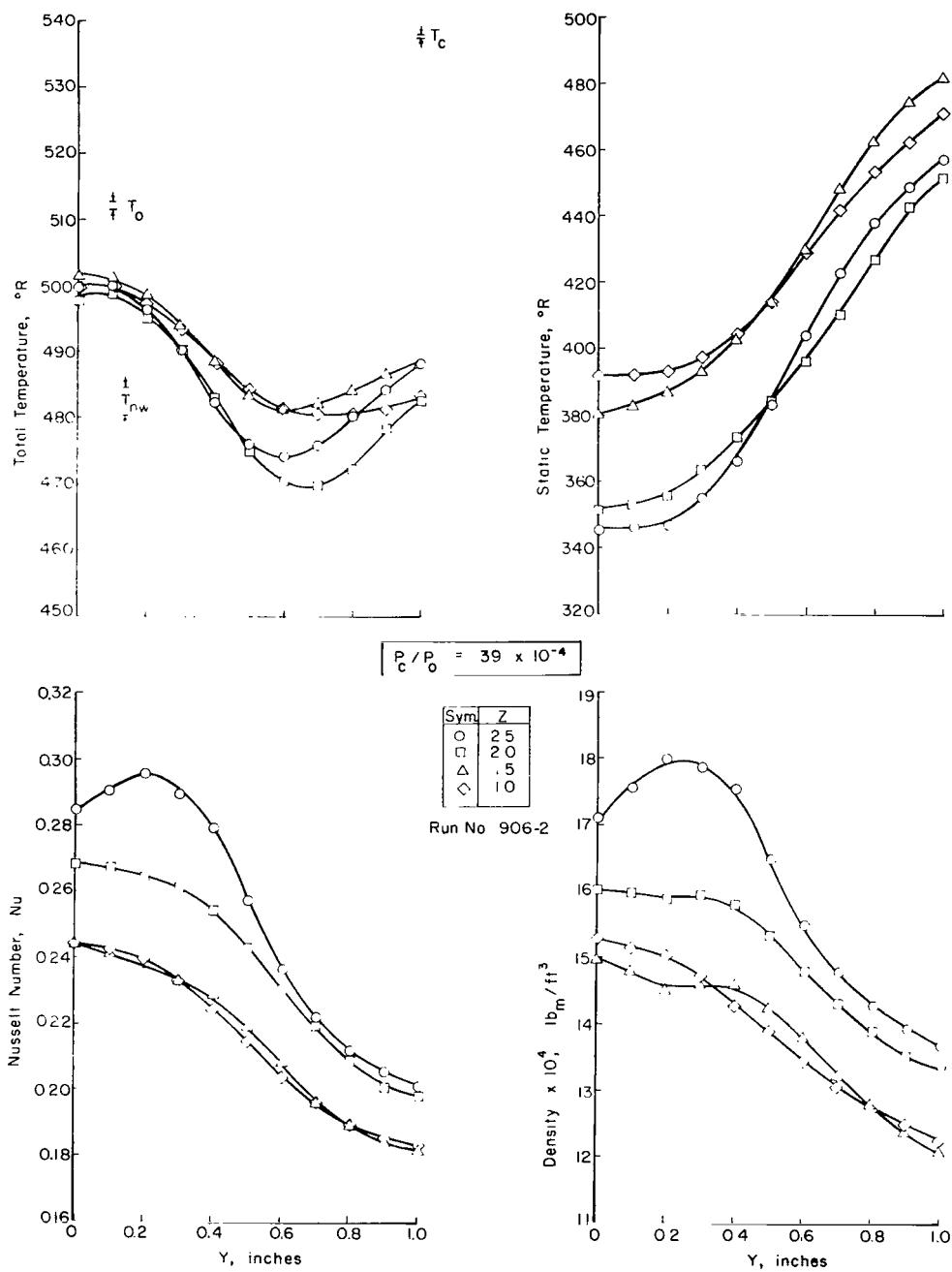
FIGURE 54.   FLOW FIELD PARAMETERS
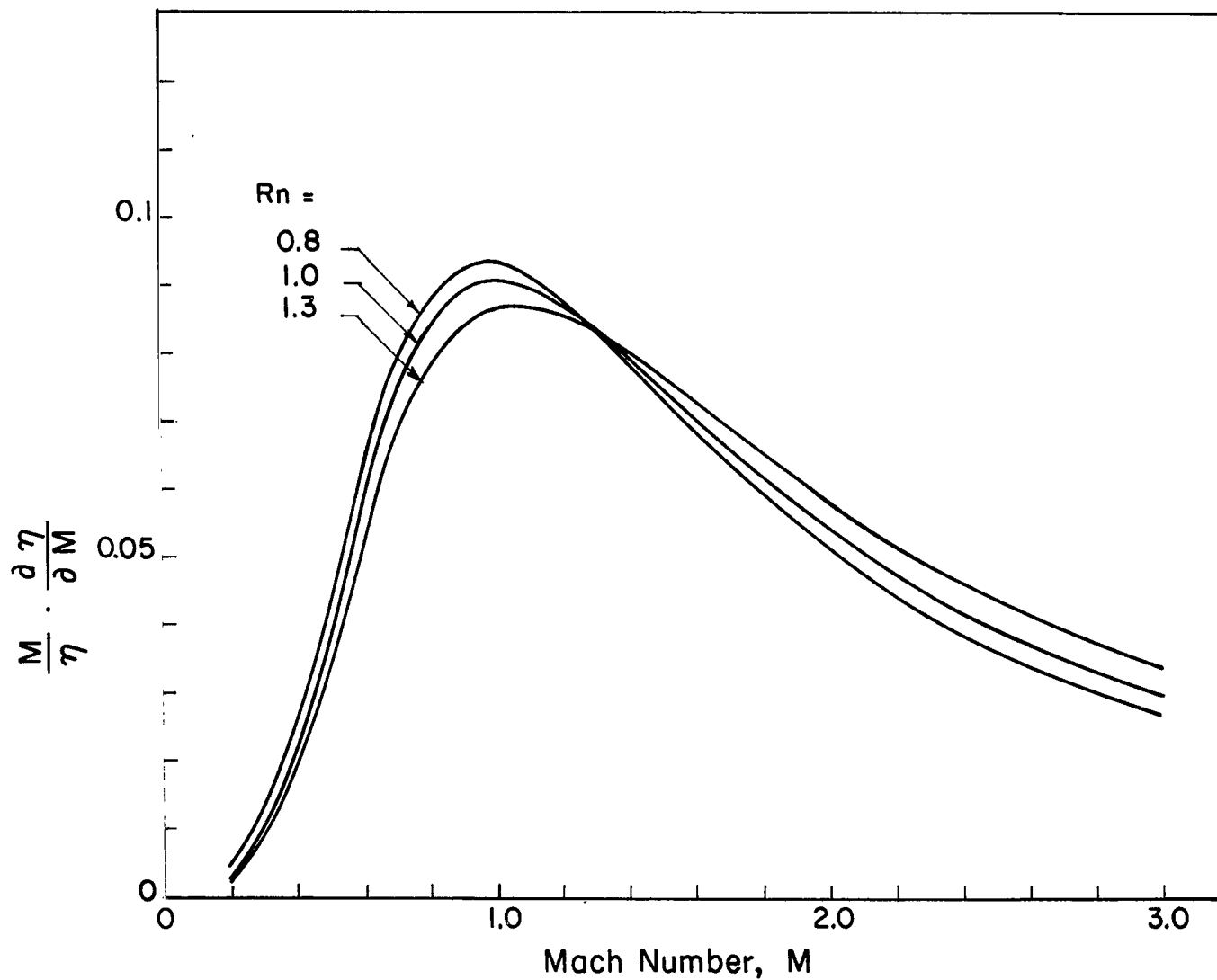
FIGURE 55. PARTIAL DERIVATIVES AS OBTAINED FROM DEWEY'S CORRELATION
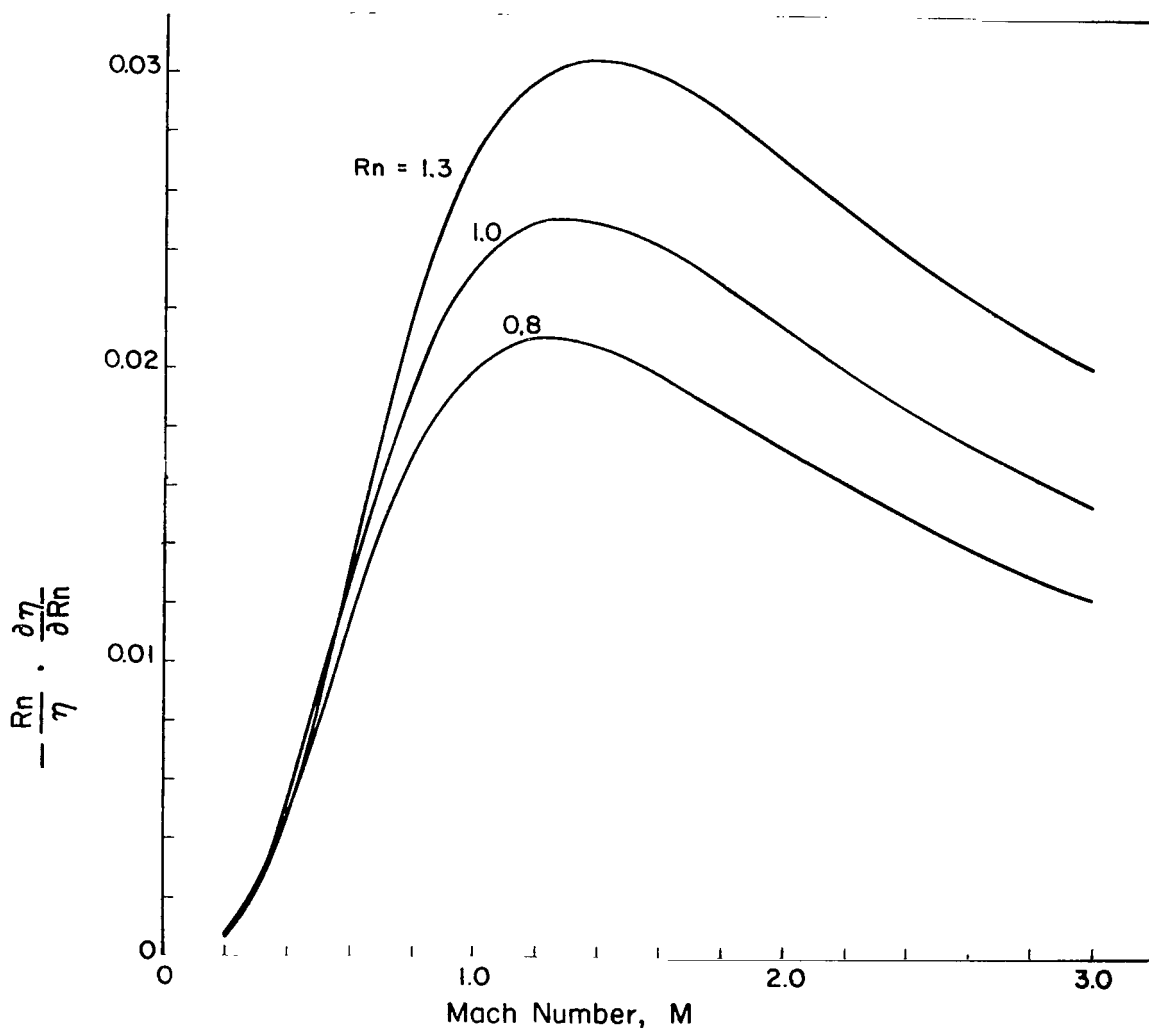
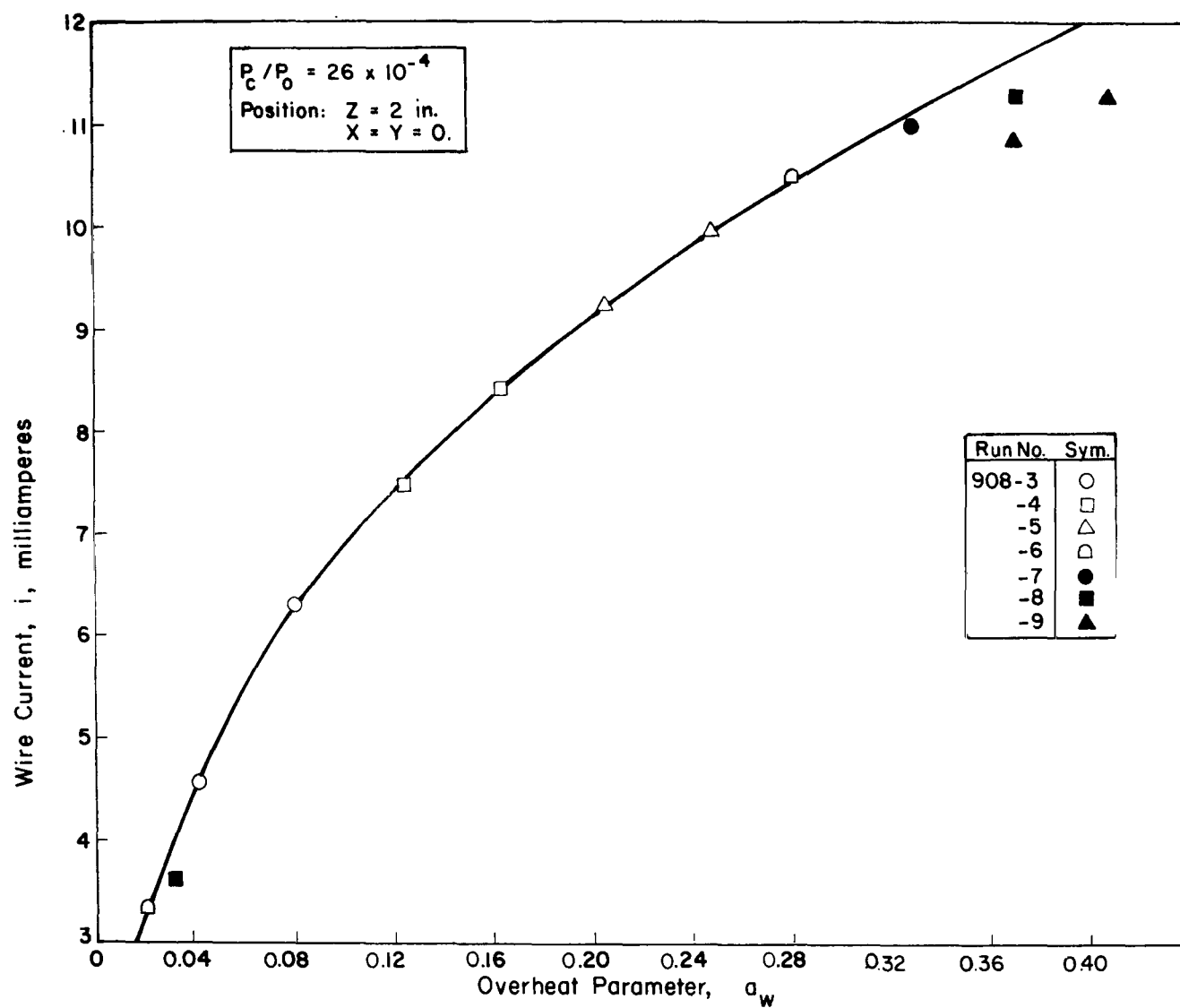FIGURE 56.   PARTIAL DERIVATIVES AS OBTAINED FROM
DEWEY'S CORRELATION
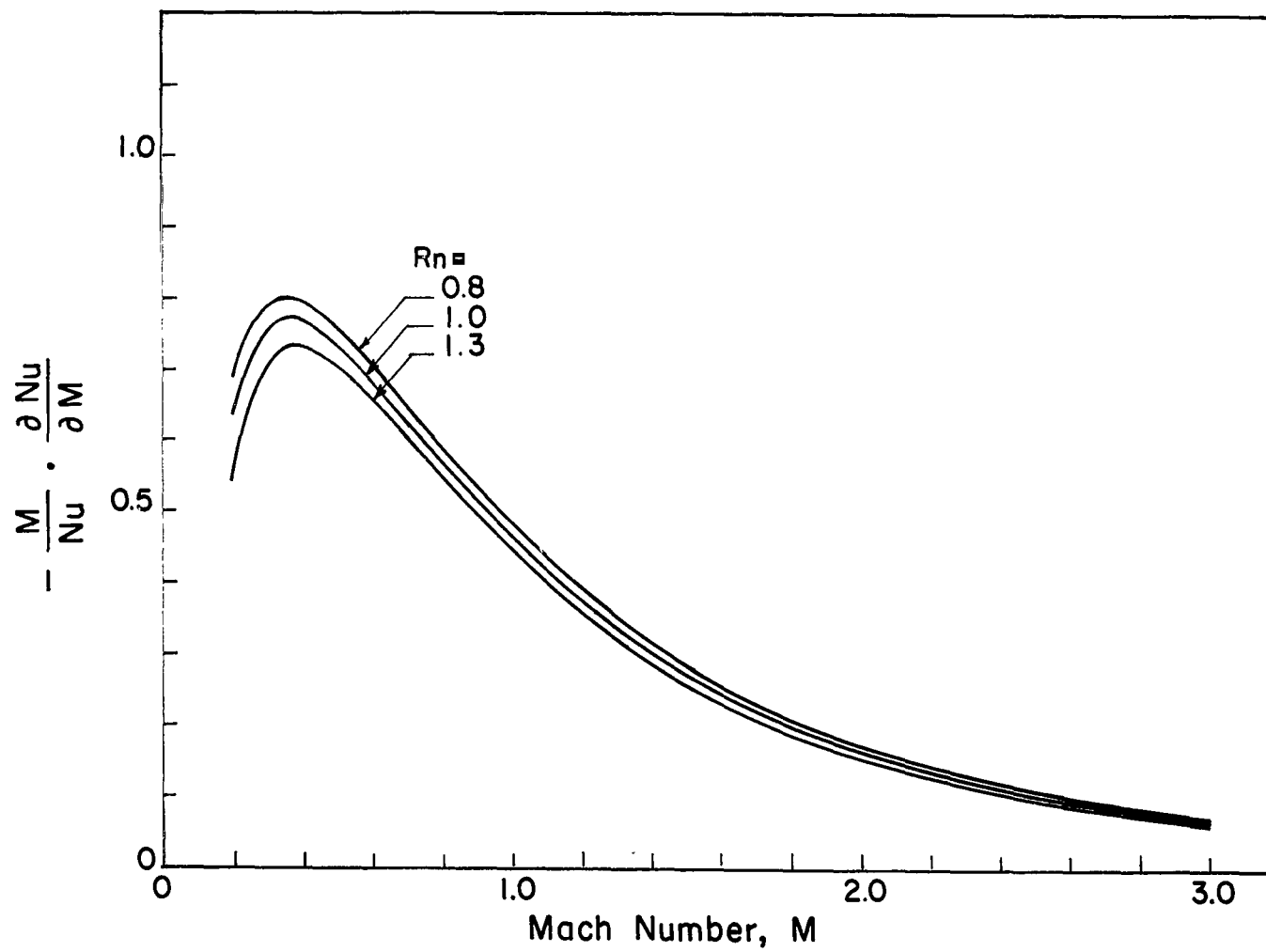
FIGURE 57.   PARTIAL DERIVATIVES AS OBTAINED FROM DEWEY'S CORRELATION
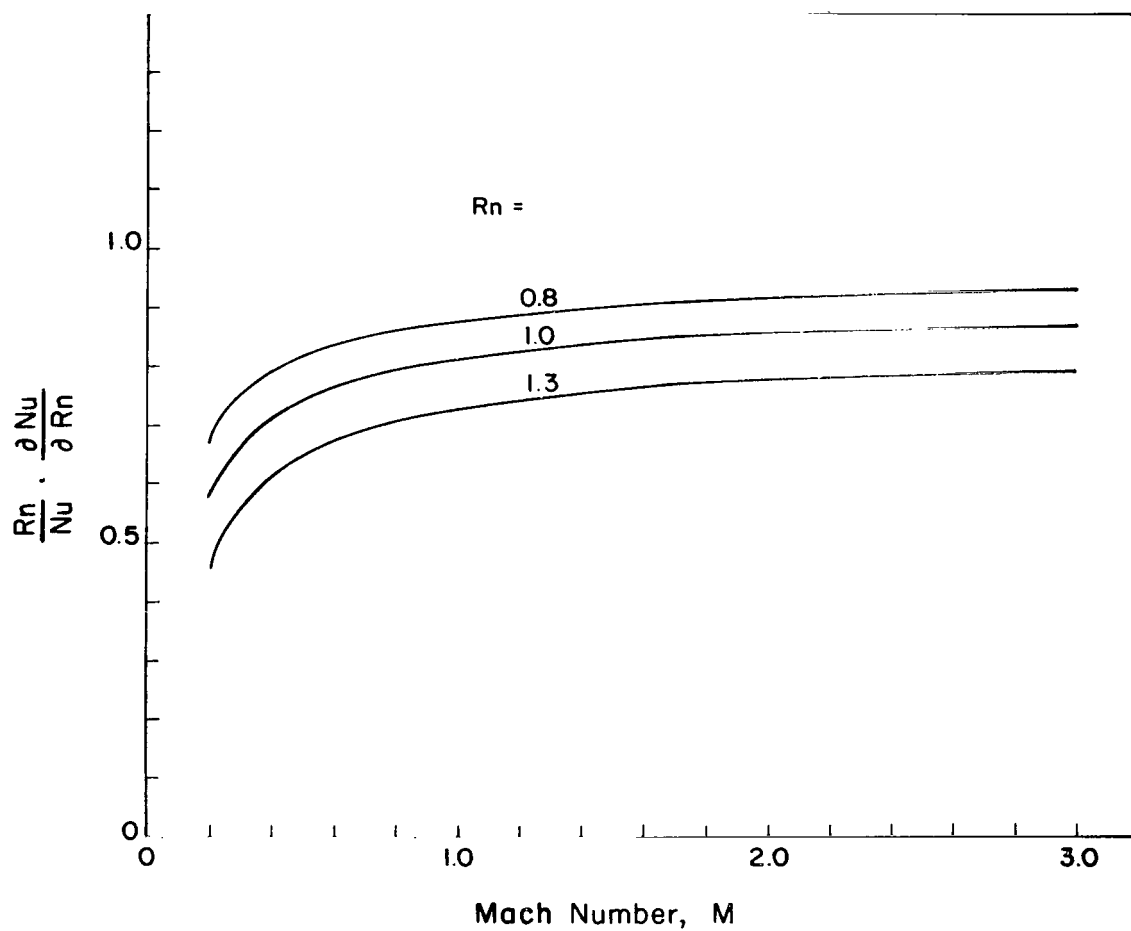
FIGURE 58. PARTIAL DERIVATIVES AS OBTAINED FROM
DEWEY'S CORRELATION

FIGURE 59. EXPERIMENTAL HOT WIRE DATA OBTAINED FROM AN OVERHEATING TRAVERSE
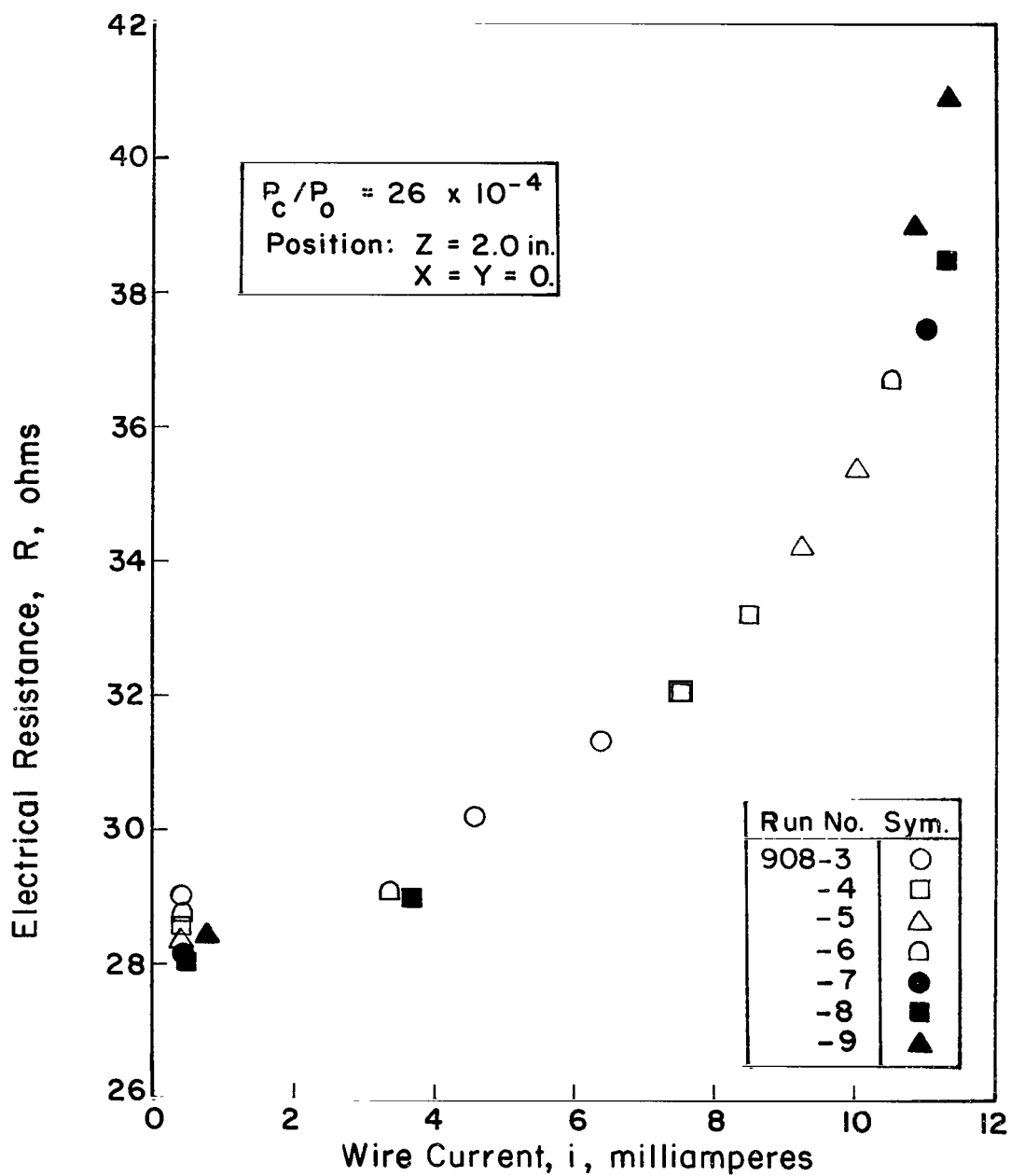
FIGURE 60.   EXPERIMENTAL HOT WIRE DATA OBTAINED FROM AN
OVERHEATING TRAVERSE
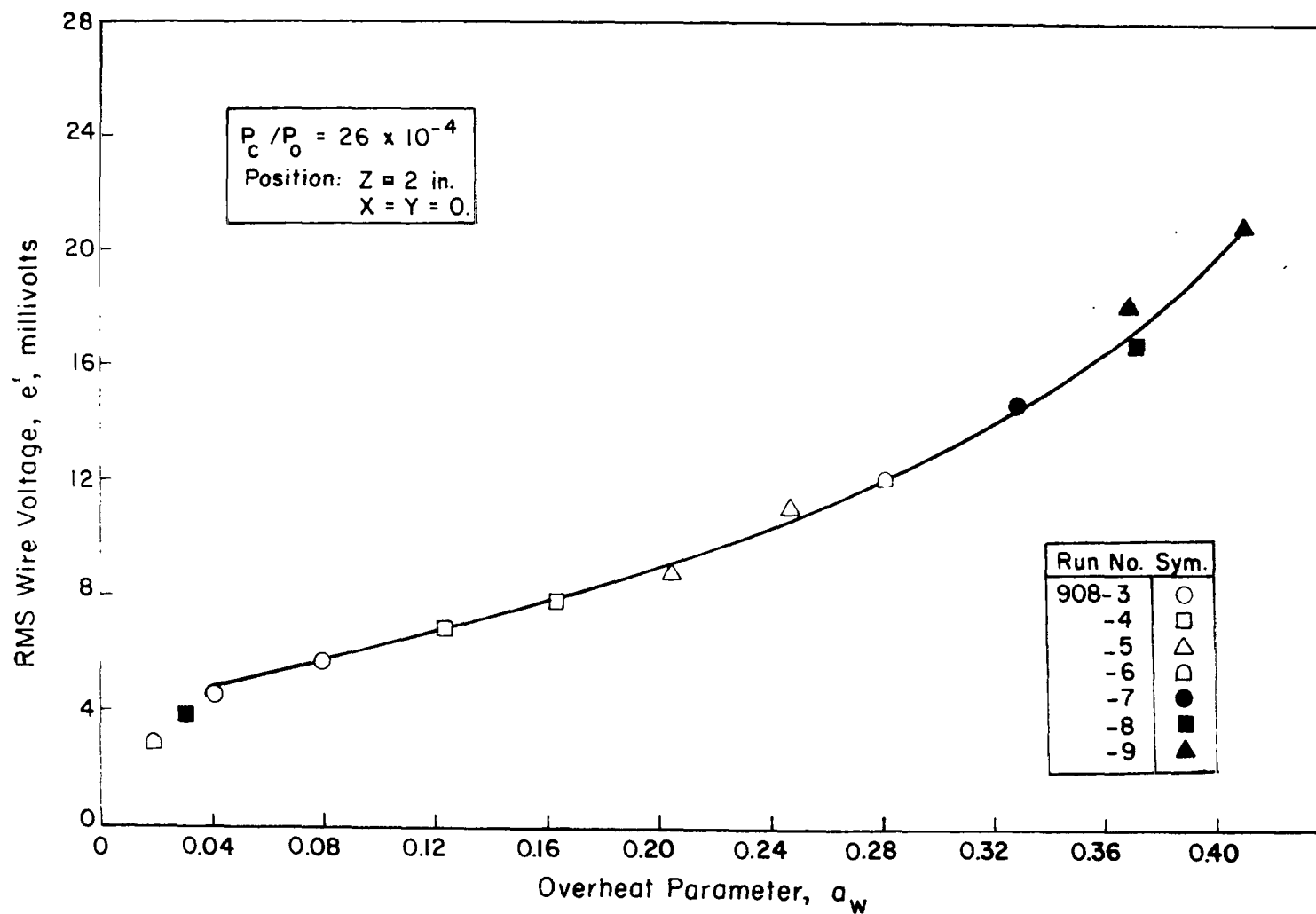
FIGURE 61. EXPERIMENTAL HOT WIRE DATA OBTAINED FROM AN OVERHEATING TRAVERSE
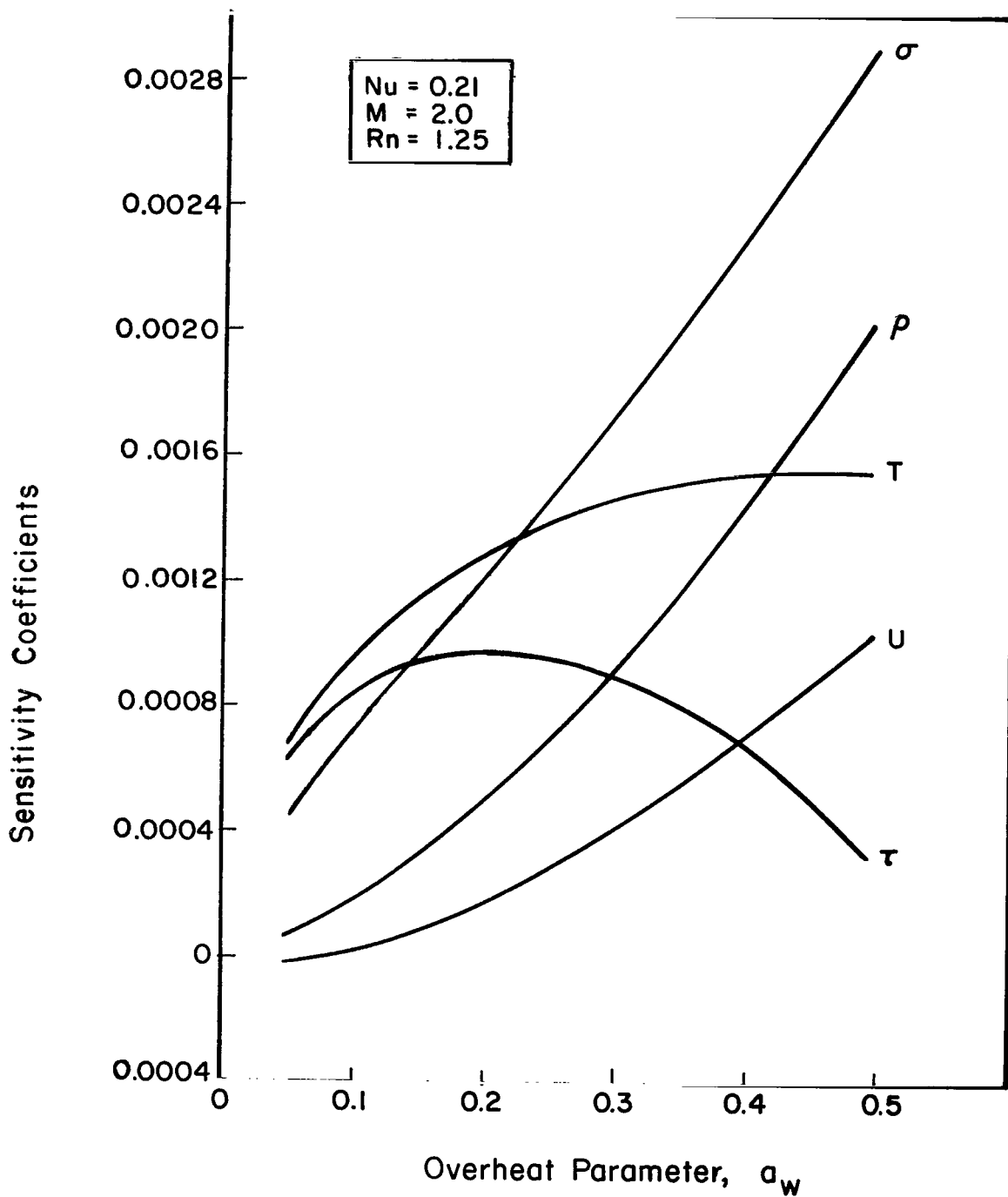
FIGURE 62. SENSITIVITY COEFFICIENTS OBTAINED FROM DEWEY'S
EMPIRICAL HEAT LAW FORMULATION AND THEORETICAL FINITE
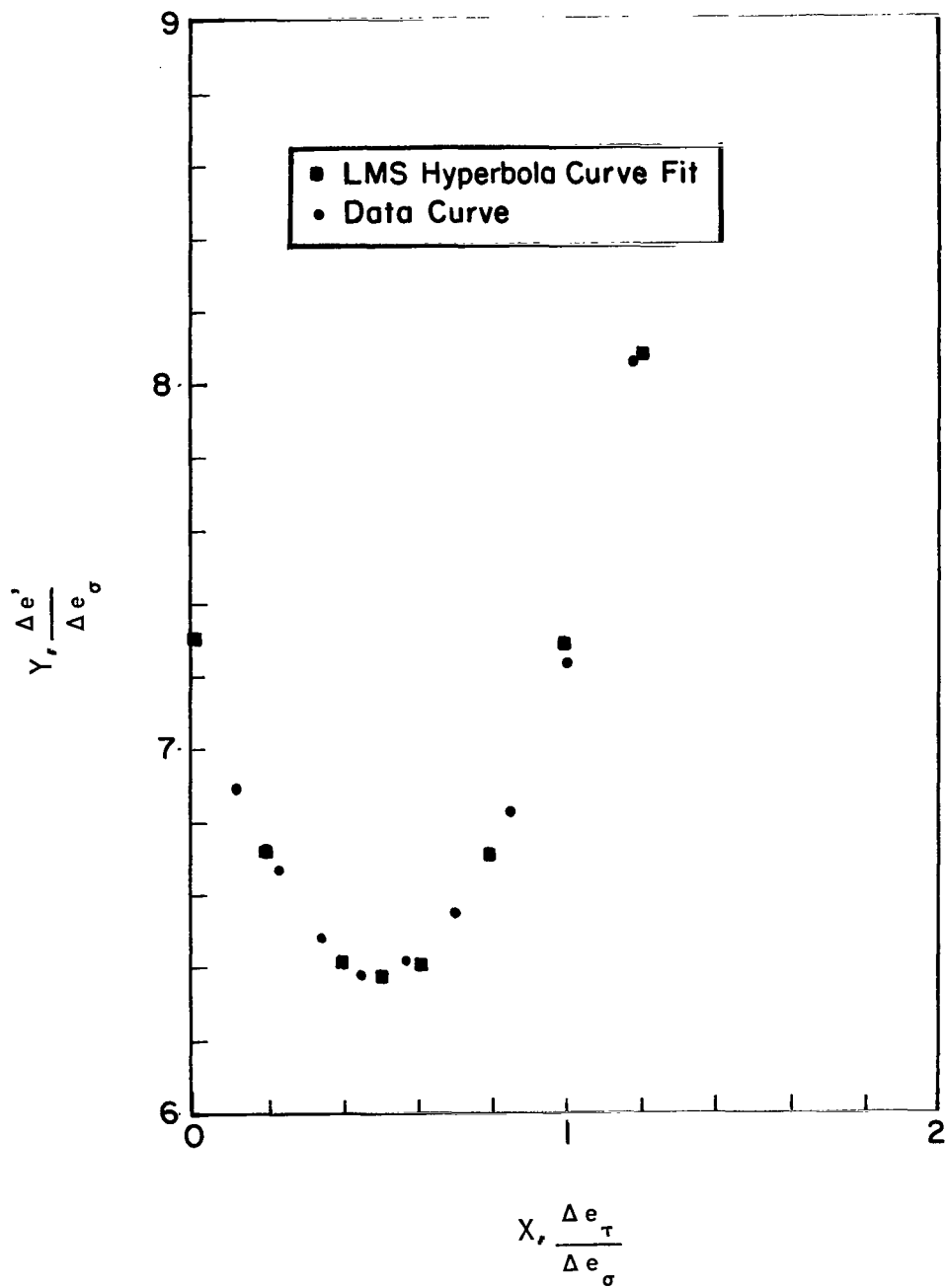WIRE OVERHEAT PARAMETERS

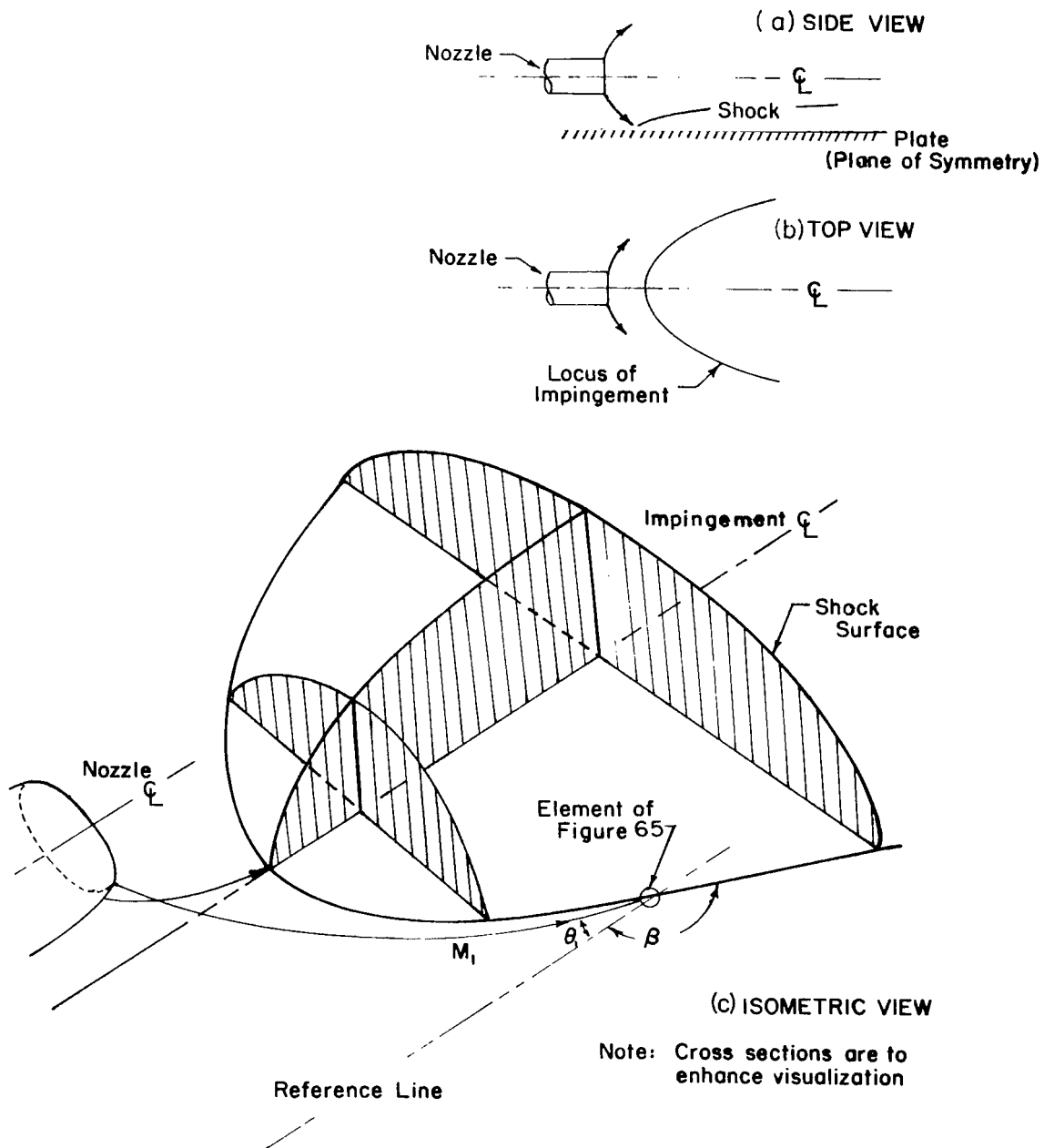FIGURE 63. X-Y FLUCTUATION DIAGRAM

(a) SIDE VIEW

Nozzle

Shock

$\cancel{\text{C}}_L$

Plate
(Plane of Symmetry)

(b) TOP VIEW

Nozzle

$\cancel{\text{C}}_L$

Locus of
Impingement

Impingement $\cancel{\text{C}}_L$

Shock
Surface

Nozzle
$\cancel{\text{C}}_L$

Element of
Figure 65

M_1

θ

β

(c) ISOMETRIC VIEW

Note: Cross sections are to
enhance visualization

Reference Line

FIGURE 64.   SHOCK ORIGINATING FROM IMPINGEMENT LINE
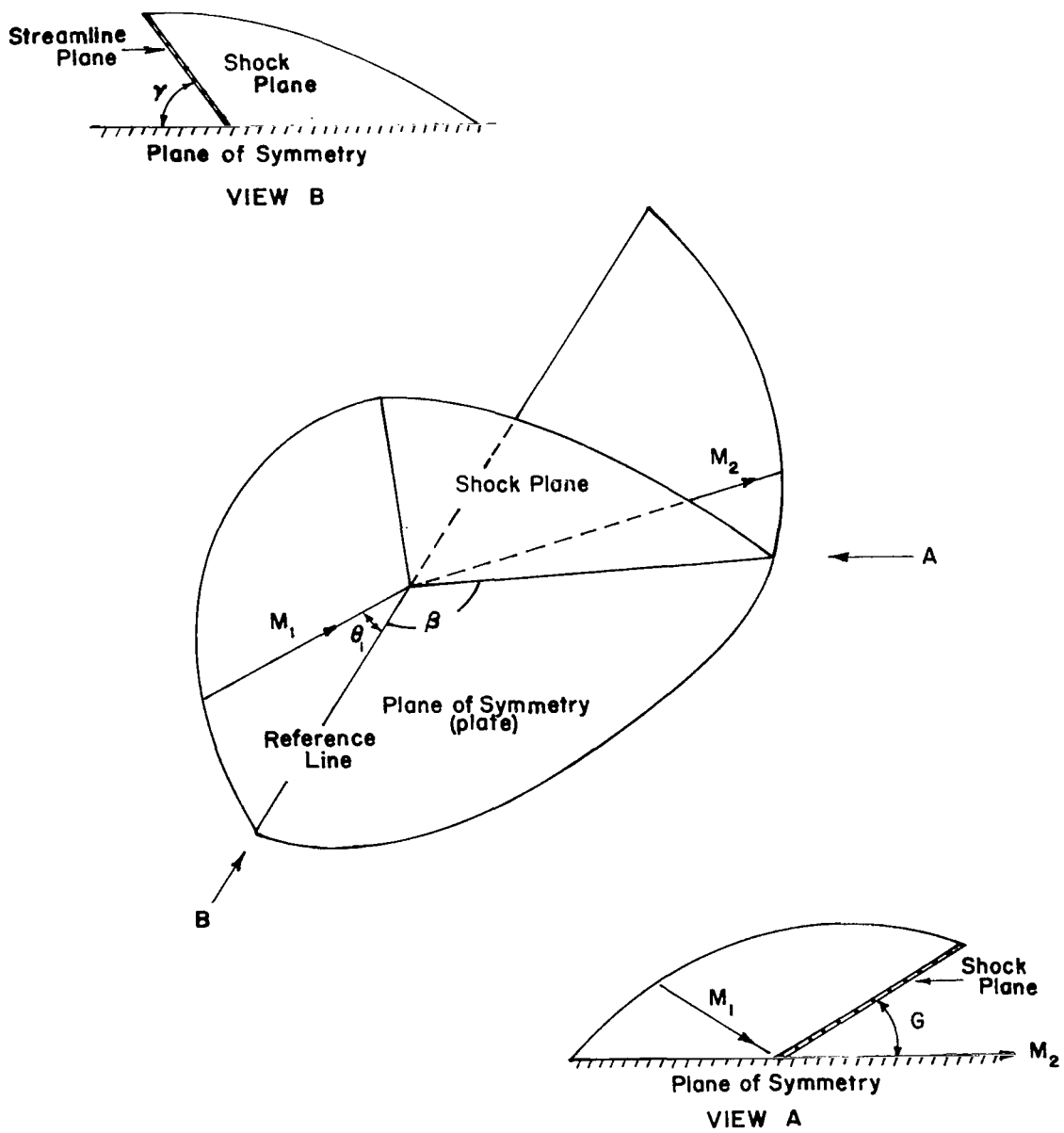
FIGURE 65. NOMENCLATURE FOR IMPINGEMENT ANGLES

1. Plane IO2 ⊥ shock plane
2. δ and θ determined from geometry
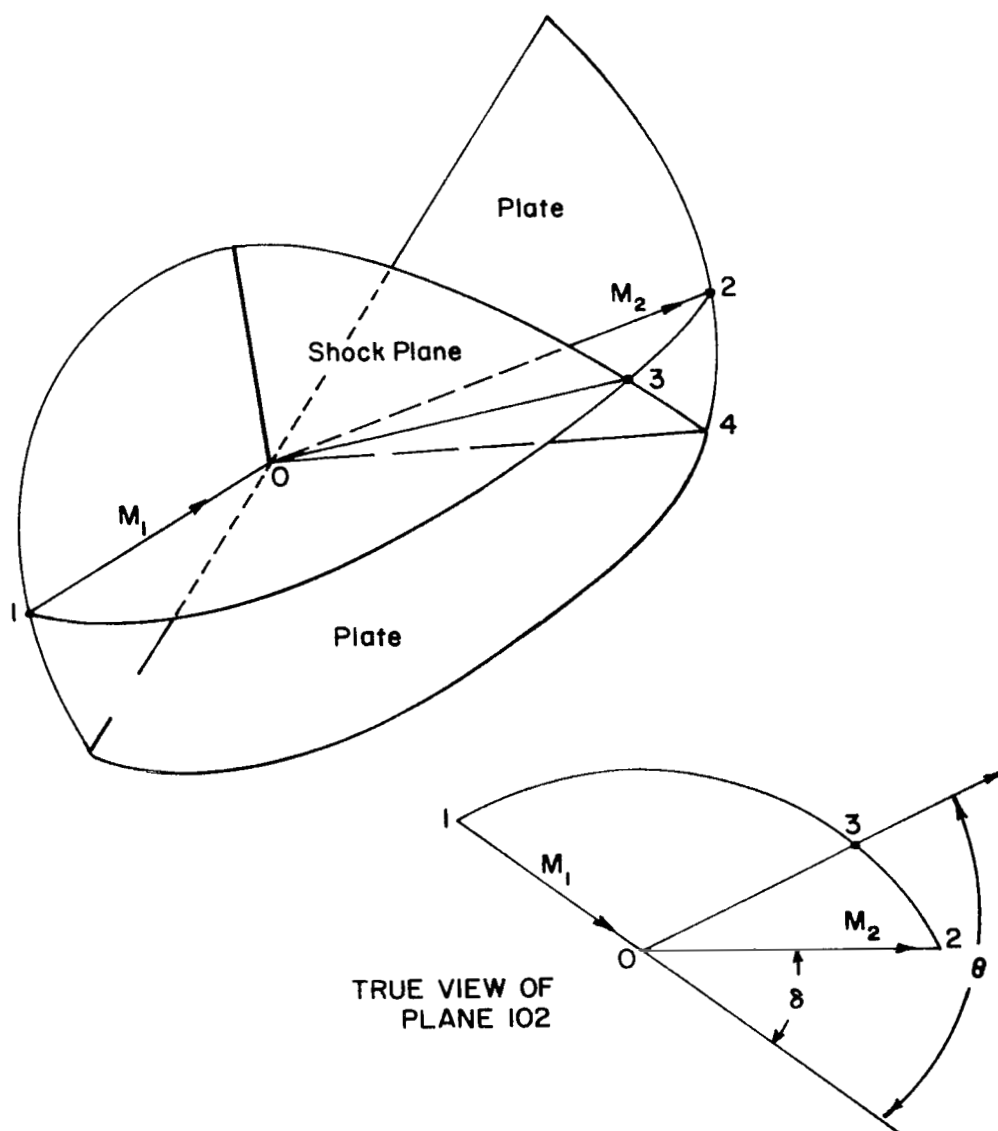   versus G with fixed M_1, θ_1, β, γ.

FIGURE 66.   FLOW DEFLECTION AND SHOCK WAVE ANGLES

"*The aeronautical and space activities of the United States shall be conducted so as to contribute . . . to the expansion of human knowledge of phenomena in the atmosphere and space. The Administration shall provide for the widest practicable and appropriate dissemination of information concerning its activities and the results thereof.*"

— NATIONAL AERONAUTICS AND SPACE ACT OF 1958

NASA SCIENTIFIC AND TECHNICAL PUBLICATIONS

TECHNICAL REPORTS: Scientific and technical information considered important, complete, and a lasting contribution to existing knowledge.

TECHNICAL NOTES: Information less broad in scope but nevertheless of importance as a contribution to existing knowledge.

TECHNICAL MEMORANDUMS: Information receiving limited distribution because of preliminary data, security classification, or other reasons.

CONTRACTOR REPORTS: Scientific and technical information generated under a NASA contract or grant and considered an important contribution to existing knowledge.

TECHNICAL TRANSLATIONS: Information published in a foreign language considered to merit NASA distribution in English.

SPECIAL PUBLICATIONS: Information derived from or of value to NASA activities. Publications include conference proceedings, monographs, data compilations, handbooks, sourcebooks, and special bibliographies.

TECHNOLOGY UTILIZATION PUBLICATIONS: Information on technology used by NASA that may be of particular interest in commercial and other non-aerospace applications. Publications include Tech Briefs, Technology Utilization Reports and Notes, and Technology Surveys.

Details on the availability of these publications may be obtained from:

SCIENTIFIC AND TECHNICAL INFORMATION DIVISION

NATIONAL AERONAUTICS AND SPACE ADMINISTRATION
Washington, D.C. 20546